ABSTRACT

PAYNE, MATTHEW JORDAN. Three-Dimensional Microphysical and Dynamical Structures of Winter Storms in the U.S. Pacific Northwest. (Under the direction of Sandra Yuter).

Frequent rainfall during the winter months in the Portland, Oregon region is associated with extratropical cyclones modified by the Coastal and Cascade Ranges. Operational WSR-88D radar observations from Portland, OR and upper-air soundings from Salem, OR over a 3-year period (2003-2006) from 1 November – 31 March are used to determine a 3D climatology of winter storms. 84 % of the 117 storm events had a low-level wind direction from the south or southwest, between 158° - 248° azimuth. Stability varied between storms, with most storms being neutral to slightly stable. Wind direction was found to be more important in determining the geographic pattern of precipitation in the PNW. For S-SW flow storms, increasing the storm volume is primarily related to increasing precipitation frequency rather than precipitation areal coverage. Local maximum in precipitation frequency is seen typically at mid-windward slope rather than at the Cascade Range crest. 3D radar observations were also compared to MM5 output for the 2005-06 and 2006-07 winter seasons. Storms were grouped by their prevailing low-level wind direction and two individual cases (2005 Dec 29-31; 2006 Nov 6-7) to compare their radial velocity, precipitation frequency, and standard deviation of radial velocity. Errors were found in the standard deviation of V_r, with the model showing more variable wind speed and direction than the observations. The spatial pattern of precipitation frequency between the radar observations and model output were found to be similar, but the magnitudes were found to usually be larger in the model output.

Three-Dimensional Microphysical and Dynamical Structures
of Winter Storms in the U.S. Pacific Northwest

by
Matthew Jordan Payne

A thesis submitted to the Graduate Faculty of
North Carolina State University
in partial fulfillment of the
requirements for the Degree of
Master of Science

Marine, Earth, and Atmospheric Sciences

Raleigh, North Carolina

2007

APPROVED BY:

Dr. William Showers	Dr. Sankar Arumugam

Dr. Sandra Yuter
Chair of Advisory Committee

DEDICATION

To my wonderful parents, Matthew Dunn Payne and Tammy Winstead Payne for being the best parents two sons could ever have, and for giving every ounce of resource and energy to making my brother, Michael Dunn Payne, and I successful. To the rest of my family for being there throughout the good and bad times, and for the wonderful support I had while in graduate school. Also, to my wonderful friends who have helped me through times a grief and have always been there for me.

ACKNOWLEDGEMENTS

I sincerely thank Dr. Sandra Yuter for providing me this wonderful opportunity to research this topic on orographic precipitation. I would also like to thank my committee members Dr. William Showers and Dr. Sankar Arumugam for providing advice and input into my thesis paper and defense. Greatly appreciated are the model output and advice from collaborators Dr. Brian Colle and Yanluan Lin of Stony Brook University. They provided MM5 output, Hovmoeller plots of radar data, and analysis of storm over, under and good prediction based on comparison of model output to SNOTEL data. Special thanks to Catherine Spooner, Kimberly Comstock, and Tim Downing for advice and technical help. Also, additional thanks go to David Stark for supplying the MRR plots and Diana Thomas for ESRL Reanalysis figures. Funding was provided by the National Science Foundation grants ATM-0544766 (Yuter) and ATM-0450444 (Colle).

TABLE OF CONTENTS

LIST OF FIGURES

Chapter 1. Introduction

Chapter 2. Data and Methods

Chapter 3. Radar Climatology Results

Chapter 4. Radar & Model Data Comparison Results

Chapter 1. Introduction

Land-falling cyclones modified by the coastal terrain and mountain orography yield frequent rainfall in the Portland, Oregon (OR) region. Neiman et al. (2007) noted that "atmospheric rivers" (Zhu and Newell 1998) play an important role in the transportation of moisture from mid-latitude cyclones towards U.S. Pacific Coast mountain barriers. These sources of water vapor help initiate heavy orographic precipitation events along mountain slopes (Smith 1979; White et al. 2003; Ralph et al. 2004; Neiman et al. 2004). In the Northwestern United States, atmospheric rivers are generally referred to as the "Pineapple Express" (Lackmann and Gyakum 1999; Colle and Mass 2000) due to the moisture influx originating near Hawaii. Some orographic precipitation events can become very intense and lead to flooding and mudslides (Ralph et al. 2005; Galewsky and Sobel 2005).

Several recent field studies have examined orographic precipitation: Eureka in Northern California (James and Houze 2005 [JH2005 from here]); the Mesoscale Alpine Programme (MAP) (e.g. Bougeault 2001; Medina and Houze 2003 [MH2003 from here]; Medina et al. 2005; Rotunno and Houze 2007), Improvement of Microphysical Parameterization through Observational Verification Experiment (IMPROVE-2) (e.g. Stoelinga et al. 2003; Garvert et al. 2005; Colle et al. 2005; Medina et al. 2007) and the Intermountain Precipitation Experiment (IPEX) (e.g. Schultz et al. 2002; Cox et al. 2005; Colle et al. 2005a; Shafer et al. 2005) (**Fig. 1**). JH2005 interpreted 2.5 years worth of three-dimensional (3D) Weather Surveillance Radar-1988 Doppler (WSR-88D) at Eureka, CA to examine the orographic effects of winter storms passing over Northern California (**Fig. 1a**). Radar patterns showed that precipitation was generally stratiform over the ocean and inland towards the mountains. Above 1 km, the flow was strong enough to be unblocked by the Sierras, and produced broadscale orographic enhancement over the coastal mountains. The mean stratiform echo pattern contained an embedded core of maximum reflectivity on the first major peak of terrain on the slope of the mountains, with a secondary echo on the second major peak (**Fig. 2**). Offshore echo enhancement was also seen with frontogensis in the offshore coastal zone. This offshore enhancement was attributed to low-level flow rising over a thin layer of cool, stable air over the ocean and adjacent to the coastal mountains. Orographic enhancement was present in all landfalling storms, but the orographically enhanced features for each storm were different. JH2005 found that orographic enhancement was well defined when the 500-700 hPa flow was strong, mid-level humidity was high, a strong low-level cross-barrier wind component and strong low-level stability.

MH2003 found that most storms from the MAP in the Lago Maggoire region of the Alps were stable or slightly unstable, with unstable storms having airflow that easily rose over mountains and stable storms having their low level air blocked by the terrain (**Fig. 1b**). Unstable and unblocked flow storms also had convective precipitation over the first major peak of the terrain, which was absent in stable, blocked cases. MH2003 documented two strong storms during the 7 September to 15 November 1999 MAP study in the Lago Maggiore region of the Alps: IOP2b and IOP8. Unstable and unblocked conditions were observed in IOP2b which produced much more cloud water than IOP8, and which in turn led to more locally heavy rain along the windward slopes of the Alps (**Fig. 3**). IOP8 represented stable and blocked low-level flow which prevented the flow to easily rise over the Alpine terrain. Rainfall amounts were high in IOP8 compared to storms that regularly occur in the

Alps, but it depended on the condensation of moisture above the 900-hPa level. Dual-polarization radar from NCAR S-Pol radar helped confirm that during IOP2b, flow easily rose over the terrain and yielded locally strong updrafts that led to large concentrations of cloud liquid water and graupel formation over the first major peak of the Alpine terrain. Both storm cases had areas of dry snow above and wet snow below 0 °C (**Fig. 4**). This led to MH2003 to develop an idealized schematic to generally categorize the mechanisms observed during two different storm types (**Fig. 5**).

IMPROVE-2 observed frontal systems passing through the Pacific Northwest (PNW) during the wet season (**Fig. 1c**). The experiment employed the NOAA-P3 and University of Washington Convair-580 aircraft, the NCAR S-Pol radar, the NOAA/ETL S-Prof vertically pointing S-band radar, and ground-based particle sampling to observe various properties of precipitation on a range of scales. Garvert et al. (2006) showed that as frontal cloud systems pass over the Cascades, vertically propagating gravity waves affect the vertical motion and cloud structure over the windward slope, consistent with Colle (2004)'s idealized 2-D simulations (**Fig. 6**). Colle (2004) ran simulations to understand the relationship between orographic precipitation and the height and width of the barrier, ambient flow, moist static stability, and freezing level. In **Figure 6**, increasing the wind speed with a constant mountain height yielded higher production of precipitation upwind of the mountain barrier. Strong cross-barrier wind also produced a well-defined gravity wave, which is typically seen in vertical cross section when flow along lines of potential temperature start to bend downward to the surface. The local minimum in height of potential temperature occurs just over the peak of the mountain. Gravity waves resulted in the precipitation enhancement over the windward slope of the mountain.

Most research from IMPROVE-2 has been focused on the 13 – 14 December 2001 case where over 60 mm of liquid equivalent precipitation fell on the Cascade crest in a 24-hr period. Model studies of the IMPROVE-2 case from 13 – 14 December 2001 showed errors including overprediction of the amount of precipitation observed over the windward slope and lee of the Cascades because of excessive cloud liquid water (Colle et al. 2005b; Garvert et al. 2005a,c). Snow amounts aloft were overpredicted by the MM5 by a factor of two which spilled over the mountain crest to the lee of the Cascade Range and produced an overprediction of precipitation there (Garvert et al. 2005c). Medina et al. (2007) also found that upwind tilting maximum reflectivity structures preceding a dip in potential temperature, or gravity waves, affected the vertical motion and cloud structure in the upper levels over the windward slope of the Cascades.

By examining 16 cyclones moving into western Oregon, Medina et al. (2007) developed a conceptual model showing the typical echo structure as the cyclone passes over the windward slope of the Cascades (**Fig. 7**). The early period of storm passage is designated as the leading edge echo in the warm advection region of a cyclone. Precipitation here appears aloft in the initial stages around 6 – 7 km altitude, and then gradually descends to the surface. The middle sector of the storm is called the double maximum echo, which is a thick layer of more intense precipitation that extends up to 5 – 6 km altitude from the surface. The lower echo-intensity maximum region in the middle of a storm takes several hours to pass over a point on the windward slope and is a bright band associated with particle melting. A second region of maximum reflectivity becomes present when the storm approaches the windward slope of the Cascades, due to the interaction of the baroclinic system with the terrain. Throughout the period of a storm, the freezing level varies 1 – 3 km between each sector (**Fig. 8**).

The IPEX field program was performed as an opportunity to examine precipitation formation over a narrow mountain barrier in the Western U.S (**Fig. 1d**). Doppler radar and microphysical data was obtained along the Wasatch Mountains in Utah in February 2000, using NOAA P-3 aircraft and two mobile Doppler radars (Schultz et al. 2002). Cox et al. (2005) found that low level flow was blocked by the Wasatch Mountains in Utah on 12 February 2000 and caused precipitation enhancement upstream of the barrier. Colle et al. (2005a) used detailed model simulations at 1.33-km grid size in the MM5 to show the importance of the Great Salt Lake and the upstream terrain on enhancing blocked structures. Overall, the 1.33 km grid size MM5 performed by Colle et al. (2005a) obtained fairly accurate predictions for overall precipitation amounts (within 10 – 20 %), but had errors in cloud water and snow amounts (**Fig. 9**). The model overpredicted the cloud water by 40 – 50 %, while it underpredicted on snow by 40 %. These problems led to the suggestion of modifying the amount of snow crystals at colder temperatures to improve the snow forecast.

These major field programs have provided comprehensive observations, but only over short time periods. Conceptual models obtained from field projects can be extended and refined using less comprehensive but longer duration observations that encompass a larger sample of storms and storm environments. This study utilizes operational radar and upper-air sounding data to examine the three-dimensional (3D) characteristics of storms in the Portland, Oregon (OR) region of the PNW. This region was selected for its high frequency of orographic precipitation events, the proximity of the local operational radar and upper-air sounding sites and their locations relative to topography.

Taking a look at oscillation cycles such as El Niño-Southern Oscillation (ENSO) and Pacific Decadal Oscillation (PDO), both cycles are apparent during our three winter season analysis (2003 – 2006). ENSO occurs when the upwelling of cool Pacific Ocean waters off the Northern Chile and Southern Peru ceases and a warm, southward moving current flows along the Peruvian coast. Changes in large scale circulation in turn yield change in precipitation, leaving some areas drier while others are wetter during El Niño compared to non-El Niño years. This oscillation tends to occur every 3 – 7 years. Storm systems during El Niño tend to pass south of PNW due to the subtropical and polar jets shifting southward (**Fig. 10a**). Storms in the PNW during El Niño occur more infrequently than normal, thus the PNW tends to be drier than average. La Niña events are the opposite of El Niño, with cooler than average sea surface temperatures off the Peru coast. This in turn yields wetter than average precipitation over the PNW, with the subtropical and polar jets shifting to the north (**Fig. 10b**). El Niño in the PNW is associated with large rainstorms and floods, especially during 1996 – 97 (Dettinger et al. 2004). Weak El Niño conditions occurred during the first winter season (2003 – 04) of our analysis, with weak La Niña conditions observed for the 2005 – 06 winter season (Taylor 1998).

The PDO is a long-lived oscillation pattern of Pacific climate variability. Unlike ENSO, the PDO can persist for a 20 – 30 year period. Signatures of the PDO are more evident over the PNW than during ENSO. PDO conditions since 1990 have been complex, changing from warm phase (1992 – 1998), followed by a brief period of weak cold phase

(1999 – 2001), to the current warm phase that began in 2002. Only during warm cycles, the flow tends to be more from the south or southwest, favorable for a high frequency of storms moving through the PNW. Cold cycles show more north or northwesterly flow and having more intermittent extratropical cyclones passing through the PNW. The PDO index pattern in **Figure 10c** showed that the PNW was generally in a warm cycle during our three year winter storm analysis (JISAO).

In particular, since most flows in the PNW are stable, we seek to refine and extend Medina and Houze's (2003) [MH2003 from here] idealized schematic for stable flow where moist rain occurs on the lower slopes (**Fig. 5**), Colle's (2004) idealized study that compares orographic flow based on changing storm characteristics (**Fig. 6**) and Medina et al. (2007)'s schematic of three typical reflectivity structures observed during mid-latitude Pacific cyclones (**Fig. 7**). This study follows the general methodology of JH2005 for identifying heavy rain events and analyzing the characteristics of their associated 3D radar data. We extend their methodology by considering the standard deviation of radial velocity which provides insight into the variability of the mean flow. Additionally, we use precipitation frequency rather than the mean radar reflectivity to describe the precipitation structures due to the highly variable freezing level and bright band effects during Portland winter storms that greatly complicate quantitative comparison of reflectivities among storms.

Chapter 2. Data and Methods

Thirty-year (1961 – 1990) rainfall climatology from Daly et al. (1994) shows that over 2.5 m (100 in) of rainfall occurs annually over the high peaks of the Coastal and

Cascade Ranges in the PNW (**Fig. 11a**). Approximately 90 % of the annual precipitation in the Portland, OR region occurs from October to May (NWS Portland, OR). At Portland International Airport (PDX), 41 % of days per year have accumulations 0.25 mm (0.01 in) or more, which increases to 58% for November - March. The city of Portland, OR is located along the Columbia River within the Willamette Valley at about 0.5 km above mean sea level (MSL) (**Fig. 11b**). Separating Portland from the Pacific Ocean to the west is the Coastal Range, whose crest is at 0.8 – 1 km MSL and oriented in a north-south (N-S) direction. To the east of Portland is the Cascade Mountain Range, where typical crest elevations range from 1.5 – 3 km MSL and are also oriented N-S similar to the Coastal Range.

We define a winter season as the set of heavy precipitation events occurring from 1 November through 31 March (with a few exceptions occurring a few days before or after). In total, we examine 117 storms from 2003 – 2006 (35 in 2003 – 04, 20 in 2004 – 05, and 62 in 2005 – 06). Storm days were selected based on daily rainfall totals of at least 5 mm (0.2 in) from PDX. Surrounding days that accumulated at least 2.5 mm (0.1 in) were also included along with the storm event. The following sections describe the radar data, upper-air soundings, calculations of thermodynamic variables, and Willamette Valley airflow characteristics, which are then compared to results of previous studies.

2.1 Radar Data

We use three winter seasons of archived Level II Next-Generation Radar (NEXRAD) Weather Surveillance Radar 88 Doppler (WSR-88D) radar observations from the National Climatic Data Center (NCDC) for storms in the Portland, OR (KRTX, height = 0.479 km) region of the U.S. Pacific Northwest. The initial storm definition was refined by using KRTX radar data to determine the start and end times of radar echo within the radar domain to the nearest hour using the MountainZebra display (James et al. 2000). MountainZebra provided visualizations of radar images in horizontal and vertical cross sections with a detailed terrain field. The WSR-88D Level II data were converted to Universal Format (Barnes 1980), and quality control was applied to reduce non-meteorological echo such as ground clutter and anomalous propagation. Data were then processed to dealias radial velocities (James and Houze 2000) and interpolated to 3D Cartesian grids utilizing NCAR Earth Observing Laboratory's REORDER software with Cressman weighting. The interpolation grid was 120 km x 120 km x 16 km with 2 km spatial resolution in the horizontal and 1 km resolution in the vertical. Finally, the data were converted into Unidata's Network Common Data Format (NetCDF) for display in MountainZebra and statistical analysis in Matlab.

2.2 Radar mean, standard deviation, and precipitation frequency

Several different fields were computed from the observed radar fields for sets of radar volumes. Averages of radial velocity (V_r) were calculated for each storm and sets of several storms. Standard deviation values were computed to characterize the consistency of flow characteristics. A radar reflectivity threshold value of 13 dBZ, equivalent to 0.2 mm hr^{-1}, was used to compare the frequency of rainfall among the radar data subsets (Hagen and Yuter 2003). JH2005 used the same dBZ threshold to determine if precipitation was more intense or frequent within their study area. The frequency was computed by summing radar pixels ≥ 13 dBZ within the 3D radar volumes of each storm or set of storms and dividing by the number of volumes.

Precipitation frequency is used instead average reflectivity because the freezing level and bright band vary during Pacific Cyclones. Medina et al. (2007) showed that through the three storm sectors, the freezing level varies 1 – 3 km MSL, so using average maximum reflectivity for comparison would prove to be difficult. A threshold of 20 % is applied to data to get rid of points with large uncertainty due to small sample size in the frequency and V_r standard deviation plots (**Fig. 12**).

All precipitation frequency values of 20 % or less are masked out of the averaged NetCDF files and then these same areas are applied to V_r standard deviation data to mask out extreme values observed usually over the Pacific Ocean, near beam blockage, and in the lee of the Cascades. This threshold technique replaces precipitation frequency values ≤ 20 % with missing values and thus removes information with low sample size in the upper levels of the radar data. We show radar horizontal cross sections for the 2 – 3 km layer to illustrate data characteristics over the mountain slopes. Vertical radar cross sections (red lines in the horizontal plots) are taken parallel to the flow for radial velocity variables, and over the southern portion of the radar scan for precipitation frequency.

2.3 Upper-air sounding data

The Salem, OR upper-air sounding (SLE) site is 75 km south of KRTX in the Willamette Valley (**Fig. 11b**). Soundings were examined for the same time period as the KRTX WSR-88D data to obtain upwind flow characteristics related to Cascade Range orographic enhancement. Layer averages of upper-air sounding data were obtained from the surface (0.61 km MSL) to approximately 2.2 km MSL, which corresponds to 1010 – 770 hPa and provided information on the current flow conditions during each storm. Each storm is represented by the layer-averaged sounding values from the sounding time nearest to storm's peak intensity. The 117 storms were grouped in several subsets by wind direction, stability, wind speed, and time accumulated precipitation area to characterize the precipitation climatology.

2.4 Willamette Valley airflow characteristics

A histogram plot of layer-averaged storm wind directions for storms illustrates how many storms fell into the different wind direction categories for all three winter seasons (**Fig. 13a**). In all, 84 % (98 out of 117) of the storms were found to have averaged wind directions from the southwest (225° ± 22.5º) (54 storms) or south (180° ± 22.5°) (44 storms). Other storms were found in the northwest (315° ± 22.5°) (2 storms), west (270° ± 22.5°) (8 storms), and southeast (135° ± 22.5°) (9 storms) categories. We group the storms into three categories for further analysis -- southeast (SE), south-southwest (S-SW), and west-northwest (W-NW). For the Cascade Mountain Range, the cross-barrier wind is the wind component from the 270º azimuth. As expected, the cross-barrier wind speed dominates when the layer-averaged wind direction is nearly perpendicular to the mountain range, with values greater than 2 ms^{-1} for winds ranging between 180º - 260º azimuth (**Fig. 13b**).

The Brunt-Väisälä frequency (B-V), defined in Durran and Klemp (1982) as the frequency at which an air parcel will oscillate which subjected to an infinitesimal perturbation in a stably stratified atmosphere, was calculated between consecutive layers using the thermodynamic equations and upper-air sounding data to determine the layer-averaged variables (Wallace and Hobbs 1977). The moist B-V (Nm^2), where the buoyancy force is measured in a saturated atmosphere, and the dry B-V (Nd^2), used for unsaturated air, were calculated from equations in Durran and Klemp (1982) (1) and Emanuel (1994) (2):

$$N_d^{\ 2} = \frac{g}{\overline{T}}\left(\frac{dT}{dZ} + \Gamma_d\right) \quad (1)$$

$$N_m^{\ 2} = \frac{1}{1+q_w}\left\{\Gamma_m \frac{d}{dz}\left[\left(c_p + c_l q_w\right)\ln\left(\Theta_e\right)\right] - \left[c_l \Gamma_m \ln\left(T\right) + g\right]\frac{dq_w}{dz}\right\} \quad (2)$$

where in the dry B-V equation, T is the sensible temperature of the atmosphere, g is the gravitational acceleration, Γ_d is the dry adiabatic lapse rate, and Z is the atmospheric height. Additional variables seen in the moist B-V equation are q_w, which is the total water mixing ratio, Γ_m is the saturated adiabatic lapse rate, c_p and c_l are the specific heat at a constant pressure and liquid, and Θ_e is the equivalent potential temperature.

Figure 13c is similar to Figure 3 from JH2005 and shows layer-averaged moist B-V and wind direction for all three winter seasons. Most storms were either neutral or slightly stable, with 83 % of storms falling between 0 and 3 x 10^{-4} s^{-2}. For wind directions between 180° - 260º azimuth, the range of B-V values increased, suggesting that air masses from the south varied in stability compared to those from the west. Most storms in Oregon tended to have neutral to slight stability compared to mostly unstable flow during storms (~ 65 %) in the JH2005 study in Eureka, CA. The moist B-V versus the cross-barrier wind speed plot in **Figure 13d** suggests that stable B-V values (> 0 s^{-2}) vary more with total wind speed than unstable values, but is a weak result because of the small accumulation of unstable samples.

Using the 800 – 900 hPa layer average similar to JH2005, the measurement of the Froude number was analyzed in this study (**Fig. 13e**). The Froude number was defined as:

$$F_r = \frac{U}{Nh} \qquad (3)$$

with h = average mountain height (1.8 km), U = cross-barrier wind speed in ms^{-1}, and N = moist Brunt-Väisälä frequency. When $F_r < 1$, the low-level cross-barrier flow is blocked and precipitation tend to form upstream of the barrier (Grossman and Durran 1984; Sinclair et al. 1997; Colle 2004; Medina et al. 2005). When $F_r > 1$, not much upstream precipitation development is observed, with air rising directly over the terrain and precipitation enhancement is seen over the individual mountain peaks (MH2003; Rotunno and Ferretti 2003). In this comparison of the Froude number to wind direction, the majority of storms are blocked according to the analysis, which uses an average mountain height of 1.8 km. The amount of precipitation uplift depends on the size and shape of the barrier, wind speed, and stability of the flow given by the linear gravity wave theory (Colle 2004; Smith and Barstad 2004).

When storm total volume (3D accumulation of radar pixels with 13 dBZ or more throughout each storm) was less than or equal to 2 x 10^7 km^3, the Froude number and the layer-averaged wind direction of the storms across all three winter seasons varied substantially (**Fig. 14a,b**). Above this storm total volume threshold, nearly all storms had strong south to southwesterly wind components, similarly to the cross-barrier wind speed plot in Figure 5b. The variation of moist B-V below the 2 x 10^7 km^3 volume threshold is much larger than the variation above the threshold (**Fig. 14c**). This finding suggests that the stability of smaller storms varies greatly, but when the storm total volume increases, it is more likely that the storm will be stable and likely produce stratiform structures. Wind speed was poorly correlated with storm total precipitation volume (**Fig. 14d**). Compared to wind direction, storm totaled volumes have a more scattered relationship with cross-barrier wind speed than in Figure 6a (**Fig. 14e**). An increase in the cross-barrier wind speed did not necessarily result in a larger storm total volume. A histogram analysis of storm accumulated volumes showed that 87 % of storm total accumulated volumes are below 2 x 10^7 km^3 (**Fig. 14f)**. This shows that though the larger volume storms are typically from the S-SW, the smaller volume storms are more frequent.

Chapter 3. Radar Climatology Results

3.1 Low-level wind direction

As expected, the three wind direction categories had different wind characteristics. The SE storms were southerly at 1 – 2 km altitude veering (wind speeds turning clockwise with height) slightly to SW above 4 km (**Fig. 15a**). The S-SW storms also veered with height, from a southerly direction at 1 – 2 km altitude towards the SW above 3 km altitude (**Fig. 15c**). The S-SW storms had greater directional wind shear than SE storms. The W-NW storms had the weakest winds of the three wind direction categories, with magnitudes reaching velocities of around 12 ms^{-1}. This is especially evident in the horizontal cross section, where speeds of 15 ms^{-1} or greater are sparse in W-NW storms compared to the SE and S-SW storms (**Fig. 15e**). W-NW storms had the weakest directional wind shear, shifting slightly from west-southwest near the surface to westerly at 6 km altitude.

V_r magnitudes steadily increase with height in all three vertical cross sections (**Fig.**

16a,c,e). The S-SW wind speeds were stronger by 5 ms^{-1} than the SE storms near the surface, and have a greater vertical wind shear gradient within the 1 – 5 km layer than SE storms. Winds for S-SW storms also appeared to be stronger by 10 ms^{-1} over the high Cascades peaks in the 6 – 8 km altitude layer than the SE storms. W-NW storms had the weakest directional wind shear, veering slightly from west-southwest near the surface to westerly at 6 km altitude.

Standard deviations of V_r for the wind direction partitioning revealed some interesting characteristics. All storm categories had relatively larger standard deviation values lee of the Cascades, and areas east of KRTX. For the SE storms, there was large standard deviation within the Willamette Valley (8 – 9 ms^{-1}) and in the southwestern portion of the Coastal Range (**Fig. 15b,d,f**). S-SW storms had weaker overall standard deviation than the SE storms. There was smaller standard deviation in V_r near 4 – 7 ms^{-1} west of the radar and along the Cascades. W-NW storms overall had the smallest standard deviation over the Willamette Valley than the other storm averages, with values ranging from 2 – 7 ms^{-1}. For **Figure 15g-j**, the 1 km radar data for the same wind direction averages better describes the low-level flow associated with each wind direction category. All horizontal plots are taken at 2 km altitude to show the overall precipitation coverage and the lowest level where the majority of the flow is unblocked by the terrain.

For SE storms, standard deviation of V_r close to the surface was larger than with S-SW and W-NW storms (**Fig. 16b,d,f**). Upper-level standard deviation during S-SW storms were similar to those of SE storms. Below 3 km altitude, S-SW standard deviation tended to be smaller than that of SE storms (7 ms^{-1}). Standard deviation east of the radar was more uniform with height, but midlevel values west of the radar were more variable and disorganized with values ranging from 4 – 9 ms^{-1}. W-NW storms had the smallest standard deviation V_r values overall.

The SE storms tended to have precipitation frequency values that ranged between 40 – 50 % across the horizontal radar domain, with some enhancement in the southern Coastal Range and in some spots over the Cascades (**Fig. 17a,c,e**). The S-SW storms showed values of 45 – 60 % precipitation frequency over both mountain ranges. Precipitation frequency was higher in the northern part of the Cascades near the Columbia River, with more uniform enhancement over the entire Coastal Range. The precipitation frequency of W-NW storms was slightly greater and more uniform in coverage over the Cascades than S-SW storms. Precipitation frequency values ranged from 50 – 65 %, and higher values tended to be confined mid-slopes of the Cascades. Precipitation frequency of W-NW storms over the Coastal Range was more scattered than the other wind directions, with maximum values of 45 – 50 %.

The vertical cross sections of precipitation frequency for SE storms showed values in the Coastal Range at 45 – 50 %, but there was only slight increase (45 %) in frequent precipitation frequency over the Cascades compared to the Willamette Valley (40 %) (**Fig. 17b,d,f**). S-SW storms had a similar precipitation frequency values (45 – 50 %) over the Cascade and Coastal Ranges. The S-SW storms have the largest precipitation frequency over elevated terrain than other wind directions. W-NW storms had little increase in precipitation frequency values along the Cascade in comparison to the Willamette Valley, though had slightly higher precipitation frequency values than S-SW storms over the Cascade Range.

3.2 Cross-barrier wind speed

Approximately 78 % of storms had layer averaged wind directions from 180º - 260º azimuth. To examine the impact of cross-barrier wind speed on precipitation distribution, we examine storms within the 180º - 260º wind direction, which were then separated into subcategories of cross-barrier wind speed weaker and stronger than 9 ms^{-1} (**Fig. 18a-d**). Comparing the horizontal cross sections, the lower wind speed category revealed radial wind speeds around 10 ms^{-1} near the surface up to 20 ms^{-1} above 4 km altitude, whereas the higher wind speed category's V_r was 15 – 25 ms^{-1} within the same vertical layer. The wind direction veered for weak cross-barrier flow, going from near southerly at 1 – 2 km altitude to near southwesterly above 4 km altitude. The stronger cross-barrier flow storms veered less with height and had a more westward flow component in the upper levels. As expected, stronger cross-barrier flows tended to have larger wind speed gradients, with wind speeds around 15 ms^{-1} along the mid-slope of the Cascades. The weaker cross-barrier category had weaker winds near ~9 ms^{-1} in the same location.

Overall for both strong and weak cross-barrier flow, the standard deviations of V_r increased with height. Stronger cross-barrier storms had lower variations of standard deviation in the upper levels. The Cascade Range tended to have the small V_r standard deviation of 3 – 6 ms^{-1} (**Fig. 18e-h**). Both cross-barrier flow categories had large V_r standard deviation in the lee of the Cascades. The Willamette Valley contained standard deviation of V_r values greater than those over the Coastal and Cascade Ranges. Standard deviation for lower wind speed storms were greater towards the southeast portion of the radar coverage area, where both cross-barrier categories had similar mid- and lower-level standard deviation values of V_r.

Precipitation frequency values were larger (+ 20 %) for the stronger cross-barrier winds as opposed to the weaker cross-barrier winds along elevated terrain (**Fig. 19a-d**). Storms with stronger cross-barrier winds had precipitation frequencies in excess of 65 – 70 %, especially in locations over the Coastal and Cascade Ranges. This apparent result is related to the two largest total precipitation volume storms (**Fig. 14e**) falling into the strong cross-barrier wind speed and storm volume categories rather than a systematic relation between cross-barrier wind speed and storm volume. **Figure 19e,g** show the horizontal and vertical cross sections of the two storm average, which shows very high precipitation frequency values (> 80 %) over much of the radar volume. Storms with weaker cross-barrier winds generally had maximum precipitation frequencies (50 – 60 %) over both mountain ranges. There was little difference in precipitation frequency between flow strength categories in the southern Cascades. The difference in precipitation frequency between both data subsets was small above 5 km altitude. Based on **Figures 14 and 19**, stronger upslope forcing can lead to more frequent rainfall, but does not always as seen with **Figure 19f,h**. In comparison to **Figure 19b,d**, the strong cross-barrier storms without the two largest accumulated volumes is slightly less in precipitation frequency magnitude (< 5 %). The Willamette Valley tended to have smaller variation in precipitation frequency than higher elevations, with standard deviations of precipitation frequency about + 5 % larger in the stronger wind speed cases.

3.3. Brunt-Väisälä frequency

B-V was used to partition storms into unstable and neutral-stable storms. Categories of unstable (BV < 0) and neutral-stable storms (B-V ≥ 0) are focused on the 180º – 260º azimuth layer averaged wind direction storms. Looking at the horizontal mean Vr cross sections, the wind pattern for both storm averages were very similar (**Fig. 20a-d**). Wind magnitudes were slightly stronger in the upper levels (7 – 8 km) by 5 ms^{-1} for the unstable cases. Stronger winds were observed above the Coastal Range in the unstable case (~20 ms^{-1}) in comparison to the stable case (~15 ms^{-1}).

Both stable and unstable storms had large standard deviation close to the radar (**Fig. 20e-h**). Stable storms appeared to have larger standard deviation V_r within the Willamette Valley region (8 – 10 ms^{-1}) compared to unstable storms (~7 – 8 ms^{-1}). Standard deviation of V_r over the Coastal and Cascade Range were also larger by 1 – 3 ms^{-1} for stable storms. Stable storms had a large V_r standard deviation (8 – 10 ms^{-1}) towards the southeast. Vertical cross sections showed similar V_r standard deviation values in the midlevels (3 – 6 km) for unstable storms and stable storms. In the lower levels (1 – 3 km), stable storms tend to have larger standard deviation by 1 – 2 ms^{-1}, especially over the Pacific Ocean and Coastal Range, than unstable storms.

Overall, the differences in the stability of storms yielded no large differences in precipitation frequencies or spatial distributions (**Fig. 21a-b**). Maximum precipitation frequency values ranged around 50 – 55 % for both storm cases, and the qualitative patterns among both storm types were similar. Locations around the Coastal and Cascade Ranges showed areas of enhanced precipitation in similar locations for both stability cases. The overall pattern of frequent precipitation was similar among both unstable and stable storm types vertically. Cross sections of precipitation frequency revealed similar characteristics, though the stable cases appeared to have slightly higher (< 5%) precipitation frequency values than the unstable cases in some locations.

3.4. Time-accumulated precipitation volume

An in-depth comparison of the larger and smaller volume storms for 180º – 260º azimuth was performed to note key differences and similarities (**Fig. 22a-d**). As shown by the black line in **Figure 14a**, a threshold value of 2 x 10^7 km^3 was selected as the separation between larger and smaller storm volumes. The mean V_r between large and small storms had horizontal and vertical cross sections that were similar to one another at low levels. Larger storms have stronger middle and upper level winds as observed in vertical cross sections. V_r of at least 20 ms^{-1} are observed at 4 km altitude and higher over the Cascades of the large storm vertical cross section, whereas the same cross section for smaller storms had similar values at around 5 km altitude.

For large and small storms, slightly larger standard deviation was observed over the Willamette Valley (7 – 9 ms^{-1}) than those over the Cascades (5 – 7 ms^{-1}) (**Fig. 22e-h**). As with previous standard deviation partitions, areas lee of the Cascades and west of the Coastal Range over the Pacific Ocean showed larger standard deviation (8 – 12 ms^{-1}). For large vs. small volume storms similar values were present in the lee of the Cascades, but smaller standard deviations of 5 – 8 ms^{-1} were observed over the Pacific Ocean for larger volume storms. Vertical cross sectional views showed larger standard deviations closer to the surface for smaller volume storms than for those with large volume characteristics. Near surface (1 – 2 km), both types of storms had similar standard deviation, especially over the Cascades and Coastal Range.

Qualitatively the spatial patterns of precipitation frequency are similar but with different magnitudes, with higher precipitation frequency values along the Coastal and Cascade Ranges in larger volume storms. This suggested that the spatial pattern of orographic enhancement of precipitation occurred independently of time accumulated storm size (**Fig. 23a-d**). The locations of orographic enhancement do not change, rather the frequency of precipitation at a certain location changes. Larger storm volumes revealed more precipitation frequency occurring south of the radar location in the Willamette Valley compared to smaller volume storms. Vertical cross sections south of the radar location show the same precipitation frequency magnitude difference seen in the horizontal cross sections from MSL to 4 km altitude. The vertical cross section for smaller volume storms showed a smaller increase in precipitation frequency magnitude (~ 45 – 50 %) over the Cascades in comparison to Willamette Valley values of (40 – 45 %), while larger volume storms showed a larger increase (~ 60 – 65 %) over the same location compared to the Willamette Valley (50 %).

Hovmoeller plots (Yanluan Lin, personal communication) examined the vertical radar reflectivity between examples of small and large volume storms (**Fig. 24a,b**). The small volume storm (4 Nov 2005) had a storm accumulated volume of 1×10^7 km^3 while the large volume storm (30 Dec 2005) had an accumulated volume of 2.3×10^7 km^3. In comparison to the Smith et al. (2003) Hovmoeller plot for MAP case IOP2b, the small or large volume storm does not have an apparent enhancement of precipitation over the first peak of the terrain (**Fig. 24c**). The small volume storm appears to have more intermittency and has precipitation produced further upwind from any major terrain peaks. The large volume storm has more persistent precipitation which it appears to be nearly constant throughout the time period and extends further upwind and downwind of the mountain barriers.

Chapter 4. Radar & Model Data Comparison Results

In this section, we compare model output for 2005 – 06 winter storms to operational radar observations. Model runs and output were provided by Dr. Brian Colle of Stony Brook University. The 2005 – 06 storms were processed using 1 km radar grid spacing to better compare to 4 km model output. We examine two main variables with the radar and model data - V_r and precipitation frequency. The Penn State/NCAR Mesoscale Model MM5 Version 3.7 in non-hydrostatic mode was utilized in this study. A 24-h MM5 simulation was completed twice daily at 0000 and 1200 UTC using 6 hour GFS analyses for initial and boundary conditions. Stationary 1.33 km, 4 km, and 12 km nested grids centered on the radar location are nested within a 36 km domain using a 1-way nested interface. For 2005 – 06 winter storms, model runs utilized the Thompson bulk microphysical scheme, which includes supercooled water and graupel as well as a Berry autoconversion from cloud water to rain. For these PNW runs, they used the Dudhia cloud radiation, "KF2" (newer Kain-Fritsch version), and ETA (M-Y) PBL.

Radial velocity for the model output was computed using the U and V model winds. Standard deviations of V_r were also calculated to note the variations in wind values within the storms. Storms were separated based on their wind direction using the three-year climatology categories (Chapter 2.4). Directly comparing radar reflectivity to model precipitation has been a controversial issue, as many studies have been performed to find some sort of relationship between both variables. In our study, in order to compare precipitation from the radar observations to the model output, precipitation frequency was calculated for the radar observations ($Z \geq 13$ dBZ) for all storm averages and subsets. The 13 dBZ value was then converted to a model precipitation frequency variable using the Hagen and Yuter (2003) relationship, which converts radar reflectivity to model mixing ratio. Model variables QR (rain content), QS (snow content), and QG (graupel content) are summed to create a total precipitation value (QT). We used a QT threshold of 0.015 g kg^{-1} as comparable to 13 dBZ in the radar observations. By calculating precipitation frequencies greater than the threshold values for both model and observational data sets we yield to something more comparable than model derived reflectivities.

In comparing SNOTEL model data in the western U.S. to radar observations (Yanluan Lin, personal communication), overall there appeared to be no real correlation for good, over, or under prediction storms. In **Figure 25a**, the overall plot is fairly similar to **Figure 13c** in that most storms are observed as neutral to slightly stable. Storms that had underpredicted snow tended to be more neutral to slightly stable. Storms that were predicted well tended to be skewed more towards slightly unstable to neutral than the other two categories. As in the three-year radar climatology, the radar accumulated storm volume to the cross-barrier wind speed plot for the 2005 – 06 season shows slight correlation between variables, with an increase in cross-barrier wind speed or total wind speed tending to have larger volume storms (**Fig. 25b,c**). However, there is no clear signature in wind speed or storm volume for the predictability of storms. This shows that the forecast quality is not a simple relation between observed stability, wind direction, wind speed, or storm volume.

4.1 Storm-averaged radial velocity

4.1.1 Southeast (SE) storms (4 storms, 59 hours of data)

The SE storm average has the worst representation by the model in comparison to the radar observations. The model wind directions were off by 20 º, with the radar observations having a more southerly component and the model output influenced by westward flow (**Fig. 26a,b**). The radar observations had much stronger winds, with up to 20 ms^{-1} difference in some locations. Along the vertical cross section of V_r, there are substantial differences, particularly a layer of lower magnitude winds to 4 km altitude in the model output which is not present in observations (**Fig. 26c,d**).

The V_r standard deviation of SE storms between radar observations and the model output also differs considerably. There is a striking difference in the pattern and magnitude of standard deviation between radar observations and model output. The observed V_r standard deviation ranges from 3 – 8 ms^{-1}, with the higher values observed over the southern Coastal Range and the Columbia River valley east of the radar **(Fig. 26e**). The model output, the highest V_r standard deviation had large regions of values > 10 ms^{-1} (**Fig. 26f**). Vertical cross sections of the standard deviation values show that there is considerable variability in V_r among the modeled SE storms compared to the observed SE storms at similar altitudes (**Fig. 26g,h**). This comparison shows that the model appears to have difficulty with predicting the wind direction and magnitude within storms coming from the SE. When the kinematics are incorrect there is little chance of producing a correct precipitation field. This large difference could be due to a small data set of only a couple of storms, or a result of less stable air coming from the south.

4.1.2 South/Southwest (S-SW) storms (53 storms, 792 hours of data)

The model performed better in representing the wind direction of S-SW storms (**Fig. 27a,b**). The directional magnitude of the radial velocities between observations and model were similar. V_r patterns indicate winds were slightly stronger near the surface (1 – 2 km layer) in observations. The cross sections of the vertical velocities showed wind magnitudes were very similar, with minimal difference between model and observations except near the surface (**Fig. 27c,d**).

The standard deviation of S-SW V_r storms provides evidence of steadiness of flow within the storms. The horizontal cross sections for the radar observations show similar standard deviation values of V_r as seen with the SE radar storms (**Fig. 27e**). Standard deviations are larger near the radar, in lee of the Cascade Range, and over the Pacific Ocean. The model standard deviation V_r shows similar values as the observed, but the location of large standard deviation is slightly different. There are large standard deviation values over the Pacific Ocean and near the radar similar to the radar observations. The model has large standard deviations near Mt. St. Helens and in lee of the Cascade Range (**Fig. 27f**). Large model standard deviation values tend to be concentrated parallel to the direction of the flow, just as in SE storms. At the midlevels between 2 – 5 km altitude, the standard deviation values are similar between the radar observations and model output. Above 5 km altitude, the values increase for both data sets (**Fig. 27g,h**).

4.1.3 West-Northwest (W-NW) storms (5 storms, 55 hours of data)

The representation of the wind field in the model was intermediate between the poor performance in SE storms and better performance in S-SW storms (**Fig. 28a,b**). The V_r magnitudes between radar observations and model output were similar, with a slight hint of the winds being stronger over the coastal areas in the radar observations. The vertical cross section revealed that observed winds were weaker by approximately 5 ms^{-1} above 5 km altitude in some locations compared to the model data (**Fig. 28c,d**). The observational vertical cross section showed this difference especially over the coast along the red line in the horizontal cross section.

The standard deviation of the V_r for the radar observations showed the largest standard deviation among all wind direction averages (**Fig. 28e**). Values of standard deviation of V_r are similar when compared to the model values (**Fig. 28f**). The W-NW storms did have larger standard deviation values located parallel to the flow. Large values of standard deviation are seen to the north-northwest and southwest of KRTX. The observations show large standard deviation values lee of the Cascade Range east of KRTX, which are not present in the model output. The radar observations show slightly larger standard deviation values by 1 – 2 ms^{-1} than the model data southwest of the radar. The model data shows slightly larger (1 – 2 ms^{-1}) concentration of standard deviation values to the northwest. Vertical cross sections of the V_r standard deviation show the higher deviation values over the southern portion of the Coastal Range in the observations and over the northern portion of the Cascade Range in the model output (**Fig. 28g,h**). Both show a similar range in deviation of 6 – 10 ms^{-1} below 6 km altitude. However, above 6 km altitude, the model shows a greater increase in deviation in comparison to the observations.

Overall, the wind directions and magnitudes compared well with wind directions containing some westerly component to it. But once the storms began having more of a southerly component to it, the model appeared to not handle the magnitude of the winds well and tended have more westward bias in the SE storm totals. Storm averaging helped average out anomalies but the smaller number of samples in SE and W-NW categories makes the results more uncertain.

4.2 Precipitation Frequency

4.2.1 SE storms

The radar precipitation frequency was low with SE storms, where most values tended to be in the range of 30 – 40 %, with maximum values of around 50 % in the southern portion of the Coastal Mountains (**Fig. 29a,b**). In comparison with the model frequency, the radar observations differed greatly with the pattern of precipitation. The model showed more enhancement in precipitation along the southern portion of the region. The radar data showed enhancement of precipitation over the Coastal Mountains, but showed a smaller increase in precipitation over the windward slope of the Cascades (35 %), where the model data had values of 65 – 75 %. The model vertical precipitation frequency showed great enhancement over the southern Coastal Mountains (**Fig. 29c,d**). The radar data revealed slight precipitation enhancement, but much less than the model. Gravity wave signatures, upwind tilted regions of higher precipitation frequencies aloft, were evident in the model, but were nonexistent in the radar observations over the Cascade windward slope. This difference in tilt of precipitation frequency structures could either be a result of the model overpredicting gravity waves or a correct prediction of gravity waves but overprediction of snow aloft associated with a given vertical motion, or some combination of the two.

4.2.2 S-SW storms

The observed precipitation frequency in S-SW storms increase in magnitude over the Cascade and Coastal Ranges as compared to the Willamette Valley (**Fig. 30a,b**). The spatial pattern of precipitation frequency is similar between radar observations and model output but the magnitudes are different. The model output shows a + 10 % increase in magnitude over the Coastal Range, and + 15 % or more over the Cascade Range compared to the radar observations. The vertical cross section shows evidence of upwind tilted structures of high precipitation frequency values (gravity waves) in the model output, and virtually none in the radar observations (**Fig. 30c,d**).

4.2.3 W-NW storms

The observed W-NW precipitation frequency is higher than other wind directions (**Fig. 31a,b**). Both radar observations and model output showed an overall increase in frequency over the Coastal and Cascade Ranges. The region of enhanced precipitation frequency extending further upwind of Cascade Range in model compared to observations.

The vertical precipitation frequency pattern suggested a gravity wave signature of upwind tilting of precipitation in the model data over the Coastal Range, yet was nowhere to be found within the observational data (**Fig. 31c,d**). There appeared to be enhanced precipitation along the slope of the Cascades in the observational data, but had no upwind tilting of precipitation as seen with the model data.

The qualitative comparison between the model and radar precipitation frequencies appeared to do fairly well in most cases of finding the correct areas where precipitation will be enhanced. However, not getting the correct frequency was quite troublesome, especially in an environment dominated by orographic precipitation patterns and forcing. The vertical precipitation frequencies showed similar patterns as the horizontal plots, though the model tended to over predict on upwind tilted precipitation structures associated with gravity waves compared to the radar observations.

4.3. 2005 December 29 – 31 storm

As well as examining average characteristics of multiple storms we also looked at some individual storms. Reanalysis plots of 30 Dec 2005 revealed tight surface pressure lines intersecting the Portland, OR region through the 24-h composite with low pressure centered towards the NW, thus SW flow dominates over the time period (**Fig. 32a**). An influx of surface precipitable water in excess of 32 mm is seen off the Northern California coast, which is consistent with the PDX total precipitation during this time period (~ 34 mm). This storm yielded one of the heaviest days of precipitation during our three-year study (**Fig. 32b,c**). Surface data from PDX and the sounding at 12 UTC 30 Dec 2005 from Salem, OR

(SLE) in **Figure 33a** showed surface temperatures during the time period ranging from 3° - 7° C (**Fig. 32e**). MRR plots of radar reflectivity taken from the same time period show that the freezing level during the storm is around 2.2 km (**Fig. 33b**).

From the SLE sounding, the layer-averaged wind direction was 219.5° azimuth, which placed it in the S-SW storm category, but the surface wind direction at PDX varied between 100° - 150° azimuth, placing the direction mostly from the S-SE (**Fig. 32f**). Surface pressure at PDX was around 1015 hPa at the beginning of the storm and gradually dropped to 990 hPa at around 0 UTC 31 Dec 2005 (**Fig. 32d**). The layer-averaged cross-barrier wind speed and moist B-V were 13.24 ms^{-1} (strong wind) and 0.22 x 10^{-3} s^{-1} (slightly stable) respectively. The storm accumulated volume was also in excess of the threshold of 2 x 10^7 km^3 (large volume). Thus, the storm covered a large volume with strong winds from the typical wind direction of most storms.

4.3.1 Mean and standard deviation of radial velocity

The horizontal cross section of mean V_r between the radar data and model observations compared well with respect to wind direction (**Fig. 34a,b**). Horizontal wind shear is low as the velocity patterns not do veer (shift to the right with height). The magnitudes of the wind speed differ, with the model showing slightly stronger velocities (20 ms^{-1}) in the 1 – 2 km layer than the radar observations (15 ms^{-1}) over the Cascade Range. The cross sections also showed an increase in wind magnitude as height increased (**Fig. 34c,d**).

The pattern of standard deviation values was significantly different between the radar observations and model output (**Fig. 34e,f**). Looking at the horizontal cross section, the standard deviation of observed V_r maximum values ranged up to 9 ms^{-1} over the Coastal Range. In the model data, standard deviation values ranged from 11 – 15 ms^{-1} north of the KRTX location. Standard deviation of V_r south of KRTX were similar between radar and model data, with smaller values (~ 5 ms^{-1}) in the Salem, OR region. Vertical cross sections of standard deviation are substantially different, with higher standard deviation values at around 8 km altitude (10 – 12 ms^{-1}) for both radar and model data sets (**Fig. 34g,h**). The model cross section also revealed high values below 1 km, but this level is difficult to compare due to the varying terrain height and no radar observations below this level. The midlevel (2 – 6 km altitude) section between the radar and model data was similar, with values ranging from 2 – 5 ms^{-1} standard deviation. Thus, the flow tended to be fairly similar above 2 km altitude for model and radar data throughout the duration of the storm.

4.3.2 Precipitation frequency

Unlike the analysis of the 2005 – 06 winter season, which showed that the model data always overpredicted the amount of frequent precipitation compared to a radar plot, the 29 – 31 Dec 2005 case showed the magnitude of observed precipitation frequency was similar to the model data. The horizontal cross section shows that the storm total precipitation frequencies for both the radar and model were similar, especially in the lower portion of the coastal and Cascade mountain ranges (**Fig. 35a,b**). Values in this area were from 60 – 85 % and differed by ± 5 % between both radar observations and model output. The radar observed higher precipitation frequency than the model did over the lower Willamette Valley region near SLE. The radar precipitation frequency was about + 15 – 20 % higher than was seen in the model. The vertical cross section showed high observed precipitation frequency values (75 – 85 %) over the Willamette Valley, while model maximum precipitation frequency values were low at 4 km altitude (**Fig. 35c,d**). Near the radar and to the north of the radar, the model contained higher precipitation frequency values.

The radar observations had persistent beam blockage to the north and east of the radar location due to the mountainous terrain in the Portland region, thus it was to be expected that the values would differ in this area. Windward slope precipitation enhancement was stronger in the radar observations than model output for this case, which differs from the 2005 – 06 storm averaged S-SW wind direction plots. The magnitude of the peak precipitation frequency values between the model and observations in this case are similar (~ 90%) but the vertical cross-section shape of the precipitation frequency maximums differ. The vertical cross section of potential temperature has a gravity wave signature manifested as downsloping potential temperature lines over the Cascade peaks. In the model, precipitation frequency is tilted upwind consistent with precipitation growth in gravity waves. The radar observations for the same cross section show nearly vertically oriented local maximum in precipitation frequency as in S-SW storm subset.

4.4 2006 November 6 – 7 storm

The 29 – 31 Dec 2005 storm case was a storm that had a significant amount of rainfall, though was not associated with any damaging results of flooding. Therefore, we decided to also compare the storm averages to an extreme case that caused extensive flooding in the PNW but was not a part of our three-year climatology. Reanalysis plots of 6 – 7 Nov 2006 revealed tight surface pressure lines similar to the 29 – 31 Dec 2005 case intersecting the Portland, OR region through the 24-h composite with low pressure centered towards the NW and SW flow dominating over the time period (**Fig. 36a**). An influx of surface precipitable water in excess of 40 mm is seen off the Oregon coast, higher than observed with the 29 – 31 Dec 2005 case, and the PDX data shows over 100 mm of rainfall was observed over the 48-h duration of the storm (**Fig. 36b,c**). Surface data from PDX and the sounding at 0 UTC 7 Nov 2006 (SLE) in **Figure 37a** reported the temperatures during the time period ranging from 14° - 19° C making this an unusually warm event for a winter storm (**Fig. 36e**).

MRR plots of radar reflectivity taken from the same time period show that the freezing level increased during the storm to near 4 km altitude at 0 UTC 7 Nov 2006 and lowers to near 3 km altitude towards the end of the period (**Fig. 37b**). The layer-averaged wind direction was 213.6° azimuth, which placed it in the S-SW storm category (**Fig. 36f**). Surface pressure at PDX was around 1015 hPa at the beginning of the storm and gradually dropped to 1005 hPa a few hours before 0 UTC 7 Nov 2006 (**Fig. 36d**). The layer-averaged cross-barrier wind speed and moist B-V were 15.02 ms^{-1} (strong wind) and 7.7165 x 10^{-5} s^{-1} (slightly stable) respectively. The storm accumulated volume was also in excess of the threshold of 2 x 10^7 km^3 (large volume). Similar to the 30 Dec 2005 case, the storm covered a large volume with strong winds from the typical wind direction of most storms.

4.4.1 Mean and standard deviation of radial velocity

Horizontal radial velocity plots between radar observations and model output show that the wind direction flows from the SW (**Fig. 38a,b**). Model V_r magnitudes are stronger by 3 – 5 ms^{-1} in the lower levels (below 3 km altitude). Vertical cross sections of the radar observations and model output show that the model has stronger wind velocities in the upper levels (above 4 km altitude), by as much as 20 ms^{-1} in some locations (**Fig. 38c,d**). V_r radar observations greatly differ from the model output, with the model having stronger flow that comes from a more westerly direction. Radar observed V_r is more from the SW and is much weaker in magnitude, especially in the upper levels.

Standard deviation of V_r shows small values ranging from 2.5 – 6.5 ms^{-1} for the radar observations (**Fig. 38e,f**). The model output also shows a similar range in values, except for the large standard deviation of V_r (6 – 12 ms^{-1}) along portions of the Coastal and Cascade Ranges. The large values appear to be near locations where the V_r is strong, and also nearly parallel to the flow. This pattern of high standard deviation values parallel to the flow is also evident in the radar observations, but is much lower in magnitude compared to the model. Vertical cross sections show that the radar and model data are similar in the lower levels (2 – 3 km altitude) in the cross section parallel to the flow (**Fig. 38g,h**). Above 3 km altitude, the standard deviation values of V_r in the radar observations have a large positive vertical gradient in values (from 7 ms^{-1} at 3 km altitude to greater than 16 ms^{-1} at 5 km altitude) compared to the model output (5 – 7 ms^{-1} in the same vertical layer).

4.4.2 Precipitation frequency

In the 6 – 7 Nov 2006 storm case, the precipitation frequency between both the radar observations and model output are different than the 29 – 31 Dec 2005 case (**Fig. 39a,b**). Precipitation frequency values in excess of 90 % are seen along the northern Cascade Range for both data subsets. The model shows more coverage of high precipitation frequency values, especially over the Coastal Range, thus showing the model over predicts frequency of precipitation. The vertical cross sections between the radar observations and model output are similar, with high precipitation frequency values (60 – 90 %) over both mountain ranges (**Fig. 39c,d**). The cross section taken along the southern portion of the KRTX coverage area shows slightly higher precipitation frequency values along the Coastal Range for the radar observations, while the model output shows slightly higher precipitation frequency values along the windward slopes of the Cascades. Also, the model output shows more upwind tilting of precipitation frequency than in the 30 Dec 2005 case, with potential temperature lines dipping further in height, yet no gravity wave signature is found within the radar observations.

Chapter 5. Discussion

5.1 James and Houze (2005)

JH2005 interpreted 3D radar data over a 2.5 year period in Northern California coastal mountain storms centered at Eureka, CA (KBHX). They showed that the 3D pattern of precipitation was generally stratiform throughout the radar coverage area. The storm characteristics were associated with unstable, unblocked cross-barrier flow on both mountain slopes (King Range along the coast and South Fork Mountains further inland). A strong area of maximum reflectivity was seen over the first major terrain peak, and less enhanced precipitation areas along secondary peaks. Enhanced precipitation offshore and over the coastal mountains was evident in all storms. Orographically enhanced precipitation features were more distinct with a strong 500 – 700 hPa flow, high midlevel humidity, and strong low-level cross-barrier wind component.

JH2005 storms tended to have more unstable air than our Pacific Northwest storms. JH2005 used a slightly smaller layer average (1 – 2 km altitude) compared to 0.61 - 2.2 km altitude in our study. Also, stability values from JH2005 were derived over the Pacific Ocean with the NCEP Eta Model grid, while our study's stability was taken over the Willamette Valley using the nearby Salem operational upper-air sounding. Similar to our study, precipitation areas for the Eureka case were larger for stable storms than unstable storms. Their finding for Northern California is similar to the moist B-V versus wind direction plot in **Figure 13c**, where larger area storms tend to be more stable. The JH2005 winter season (1 October – 31 March) is one month longer than our winter season (1 Nov. – 31 March). Low-level cross barrier wind in Northern California from the southwest had similar magnitudes to our climatology study for the PNW. Cross-barrier flow enhanced terrain-induced precipitation over the Coastal Range and over the inland Sierras Range.

5.2 Medina and Houze (2003)

During MAP, data were collected for fourteen storms from 7 September to 15 November 1999. MH2003 used mean soundings from Milano, Italy, which is located between the Apennines and Alpine mountain ranges, to analyze two storm cases - IOP2b (unstable, unblocked flow case) and IOP8 (stable, blocked flow case). Both storm cases had extensive rainfall and exhibited similar upper-level wind speeds. However, for IOP8, the stability and weak winds below 900 hPa prevented the air flow from rising over the Alps. There were also microphysical differences between both storms, with IOP2b exhibiting convective features such as graupel over the first peak of elevated terrain. IOP8 produced precipitation, but it had more of a stratiform nature (**Fig. 5**).

The MAP experiment has a much smaller data set than either JH2005 or our study, which had 117 storms during the three-year period. Southerly flow and southeasterly flow across the Apennines and Alps is described for IOP2b and IOP8. The source of moisture for MAP storms was the Mediterranean Sea, while the Pacific Ocean was the moisture source for our study. The MAP study may have experienced more unstable atmospheric flow due to the Mediterranean Sea being warmer by around 5 °C (1.5 km average depth) than the Pacific Ocean (4.2 km) (NCEP SST Reanalysis). Higher SSTs yield more evaporation for a given wind flux, creating more transport of water vapor over the Apennines and Alps. Low-level cross-barrier wind speed was also stronger for the unstable case (IOP2b) compared to the stable case (IOP8) in the Lago Maggiore region of MAP, similar to our findings.

5.3 Medina et al. (2007)

Medina et al. (2007) used the IMPROVE-2 radar data (Nov – Dec 2001) set over the central Oregon Cascades as well as SLE sounding data to obtain thermodynamic variables for sixteen troughs that passed through the area. This study also made use of the National

Center for Atmospheric Research (NCAR) S-band dual-polarized radar imagery to identify different precipitation particle types, which was not available for our study. Medina et al. (2007) analyzed winter storms based on three basic storm structures: leading edge echo, double maximum echo, and shallow convection echo. One storm case (28-29 November 2001) was compared to the three basic echo structures to see how it differed from other IMPROVE-2 storms.

The typical sequence of storm structures involved the leading edge echo descending from upper levels to the surface as warm air advection lifted the low level air. The double maximum echo had two levels of where the echo is at a maxima: the freezing level and 1 – 2.5 km above that, where it becomes well-defined over the windward slope of the Cascade Range. The higher level echo maximum may result from the aggregation of large particles and from dynamic enhancement due to gravity waves. Finally, during the shallow convection echo period, flow is postfrontal with little to no shear and precipitation falls out of decaying updrafts. Our data has insufficient vertical resolution in order to resolve the double maximum echo seen in the Medina et al. (2007) study. The IMPROVE-2 study of Medina et al. (2007) had a two-month window (Nov – Dec 2001) to analyze storms and extensively analyzed only one storm case. Signatures of warm air advection were apparent in most of the storms examined in the Medina et al. (2007) study, similar to our storm averages for S-SW storms.

Chapter 6. Conclusions

Previous studies of orographic precipitation have yielded numerous finding regarding the factors that help enhance precipitation over the windward slope of a mountain. However, few have undertaken thousands of volumes of radar data and compared it to model output. Preliminary climatological data from PDX, V_r and radar reflectivity data were used to select the 117 storms that occurred during three winter seasons (1 November – 31 March) in Portland, OR from 2003 – 2006. Sounding data was also obtained from Salem, OR for the same time period, and the resulting thermodynamic variables were used to analyze storm characteristics to determine dominant features during winter storms. MM5 mesoscale model output was also obtained for the 2005 – 06 and 2006 – 07 winter seasons to compare to 3D radar observations to see how well the model performed for storm averages and individual cases.

Wind direction is the dominant feature in determining the spatial pattern of precipitation for Portland area storms, having greater influence than the cross-barrier wind speed or the stability of the flow. The Precipitation-elevation Regression on Independent Slopes Model (PRISM) rainfall map by Daly et al. (1994) showed an increase in rainfall with higher altitude along the Cascades, which is not consistent with our study. We found the typical precipitation enhancement mid-slope rather than at the crest of the Cascade Range and at the crest of the Coastal Range.

Wind direction was the primary control on locations of precipitation enhancement in the Portland, OR region. South and southwesterly-type storms represent 84 % of storms in the Portland region and often had the greater chance for frequent precipitation due to the strong flow associated with them. W-NW storms had the weakest wind magnitudes and lowest V_r standard deviation of the three wind categories, with S-SW and SE storms (highest V_r standard deviation) having similar magnitudes. On the other hand, W-NW storms had slightly higher precipitation frequency values than S-SW storms along the Cascade slopes. But S-SW storms had the largest areal coverage of precipitation frequency > 50 % over both mountain ranges.

When making a distinction between weak and strong flow storms for S-SW storms, the strong wind speed storms had more veering associated with them and had stronger wind magnitudes throughout the vertical layer. The storm groups had little difference between one another with their standard deviation of V_r values. Strong wind speed storms produced more frequent precipitation over both mountain ranges, and had higher precipitation frequency values throughout the coverage area than the weak wind speed storms.

V_r and standard deviation of V_r plots revealed little differences in wind direction and magnitude between stable and unstable storms. Most storms during our three year study were neutral to stable and were associated with the cool, moist Pacific Ocean air flow and the non-convective nature associated with the stratiform systems. Difference in stability yielded only a small change in spatial pattern of precipitation frequency, with only changes along locations in the Cascade Range.

Increasing the storm-accumulated volume was primarily related to increasing the precipitation frequency rather than increasing the area of precipitation coverage. Large volume storms had stronger upper level winds, with dominating S-SW flow associated with them. V_r plots showed that wind directions and magnitudes differed slightly between large and small volume storms. Standard deviation of V_r averages for large volume storms show smaller standard deviations in wind magnitude over the Pacific Ocean, compared to small volume storms. Large volume storms produce much more frequent precipitation along both mountain ranges than small volume storms. However, having a strong cross-barrier flow or wind speed did not necessarily mean the storm accumulated volume would increase. Time-distance plots show more intermittency in small volume storms while large volume storms were more persistent.

For the comparison between radar observations and model output, the forecast quality was not a simple relation of observed stability, wind direction, wind speed, or the storm accumulated volume. In separating the storms by their prevailing low-level wind direction, S-SW storms were still the more frequent storm observed for the 2005 – 06 winter season. SE storms appeared to have the largest difference between Vr and standard deviation of V_r patterns in the radar and model, while W-NW storms had weaker flow overall. Overall, the model overpredicts the precipitation frequency coverage, but the spatial pattern between radar observations and model output is predicted well. Upwind tilted precipitation structures associated with gravity waves are apparent in the model output, especially in the S-SW storms, but are not present in the radar averages. This difference in upwind tilting precipitation frequency structures was either a result of the model overpredicting gravity waves or a correct prediction of gravity waves but overprediction of snow aloft associated with vertical motion, or some combination of the two.

The two individual storm cases examined showed slightly different results, with mean wind directions and speed in the model having significant errors. The model tends to show higher values of Vr standard deviation because of this, partly as a result of “shocks”, or jumps due to the 12-h model runs. Precipitation frequency seemed to be modeled better for individual storms examined, perhaps due to the heavy precipitation observed in these storms and the S-SW flow associated with them. However, the model still overpredicted on the amount of frequent precipitation observed. Upwind-tilted precipitation structures associated with gravity waves were present in the 3D MM5 model and frequently appear in 2D simulations such as in Colle (2004). However, the radar observations examined in this study tended to have vertical reflectivity structures with little to no evidence of upwind tilting of precipitation related to gravity waves.

Similar to JH2005 analysis of Eureka, CA, we saw large changes in the geographic pattern of precipitation associated with different low-level wind directions. For 2 km altitude multi-storm average horizontal cross-sections, they also saw very different patterns of precipitation with varying cross-barrier wind strength. In contrast, we saw similar patterns with varying cross-barrier wind strength but changes in precipitation frequency magnitude. Although they do not provide a figure showing squared moist B-V versus cross-barrier wind speed, since most of their cases were unstable we can surmise that part difference in results comes from their inclusion of more unstable cases in both cross-barrier wind speed categories than we had.

In Medina and Houze’s (2003) analysis of southern Alps storms, they found clear cut cases of blocked and unblocked flow with precipitation enhancement upwind of terrain in stable (blocked) case and precipitation enhancement at first peak in terrain in the unstable (unblocked) case we did not see clear indication of either. Our precipitation was typically most enhanced mid windward slope and for some cases at crest. The Alps (crest altitude 3 – 3.5 km) forms a much higher and steeper barrier than the Cascade Range (crest altitude 1.8 – 2 km). The more gentle slope of the Cascade Range in Oregon likely posed less of an obstacle to blocked flow yielding less precipitation enhancement in the valley and more over the slopes. Colle's (2004) idealized 2D simulations (his Fig. 4) shows increasing building back of precipitation upstream as the mountain height and slope increased for stable flow.

Medina et al. (2007) examined a portion of the Oregon Cascades to the south of our study area. We concur with their study that freezing level heights in this region can vary up to several km in altitude during storms. This was the primary reason why we used precipitation frequency rather than average reflectivity to represent the precipitation field. The conceptual model summarizing their findings (**Fig. 7**) shows most precipitation enhancement on lower slopes and over the Willamette valley. In contrast, we saw infrequent precipitation over the valley compared to the windward slopes and more enhancement on the mid slopes as compared to the lower slopes. Given that Medina et al. (2007)'s study and our study examine the same time of year and the same general geographic location these differences are surprising. However, their study area of central Oregon has foothills extending further west compared to our area of northern Oregon/southern Washington. Also, they used E-W vertical cross-sections to describe storms with SW flow whereas we used SW-NE cross-sections that were more parallel to the low-level flow. This study examines 117 storms compared to Medina et al.(2007)'s 4. It may be that their 4 storms are not representative of the longer term average. Differences in methodologies and sample size are likely contributed to the differences in the findings.

In all, the ideal setup for a larger precipitation volume storm in the Portland, OR area requires a wind direction from the 180° – 260° azimuth, wind magnitude greater than 9 ms^{-1}. The location of locally intense rainfall along the windward slopes can be roughly determined from the layer-averaged wind direction. The model would have a good representation on the spatial pattern of the precipitation, but problems with forecasting precipitation frequency. Model output also has trouble with modeling the wind direction and speed, especially for the SE and W-NW storms. Precipitation appears to be produced at a maximum mid-slope and not at the crest of the Cascades, while increasing the volume is mainly related to increasing precipitation frequency. Thus, these storm averaged characteristics can be applied to short-term weather forecasting in hopes to reduce the costly damage done from future heavy precipitating events.

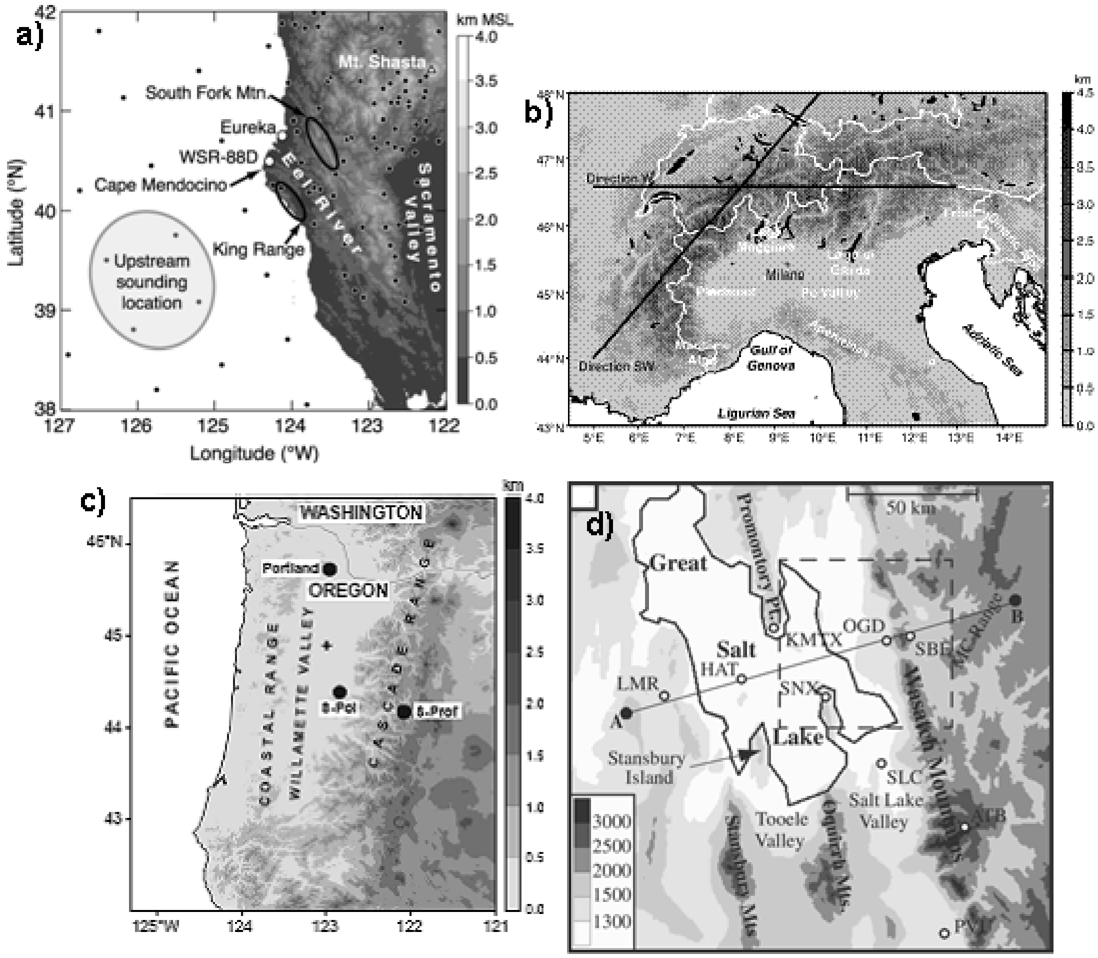

Fig. 1. (a) Map of northern California orographic storm study from 2002 – 2005 (from James and Houze 2005). (b) Map of the MAP case study for the Lago Maggiore region in Italy from Nov – Dec 2001 (From Medina and Houze 2003). (c) Map of IMPROVE-2 case study for the Portland, OR region from Nov – Dec 2001 (From Medina et al. 2007). (d) Topographic map of the IPEX case study in the Wastach Mountains in Utah for 12 February 2000 (From Colle et al. 2005).

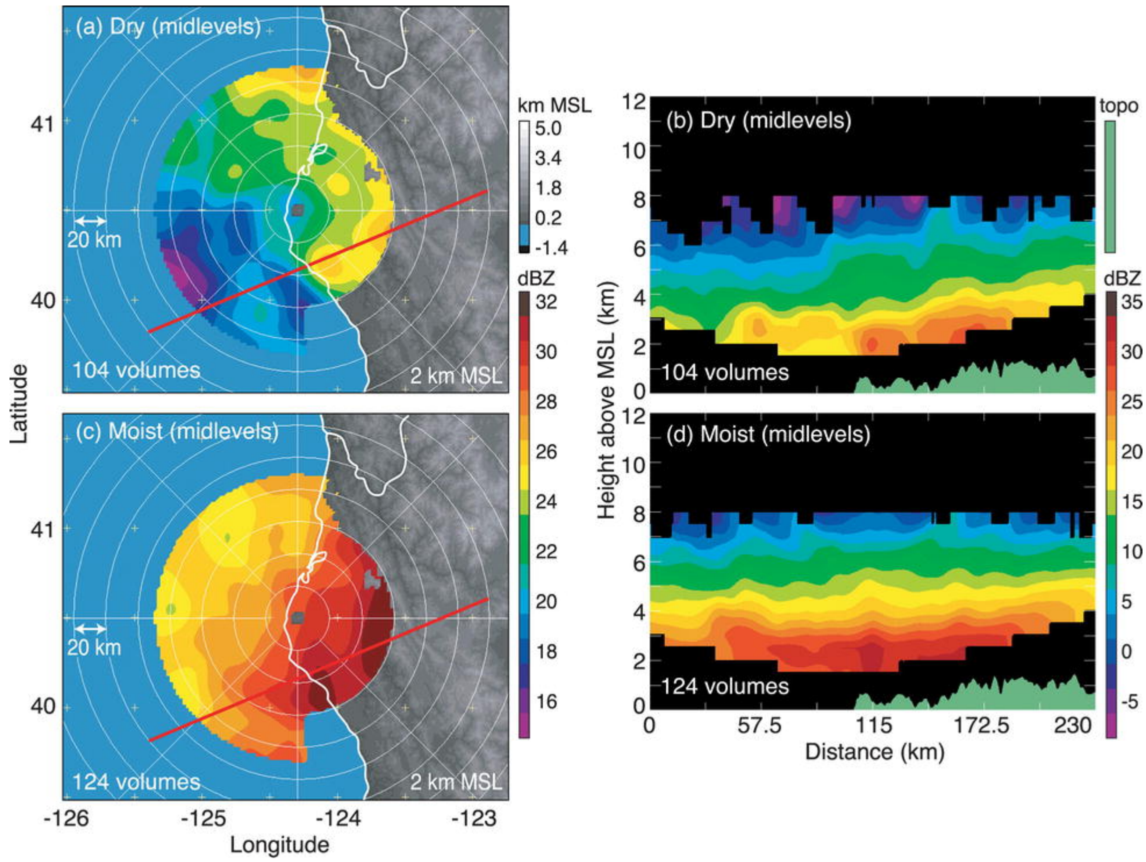

Fig. 2. Subset of radar volumes where the 700 – 500 hPa layer-averaged dewpoint depression was (a) at least 3°C and (c) less than 3°C for mean reflectivity at 2 km MSL. (b) and (d) Vertical cross sections respective to (a) and (c) along red lines in horizontal cross sections and terrain profile shaded green. Range ring spacing is 20 km with azimuth lines drawn every 45° (From James and Houze 2005).

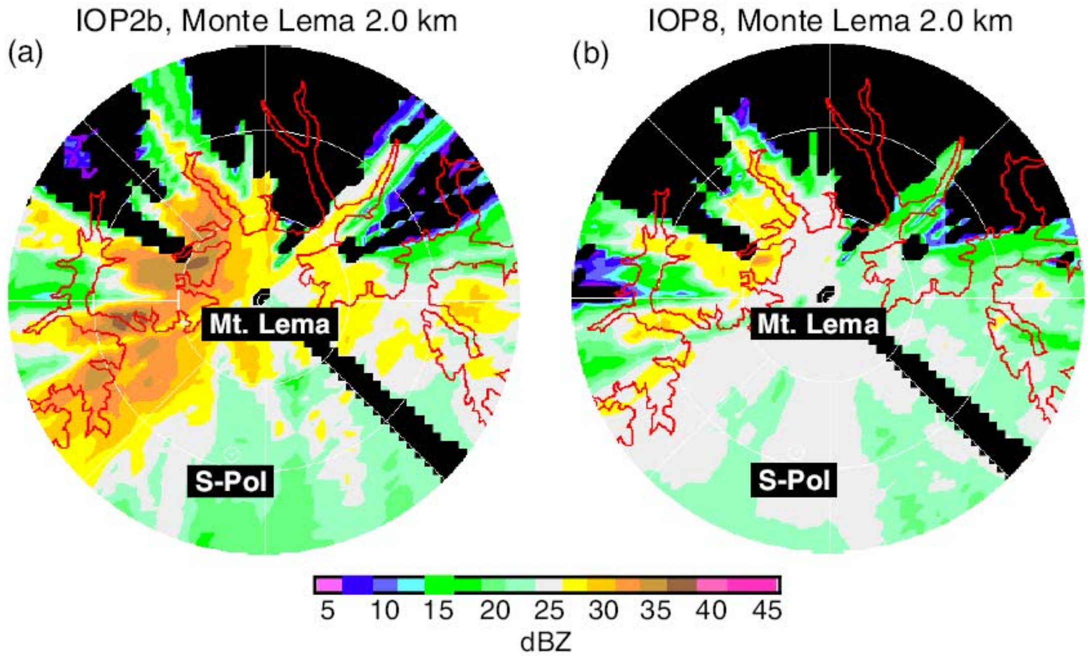

Fig. 3. Constant-altitude plots at 2 km showing the storm-mean reflectivity observed by Monte Lema radar for (a) IOP2b (1300 UTC 19 September to 0100 UTC 21 September 1999) and (b) IOP8 (1200 UTC October to 2200 UTC 21 October 1999). The 800 m terrain is shown in red. Range ring spacing is 20 km. Heights are MSL (From Medina and Houze 2003).

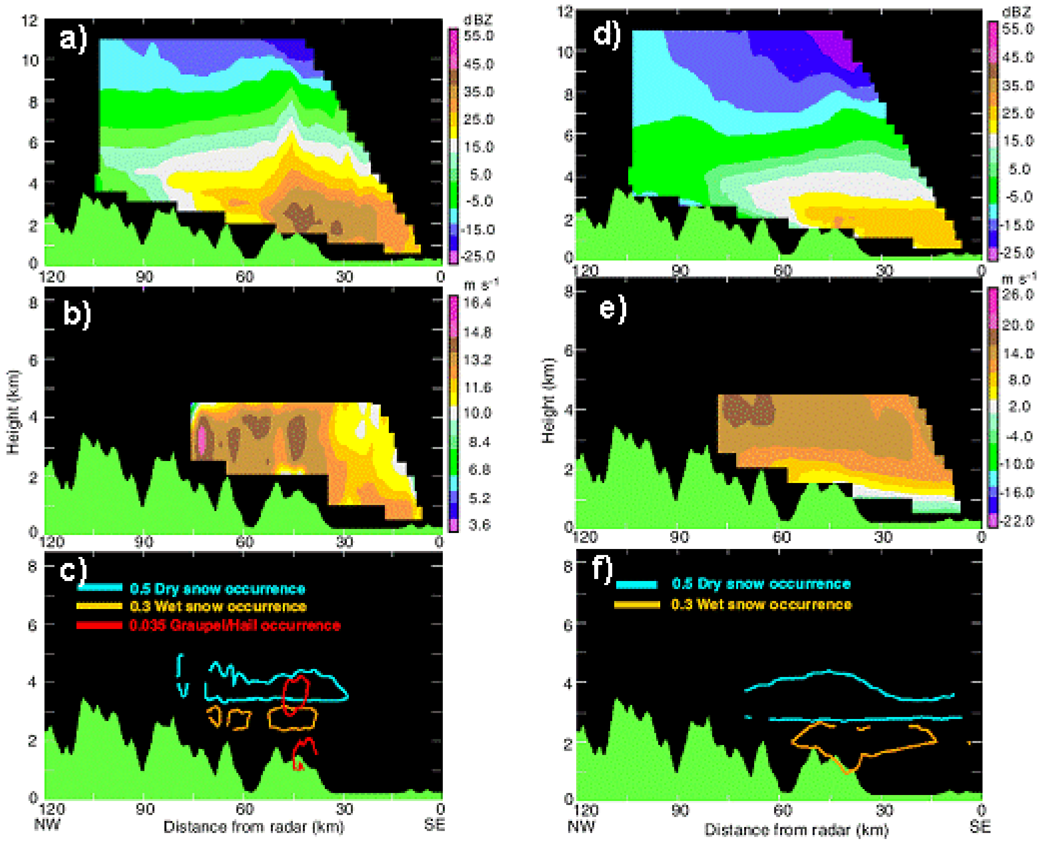

Fig. 4. Vertical cross section of the S-Pol radar storm-mean fields during IOP2b (left) and IOP8 (right). (a) Mean reflectivity, (b) mean radial velocity (positive values denote outbound flow), and (c) frequency of occurrence of particle types identified by polarimetric radar algorithms (From Medina and Houze 2003).

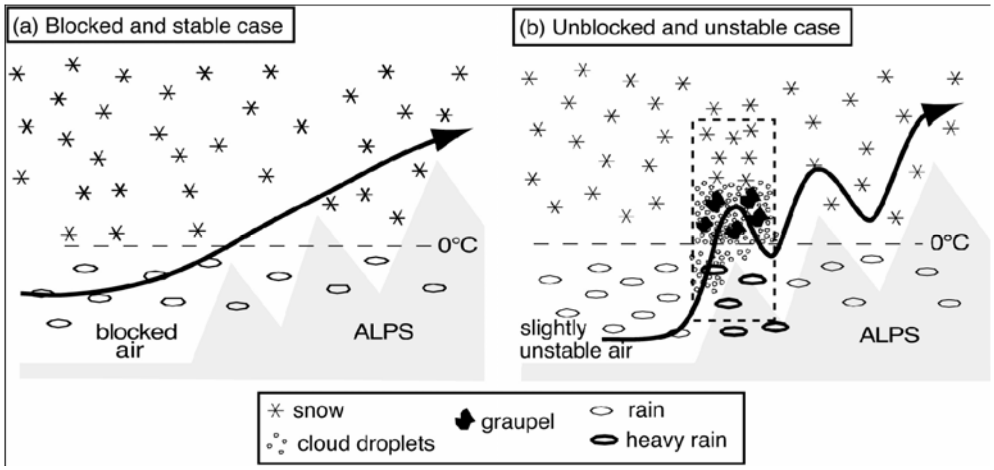

Fig. 5. Conceptual model of the orographic precipitation mechanisms active in (a) stable blocked, and (b) unstable unblocked flows. The diagrams show the types of hydrometeors present in each case, along with the behavior of the flow. The dashed box in (b) indicates the position of the embedded convective rain shower and graupel (From Medina and House 2003).

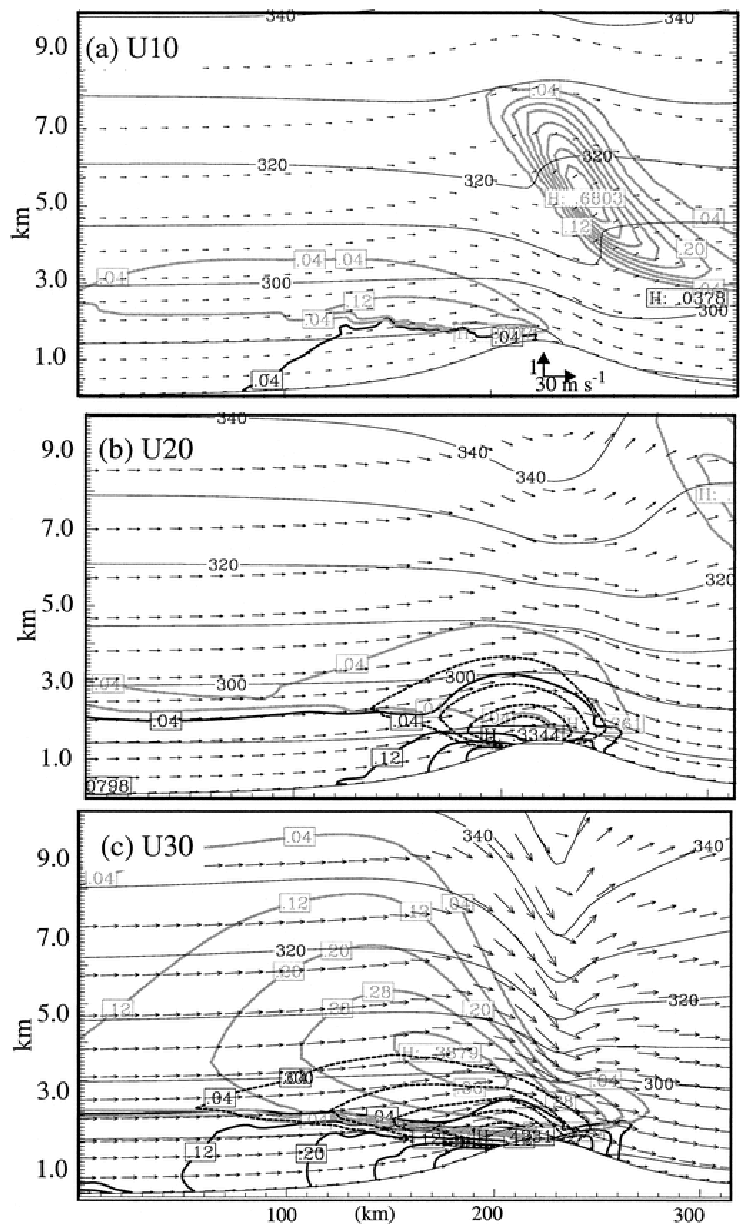

Fig. 6. Idealized 2-D cross section of potential temperature (solid every 10 K), wind vectors, snow (gray-dashed), graupel (black-dashed), and rain (solid) mixing ratios every 0.08 g kg^{-1} starting at 0.04 g kg^{-1} for the cases of increasing wind speed perpendicular to the mountain for (a) cross-barrier wind speed at 10 ms^{-1} (U10), (b) cross-barrier wind speed at 20ms^{-1} (U20), and (c) cross-barrier wind speed at 30 ms^{-1} (U30) experiments (From Colle 2004).

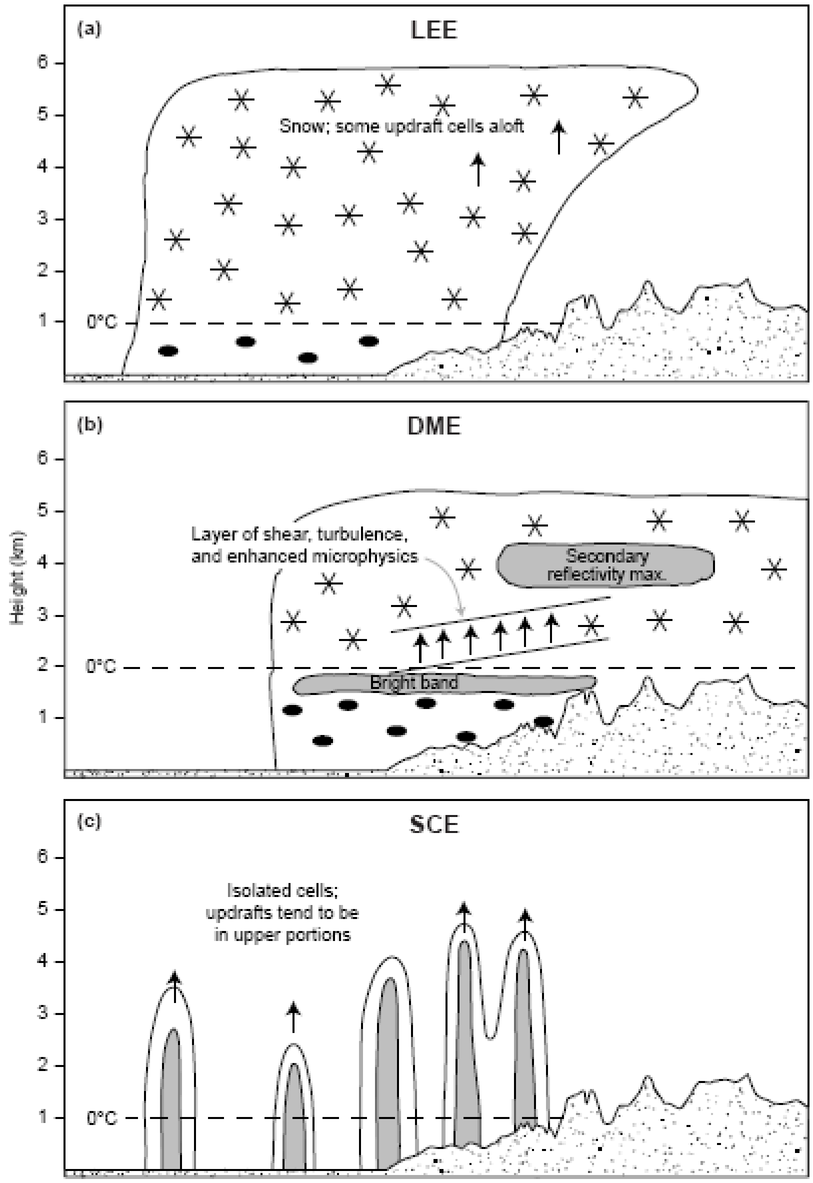

Fig. 7. Schematic illustration of the typical reflectivity structures observed in the (a) Leading Edge Echo, (b) Double Maximum Echo, and (c) Shallow Convective Echo periods of mid-latitude Pacific cyclones as they progress toward the terrain of the Oregon Cascade Range. The solid contours enclose areas of moderate reflectivity, while the shading indicates areas of increased reflectivity. The stars indicate snow and the ellipses rain. The speckled area shows the orography. The arrow represents updrafts (From Medina et al. 2007).

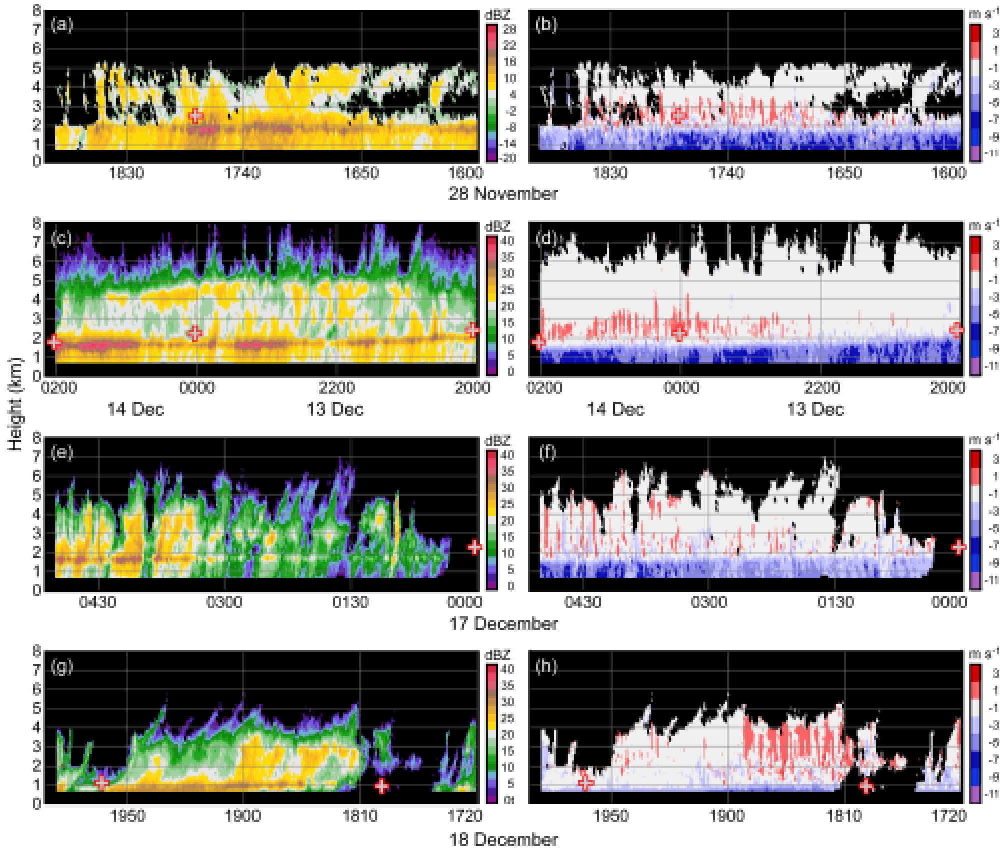

Fig. 8. Time series of S-band vertically pointing profiler radar (S-Prof) data during the passage of double maximum echo periods for reflectivity (left) and radial velocity (right): (a)-(b) 1600-1900 UTC 28 November 2001; (c)-(d) 2000 UTC 13 December – 0200 UTC 14 December 2001; (e)-(f) 0000-0500 UTC 17 December 2001; and (g)-(h) 1720-2000 UTC 18 December 2001. The crosses show the height of the 0° C level as measured by the Salem soundings. Note only storm in (c) shows distinct double maximum echo (From Medina et al. 2007).

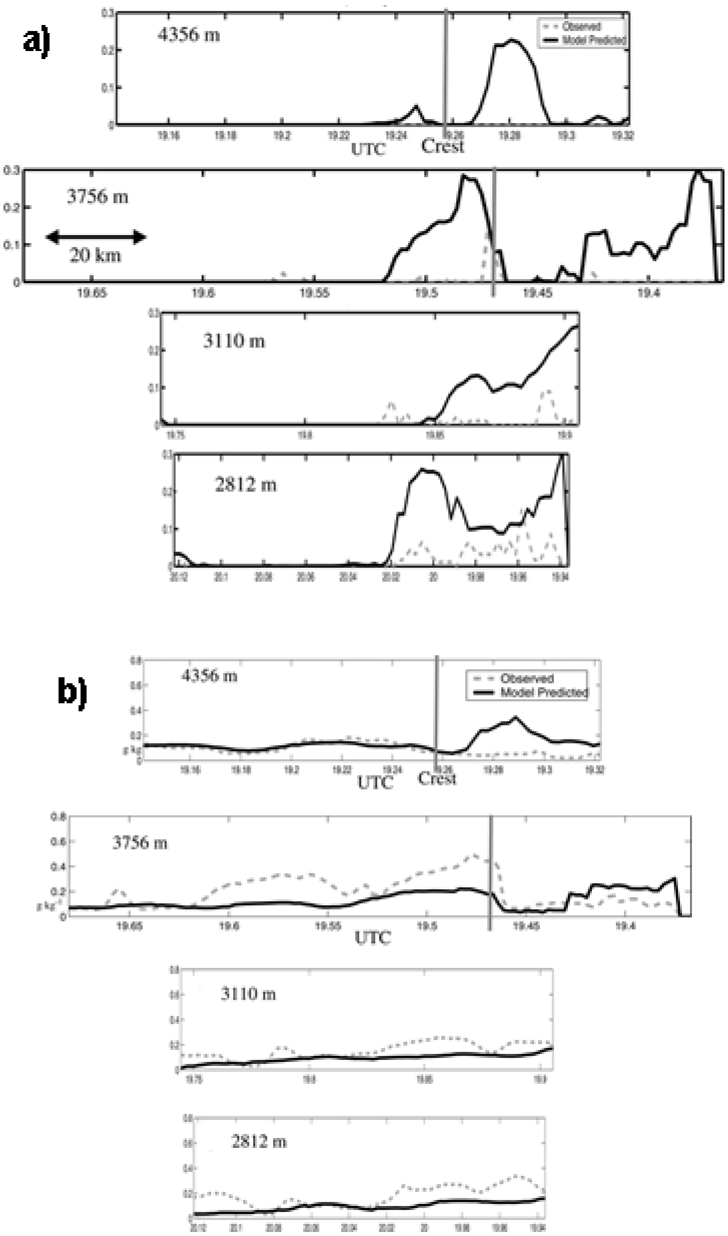

Fig. 9. Comparison of observed model variables for IPEX case. (a) Plots of liquid water mixing ratio (g kg-3) from the King Probe (dashed) and 1.33-km MM5 (solid) at 4356, 3756, 3110, and 2812 m MSL. (b) Plots of snow mixing ratio (g kg^{-1}) derived from the composite 2DGC–2DP particle size spectra (gray dashed) and 1.33-km MM5 (black) at 4356, 3756, 3110, and 2812 m MSL. The location of the crest is shown by the gray vertical line (From Colle et al. 2005a).

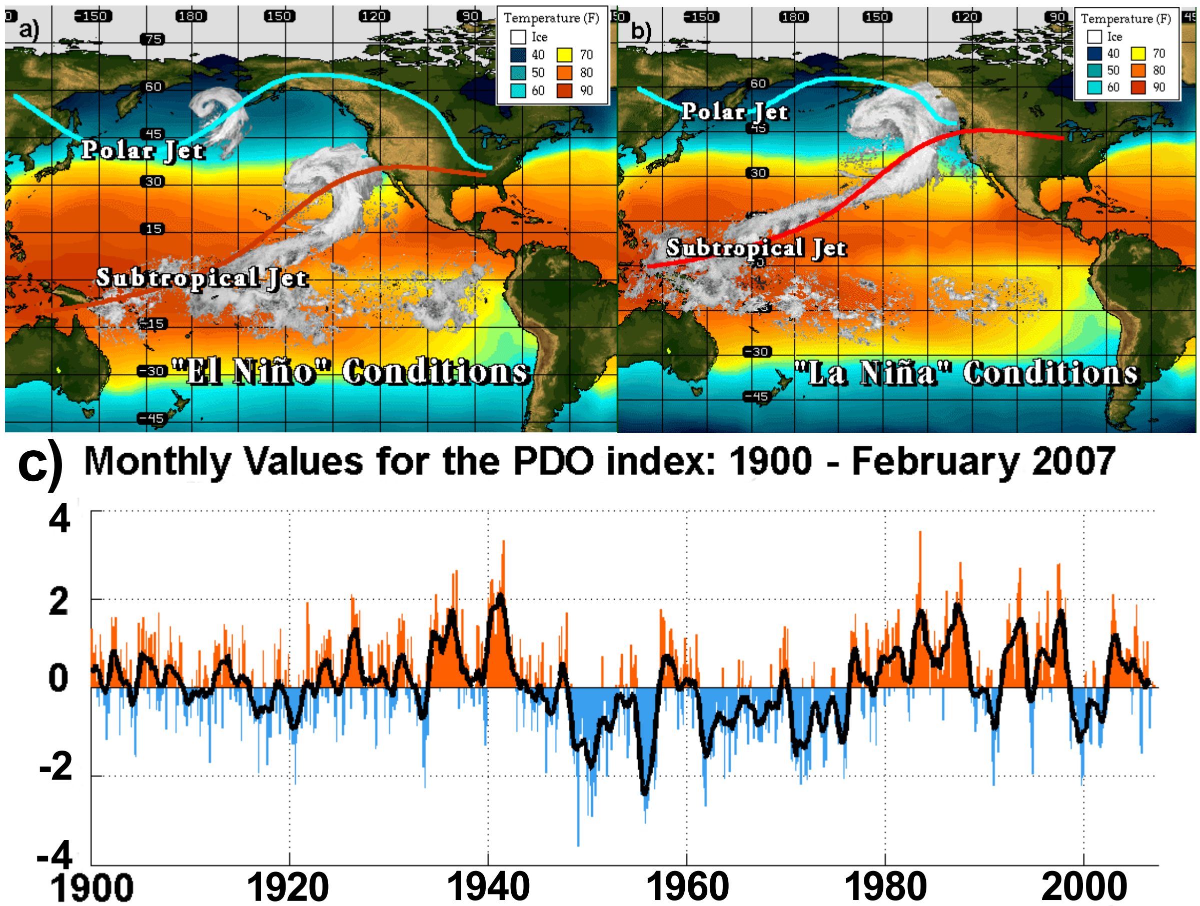

Fig. 10. Sea surface temperatures that show the typical atmospheric responses to shifts the ocean temperature during (a) El Nino and (b) La Nina (Taylor 1998). (c) Pacific Decadal Oscillation (PDO) monthly index from 1900 through Feb. 2007 (JISAO).

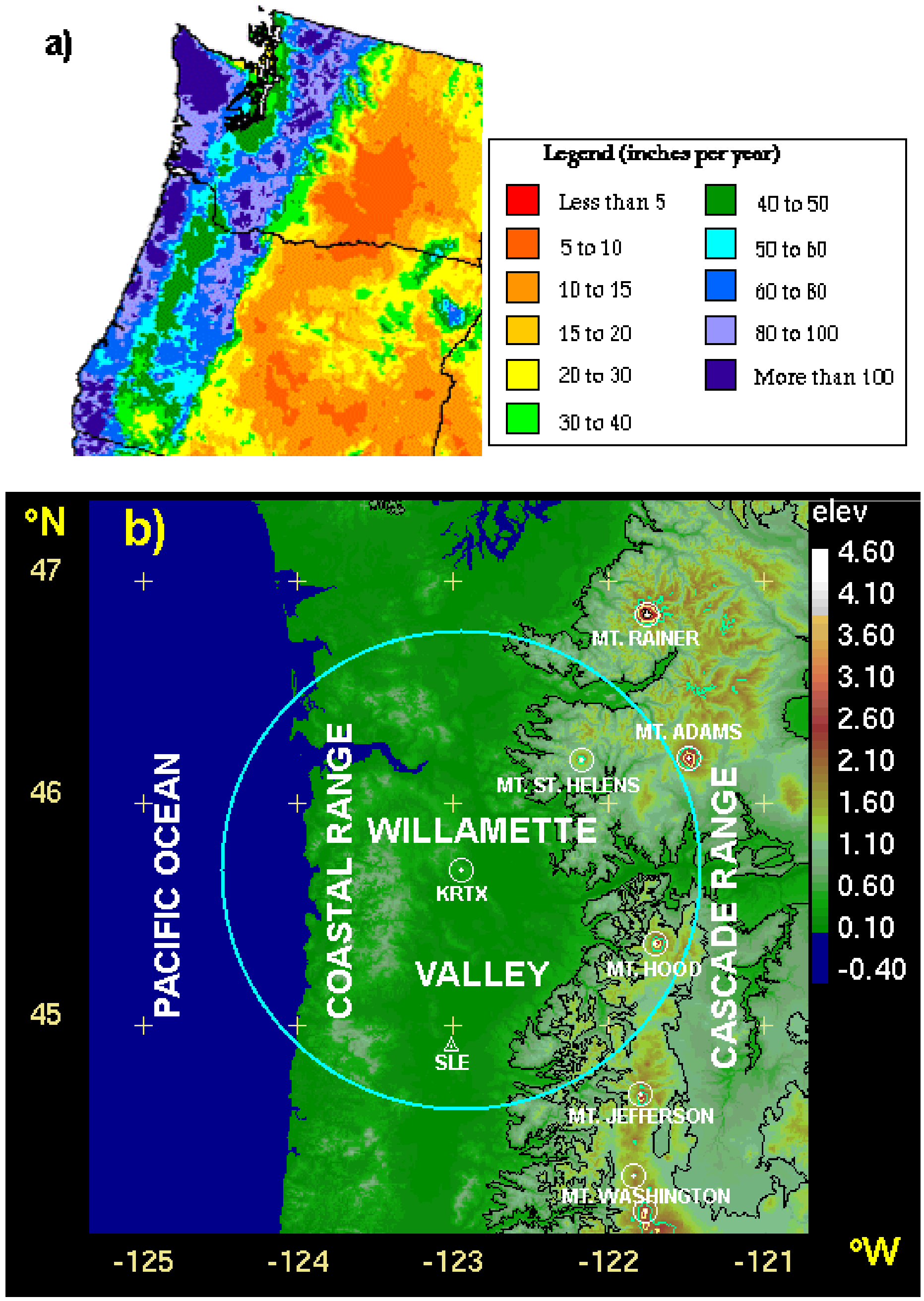

Fig. 11. (a) Average annual precipitation (in inches) for thirty-year (1961 – 1990) climatology of the U.S. Pacific Northwest. The diagram shows enhanced precipitation associated with Coastal (left side) and Cascade (right side) Ranges in the analysis area (From Daly et al. 1994). (b) Topography of Portland, Oregon and its surrounding areas (in km altitude). Locations of Coastal and Cascade Ranges, Portland NEXRAD radar (circle), Salem sounding (triangle), and Willamette Valley are labeled.

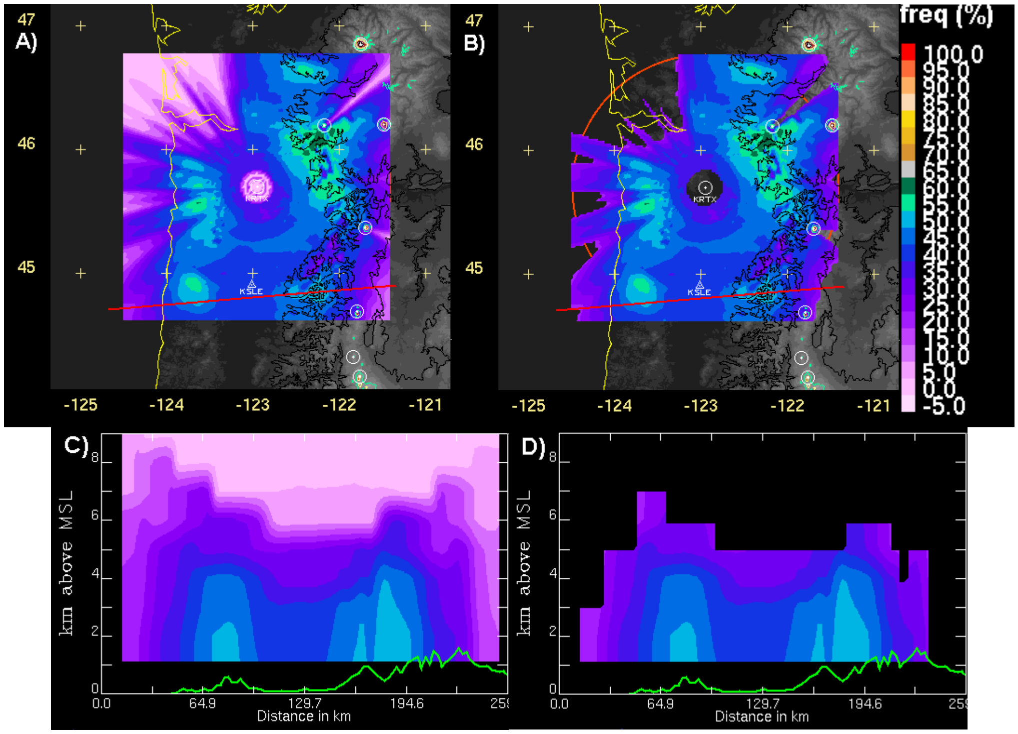

Fig. 12. Precipitation frequency (%) plots for S-SW storms for all three winter seasons. (a),(c) represent unmasked precipitation frequency for S-SW storms. (b),(d) represent masked precipitation frequency (≤ 20 %) for S-SW storms.

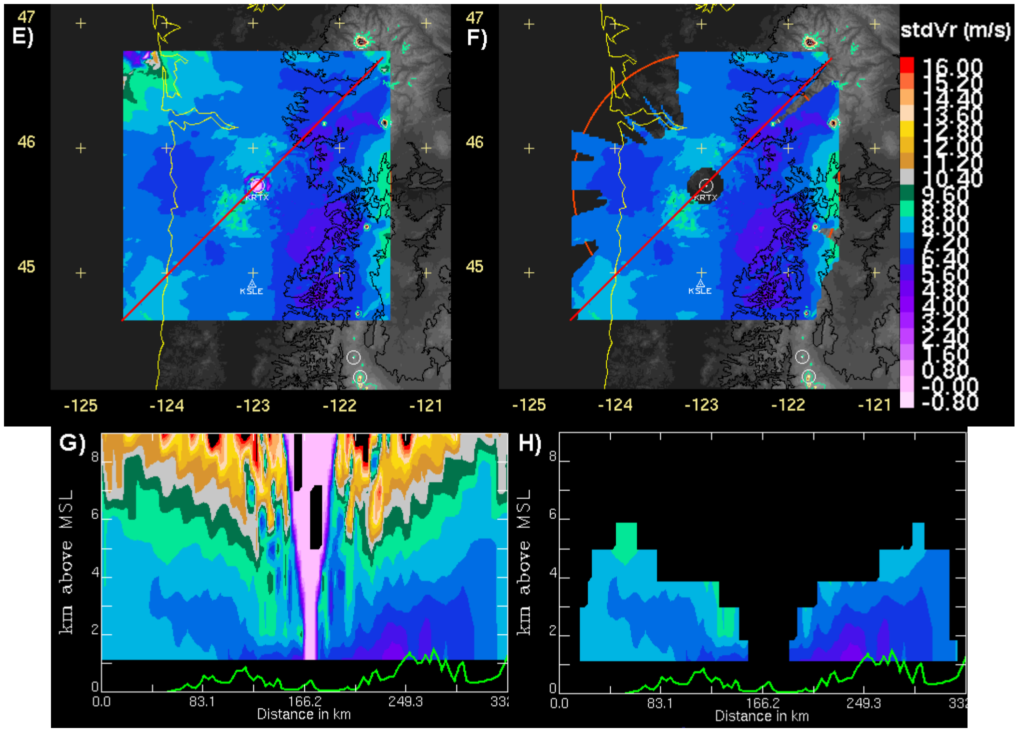

Fig. 12 cont. Standard deviation of radial velocity for S-SW storms for all three winter seasons. (e),(g) Unmasked standard deviation of radial velocity for S-SW storms. (f),(h) Masked standard deviation of radial velocity for S-SW storms.

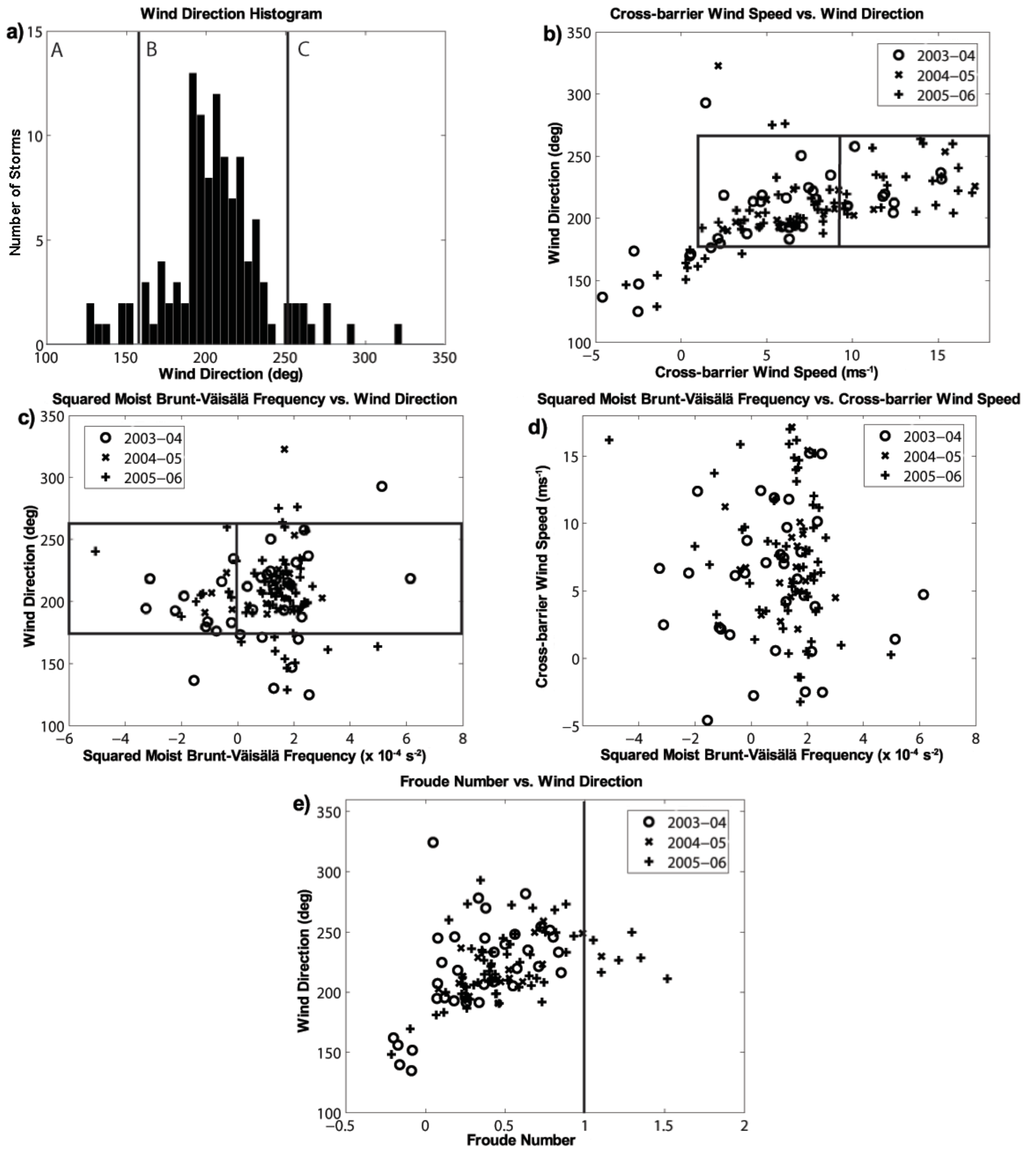

Fig. 13. (a) Histogram of vertically averaged wind direction storms for 117 storms over three winter seasons. Storms are separated by wind directions (black line); A – SE storms (9 total), B – S-SW storms (98), and C – W-NW storms (10) for averaged plots in Figs. 15 – 17. (b) Scatter plot of vertically averaged cross-barrier wind speed versus wind direction for layer (0.61 - 2.2 km altitude) from Salem (SLE) upper-air soundings. Box shows categories of weak wind speed (2 - 9 ms^{-1}) and stronger wind speed (9 - 18 ms^{-1}) storms for those with 180º - 260º azimuth layer-averaged wind direction for averaged plots in Figs. 18 – 19. (c) Scatter plot of vertically averaged moist squared Brunt-Väisälä frequency (s^{-1}) versus wind direction for layer (0.61 - 2.2 km altitude). Black line indicates separation of unstable (B-V < 0) and stable/neutral (B-V ≥ 0) storms used for averaged plots in Figs. 20 – 21. (d) Similar plot as (c) except B-V versus cross-barrier wind speed (ms^{-1}). (e) Scatter plot of Froude number versus wind speed (ms^{-1}) using the 800 – 900 hPa layer average.

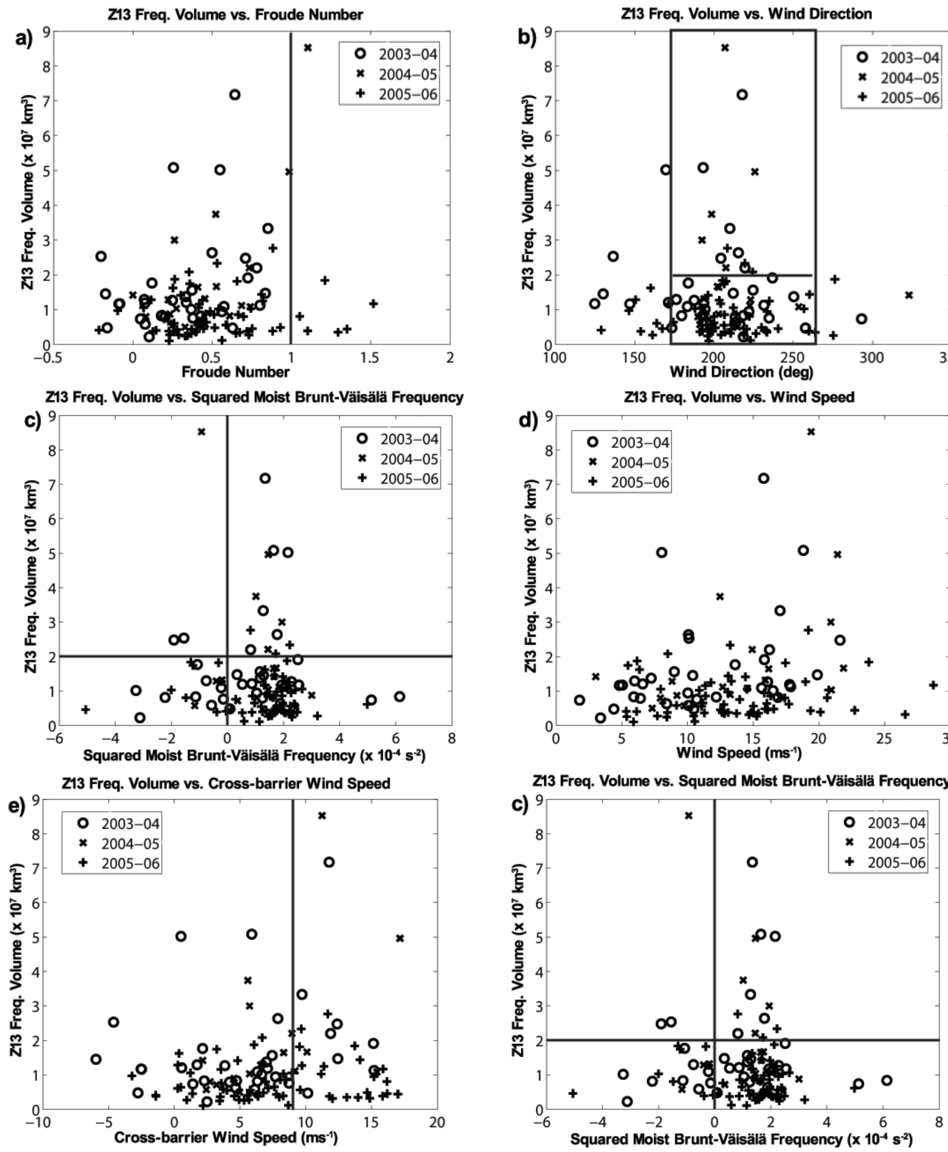

Fig. 14. (a) Scatter plot of storm total precipitation volume (Z ≥ 13 dBZ) versus Froude number for 800 – 900 hPa layer for all 117 storms. (b) Same as (a), except for vertically averaged wind direction using 0.61 – 2.2 km layer average. Black line represents threshold of 2 x 10^7 km^3 as separation between large and small storms for Figs. 22 and 23. (c) Same as (b), except for Brunt-Väisälä frequency (s^{-1}). Black lines indicate threshold of 2 x 10^7 km^3 for storm total accumulated volumes and 0 s^{-2} for stability. (d) Same as (b), except for vertically averaged total wind speed. (e) Same as (b), except for vertically averaged cross-barrier wind speed (ms^{-1}). Black line indicates separation at 9 ms^{-1} for weak (U < 9ms^{-1}) and strong (U ≥ 9ms^{-1}) cross-barrier wind speed storms. (f) Histogram of storm total accumulated volumes of precipitation frequency (Z ≥ 13 dBZ).

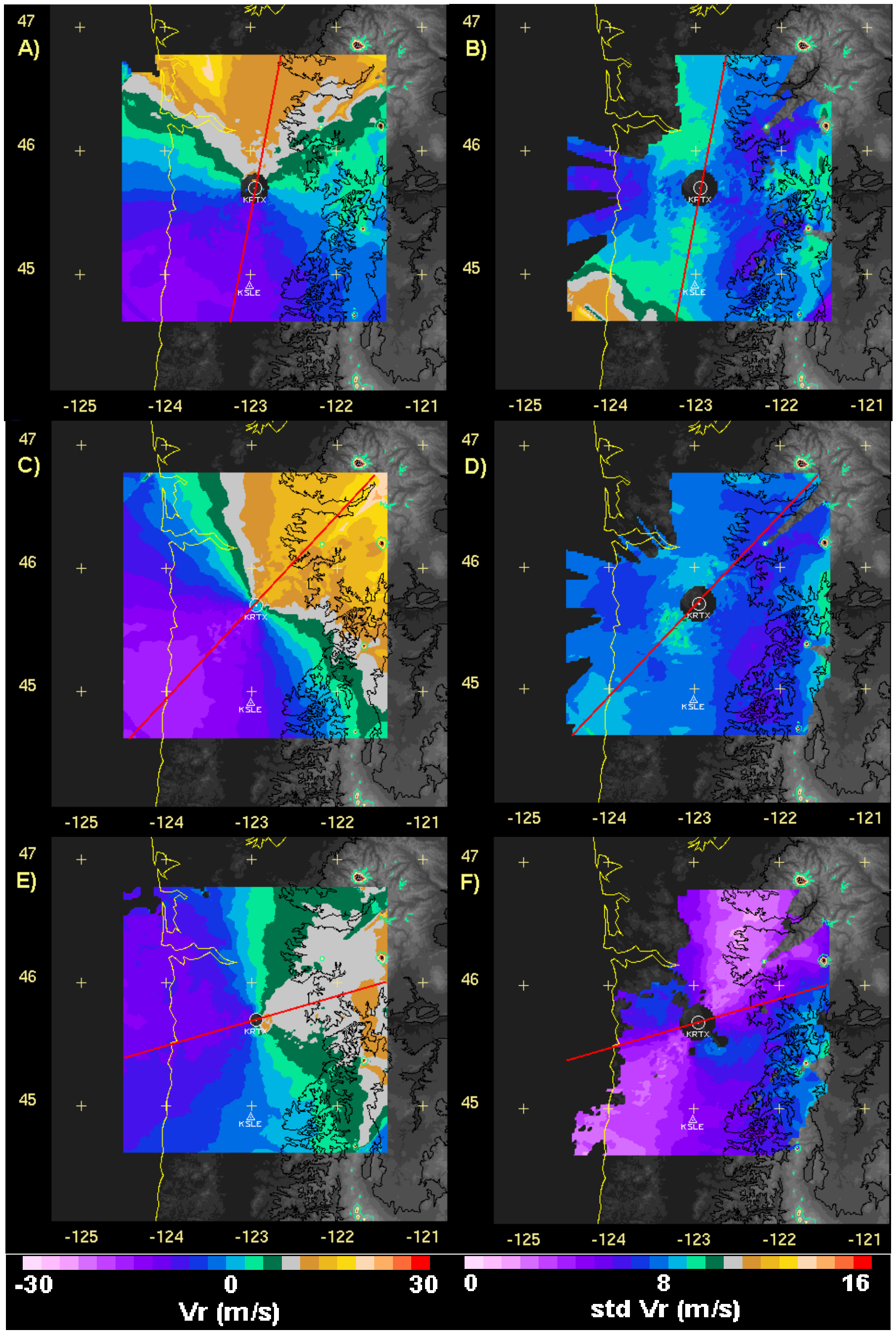

Fig. 15. Comparison of radial velocity structures (at 2 km altitude) for storms with different low-level wind directions (from Figure 13a). All V_r standard deviation figures show only values correspond to points with precipitation frequency > 20 %. (a) Horizontal mean radial velocity pattern for SE storms. (b) Horizontal standard deviation of mean radial velocity for (a). (c) Same as (a) except for S-SW storms. (d) Horizontal standard deviation of mean radial velocity for (c). (e) Same as (a) and (b) except for W-NW storms. (f) Horizontal standard deviation of mean radial velocity for (e).

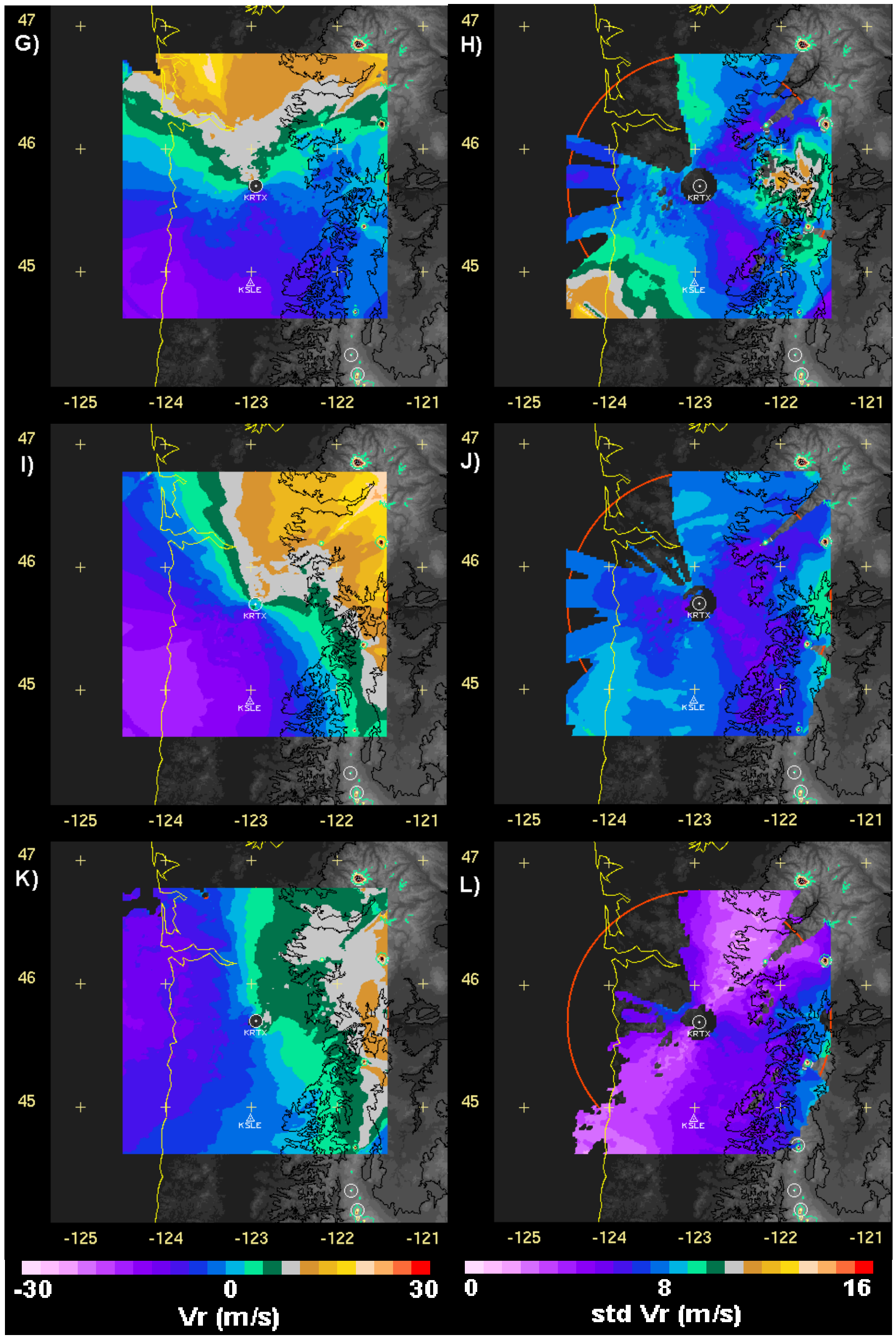

Fig. 15 cont. Comparison of horizontal radial velocity structures (at 1 km altitude) for storms with different low-level wind directions as defined in Figure 13a. Standard deviation of V_r plots show only values corresponding to precipitation frequency > 20 %. (g) Horizontal mean radial velocity pattern for SE storms. (h) Horizontal standard deviation of mean radial velocity for (g). (i) Same as (g) except for S-SW storms. (j) Horizontal standard deviation of mean radial velocity for (i). (k) Same as (g) and (i) except for W-NW storms. (l) Horizontal standard deviation of mean radial velocity for (k).

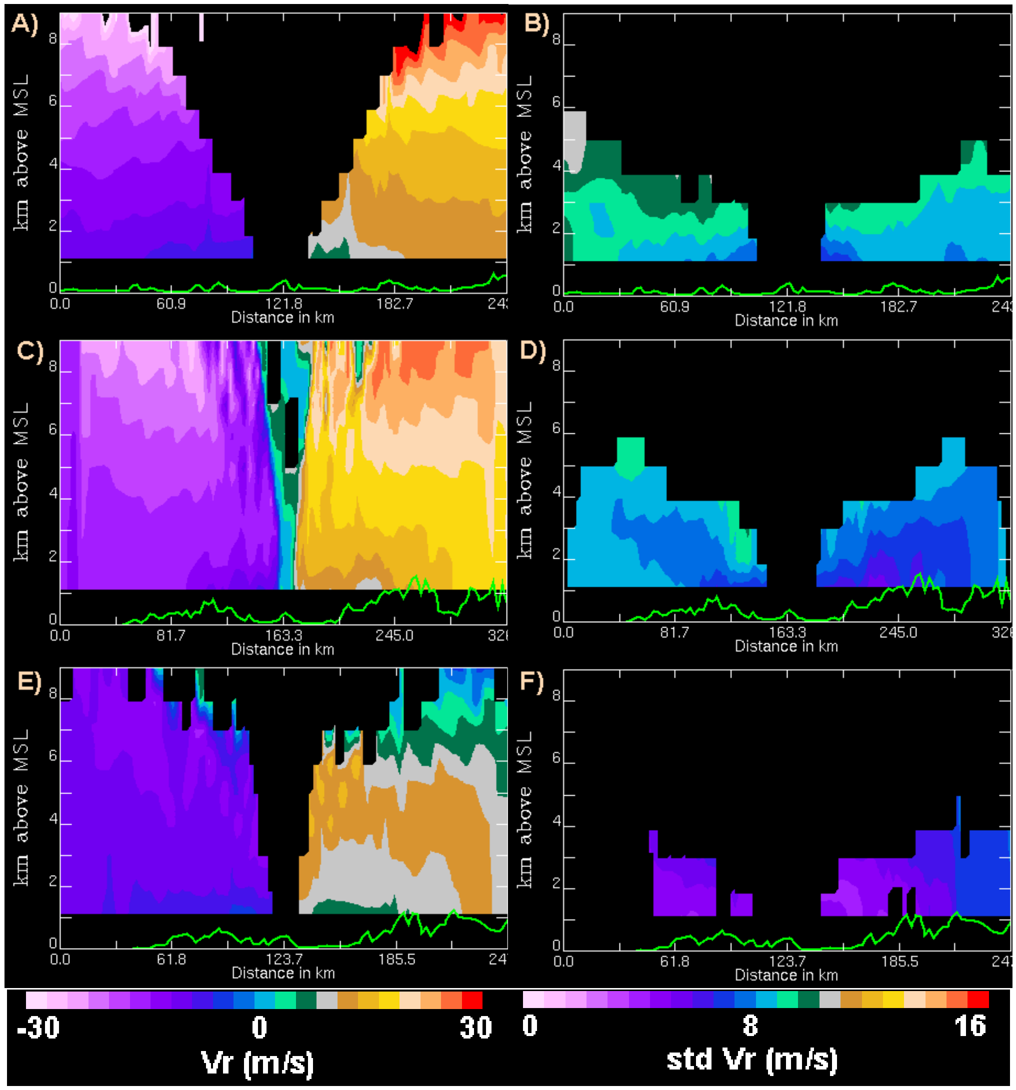

Fig. 16. Same as Figure 15, except using vertical radial velocity cross sections for different low-level wind directions (along red lines in Figure 4). Standard deviation of V_r plots show only values corresponding to precipitation frequency > 20 %. A) and B) - SE storms; C) and D) - S-SW storms; E) and F) - W-NW storms.

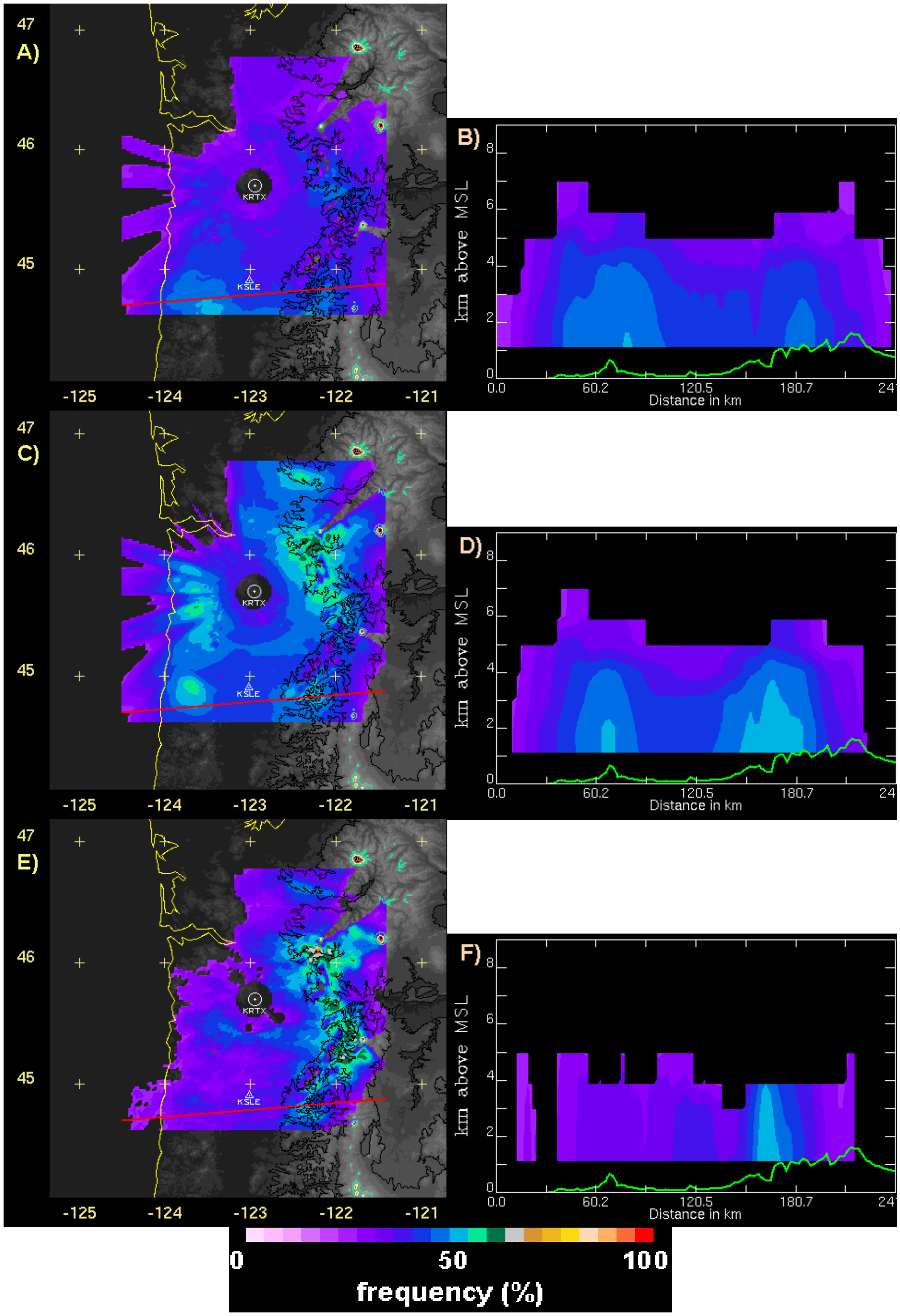

Fig. 17. Comparison of precipitation frequency at 2 km altitude for storms with different low-level wind directions. All precipitation frequency figures show values greater than 20 %. A) and B) - SE storms; C) and D) - S-SW storms; E) and F) - W-NW storms.

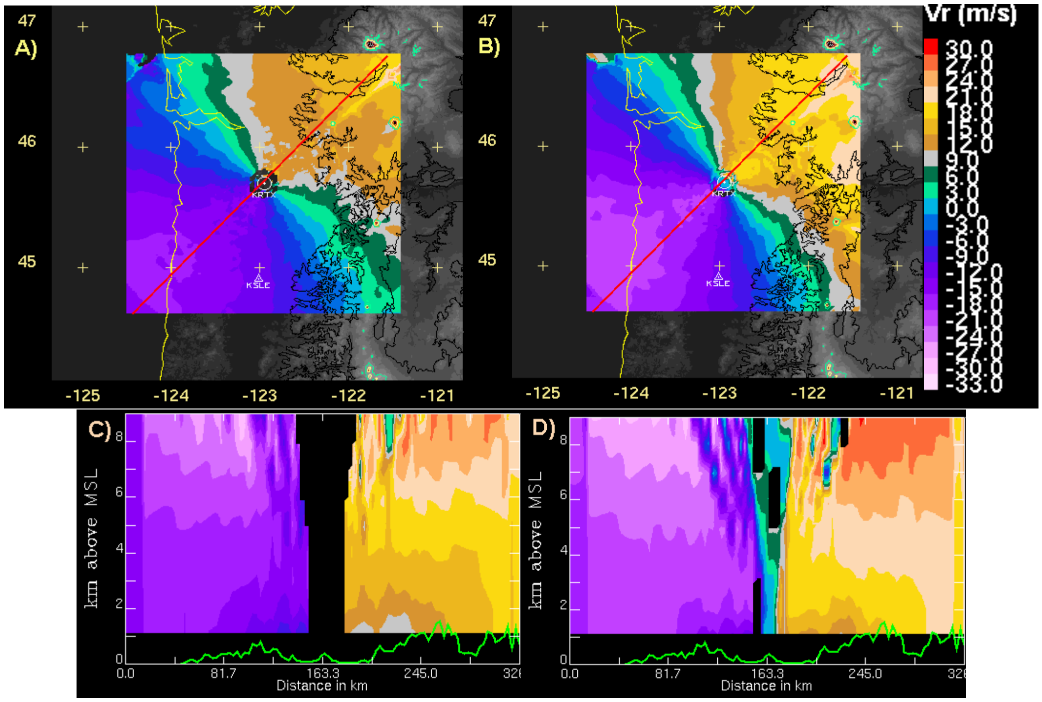

Fig. 18. Comparison of radial velocity structures for storms of weaker (2 – 9 ms^{-1}) and stronger (9 -18 ms^{-1}) cross-barrier winds as defined in Figure 13b. All standard deviation plots use the precipitation frequency threshold of 20 %. (a) Horizontal mean radial velocity (ms^{-1}) pattern for weaker cross-barrier wind storms at 2 km altitude. (b) Same as (a), except for stronger cross-barrier wind storms. (c) Vertical cross section of mean radial velocity along red line in (a) for weaker velocity storms. (d) Vertical cross section of mean radial velocity along red line in (b) for stronger velocity storms.

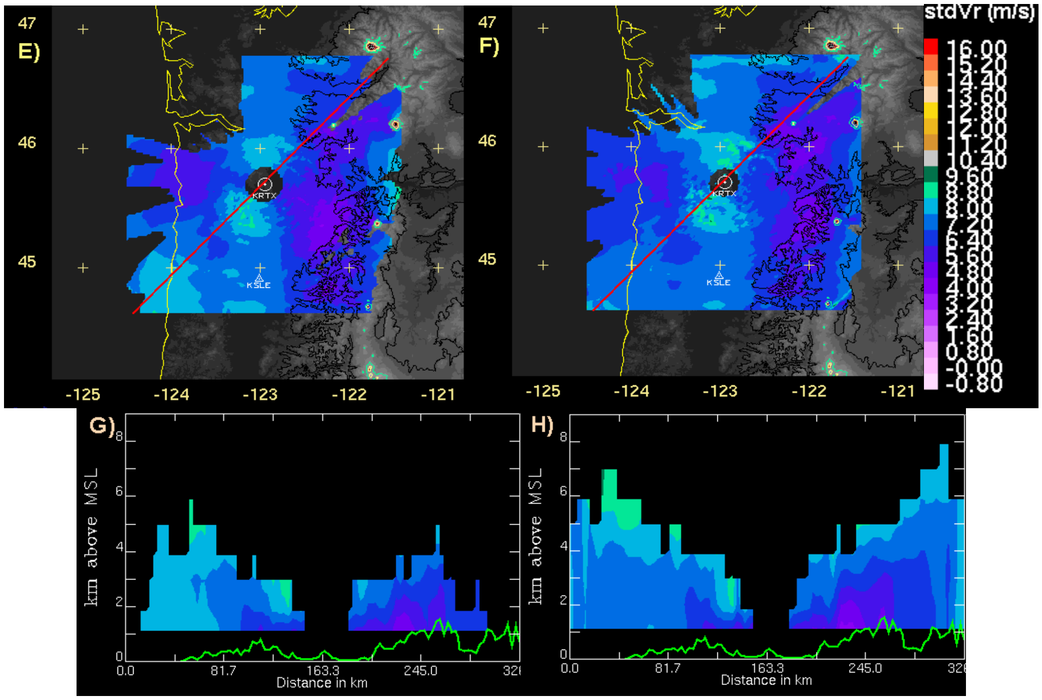

Fig. 18 cont. (e) Standard deviation of mean radial velocity for weaker velocity storms. (f) Standard deviation of mean radial velocity for weaker velocity storms. (g) Vertical cross section of (e). (h) Vertical cross section of (f).

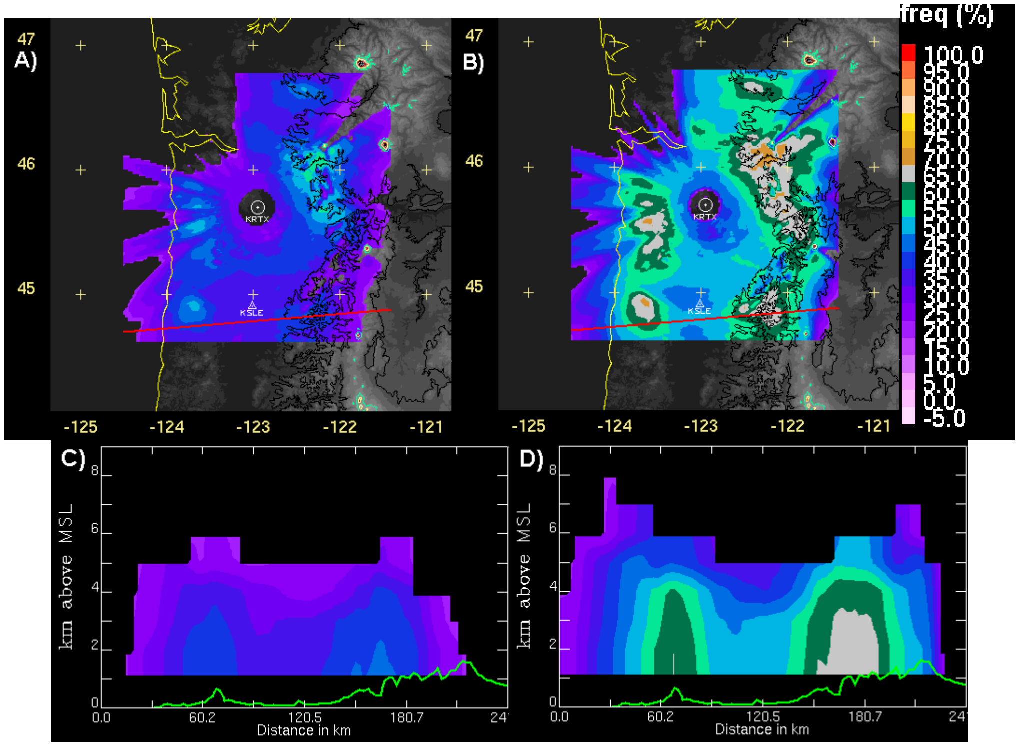

Fig. 19. Same as Figure 17, except for precipitation frequency for lower and higher cross-barrier wind speeds. All precipitation frequency figures show only values greater than 20 %. A) and C) – Weak cross-barrier wind speed storms; B) and D) – Strong cross-barrier wind speed storms.

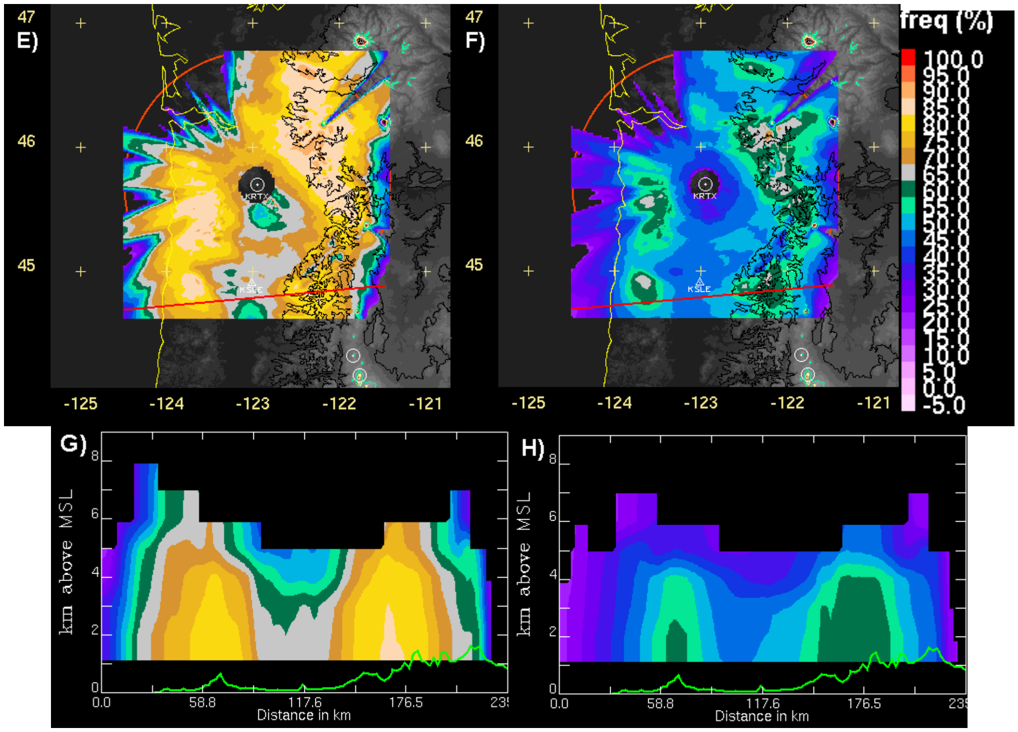

Fig. 19 cont. E) and G) – Two largest accumulated volume storms; G) and H) Strong cross-barrier wind speed storms without the two largest accumulated volume storms.

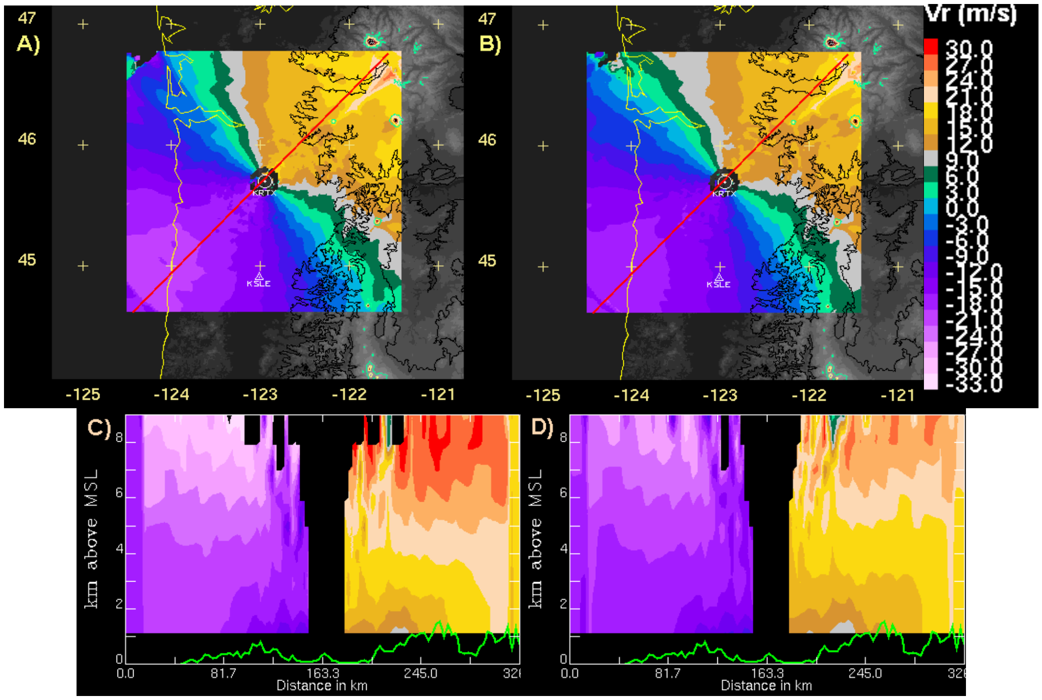

Fig. 20. Comparison of radial velocity structures for storms with unstable (B-V < 0 s^{-1}) and stable (0.15×10^{-4} s^{-1} < B-V < 4×10^{-4} s^{-1}) storms as defined in Figure 13c. All standard deviation plots use the precipitation frequency threshold > 20 %. (a) Horizontal mean radial velocity (ms^{-1}) pattern for unstable storms at 2 km altitude. (b) Same as (a), except for stable storms. (c) Vertical cross section of mean radial velocity along red line in (a) for unstable storms. (d) Vertical cross section of mean radial velocity along red line in (b) for stable storms.

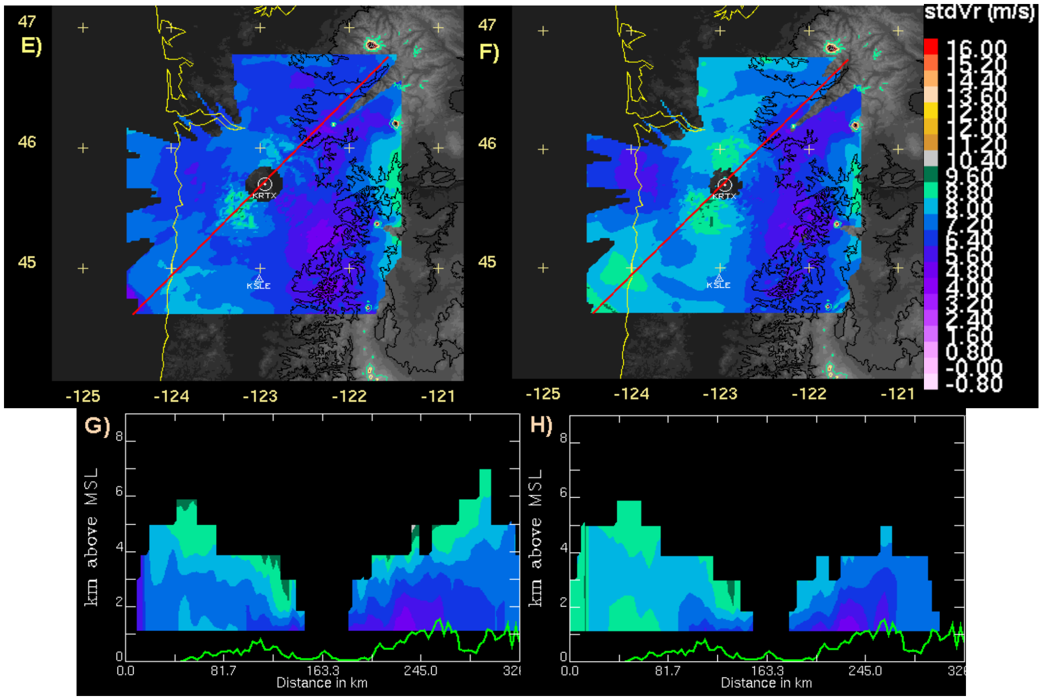

Fig. 20 cont. (e) Standard deviation of mean radial velocity for unstable storms. (f) Standard deviation of mean radial velocity for stable storms. (g) Vertical cross section of (e). (h) Vertical cross section of (f).

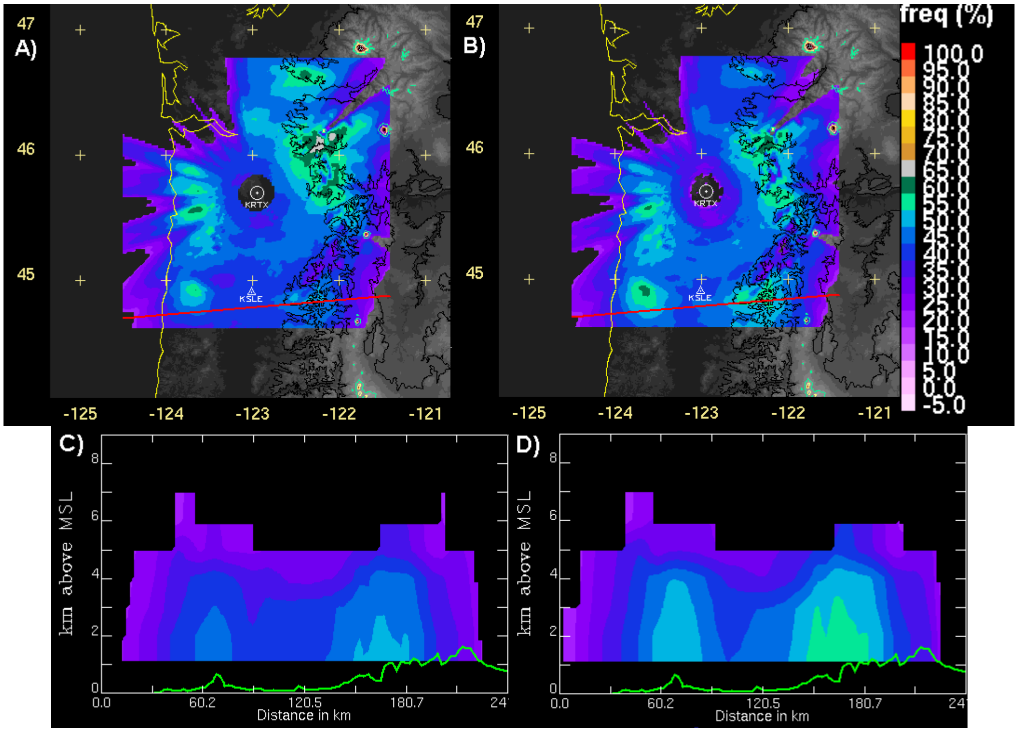

Fig. 21. Same as Figure 19, except for precipitation frequency for unstable and stable storms. All precipitation frequency figures show only values greater than 20 %. A) and C) – unstable storms; B) and D) – stable storms.

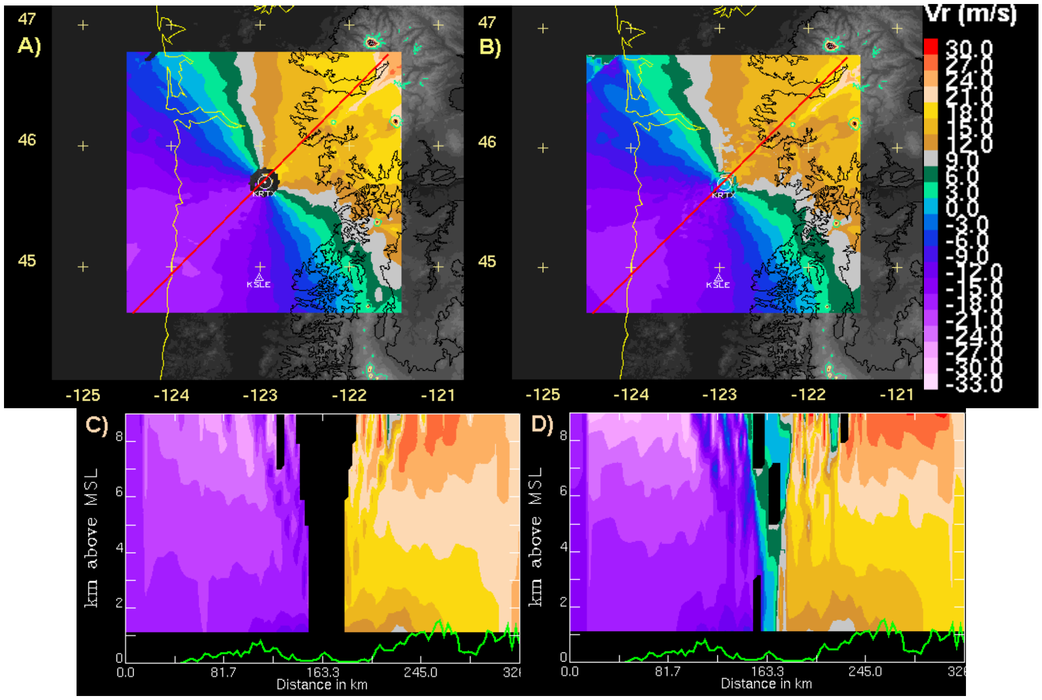

Fig. 22. Comparison of radial velocity structures for storms for large (volume > 2 x 10^7 km^3) and small (volume < 2 x 10^7 km^3) volume storms as defined in Figure 14a. All standard deviation plots use the precipitation frequency threshold > 20 % (a) Horizontal mean radial velocity (ms^{-1}) pattern for large storms at 2 km level. (b) Same as (a), except for small storms. (c) Vertical cross section of mean radial velocity along red line in (a) for large storms. (d) Vertical cross section of mean radial velocity along red line in (b) for small storms.

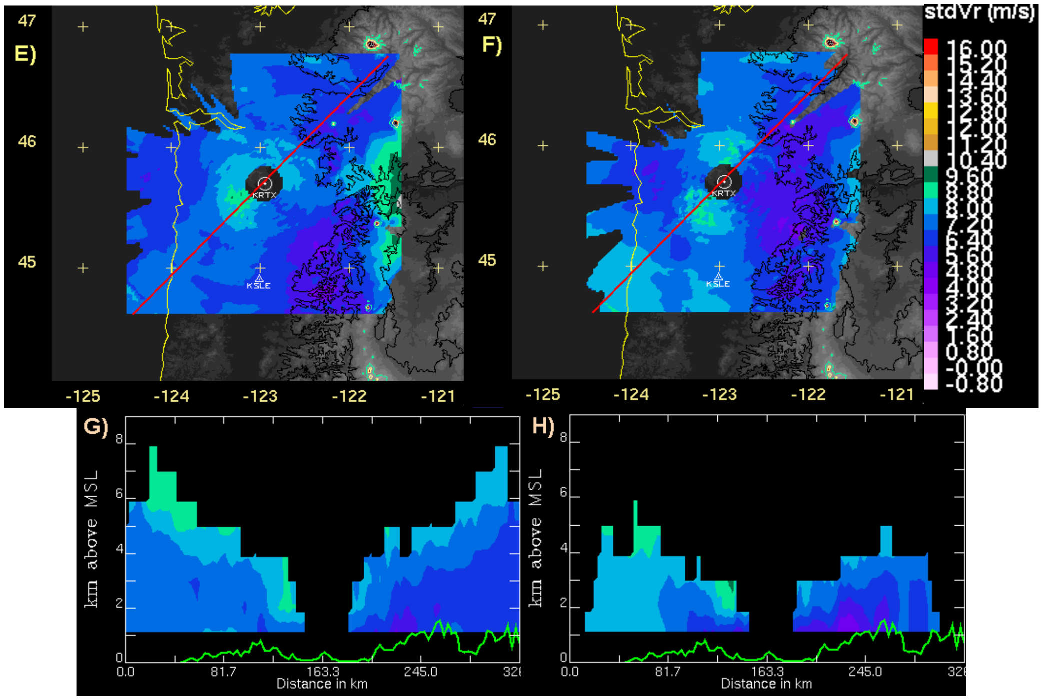

Fig. 22 cont. (e) Standard deviation of mean radial velocity for large storms. (f) Standard deviation of mean radial velocity for small storms. (g) Vertical cross section of (e). (h) Vertical cross section of (f).

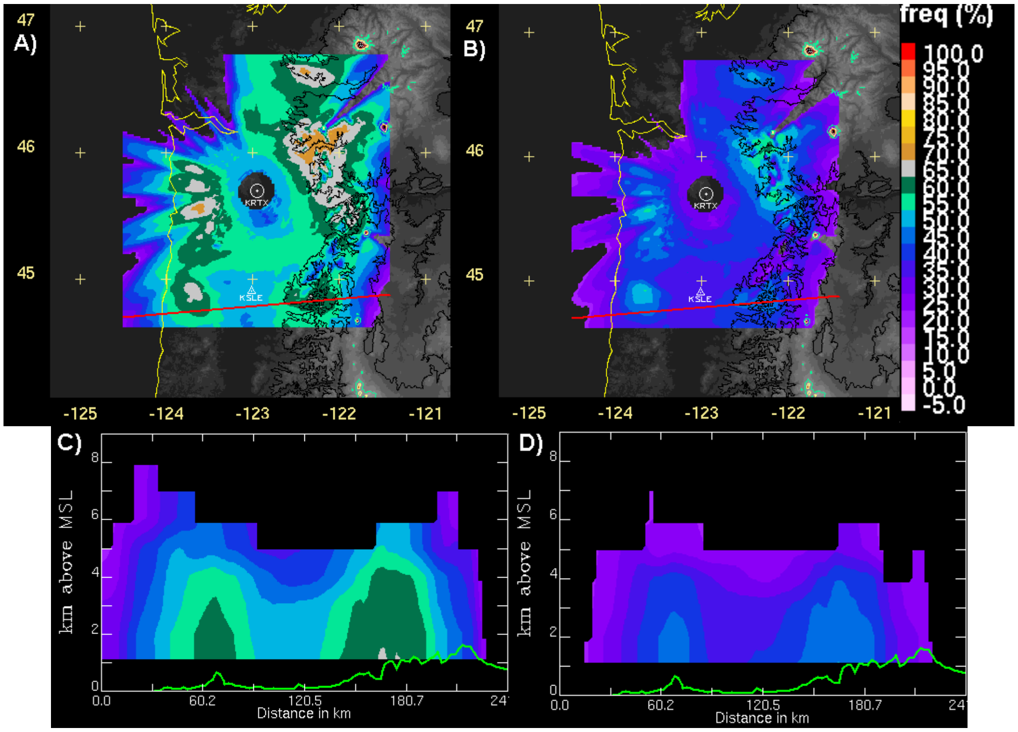

Fig. 23. Same as Figure 21, except for precipitation frequency for large and small volume storms. All precipitation frequency figures show only values greater than 20 %. A) and C) – large volume storms; B) and D) – small volume storms.

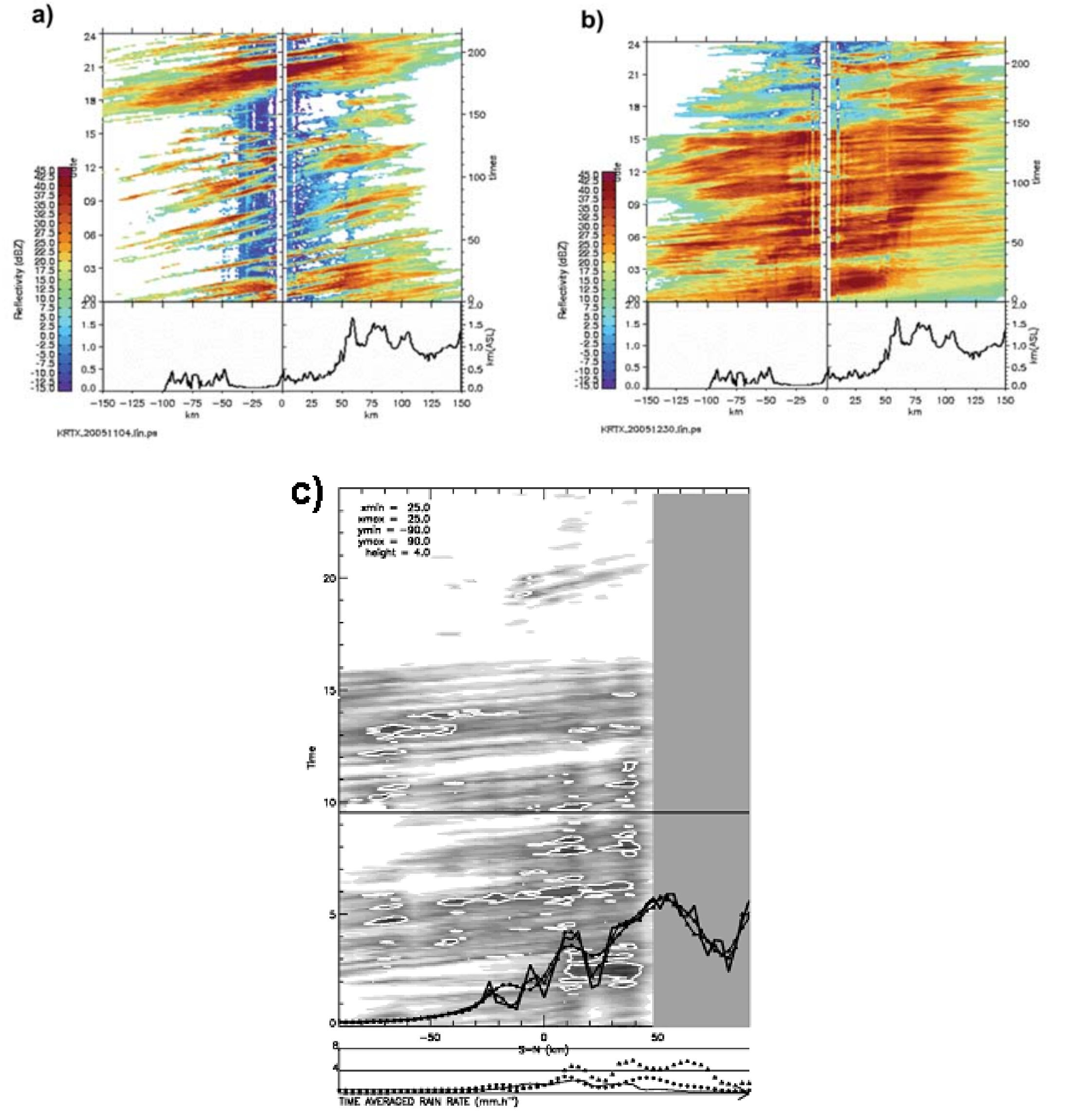

Fig. 24. Time versus distance plots along E-W line at 45.35° N latitude for (a) 2005 Nov 4 (small volume storm) and (b) 2005 Dec 30 (large volume storm) (Yanluan Lin, personal communication). (c) Time (UTC) versus distance diagram of Monte Lema radar reflectivity along 9.15°E at 4 km altitude for 20 September 1999. Measurements are every 7.5 minutes. Orographic precipitation locked to the terrain (From Smith et al. 2003).

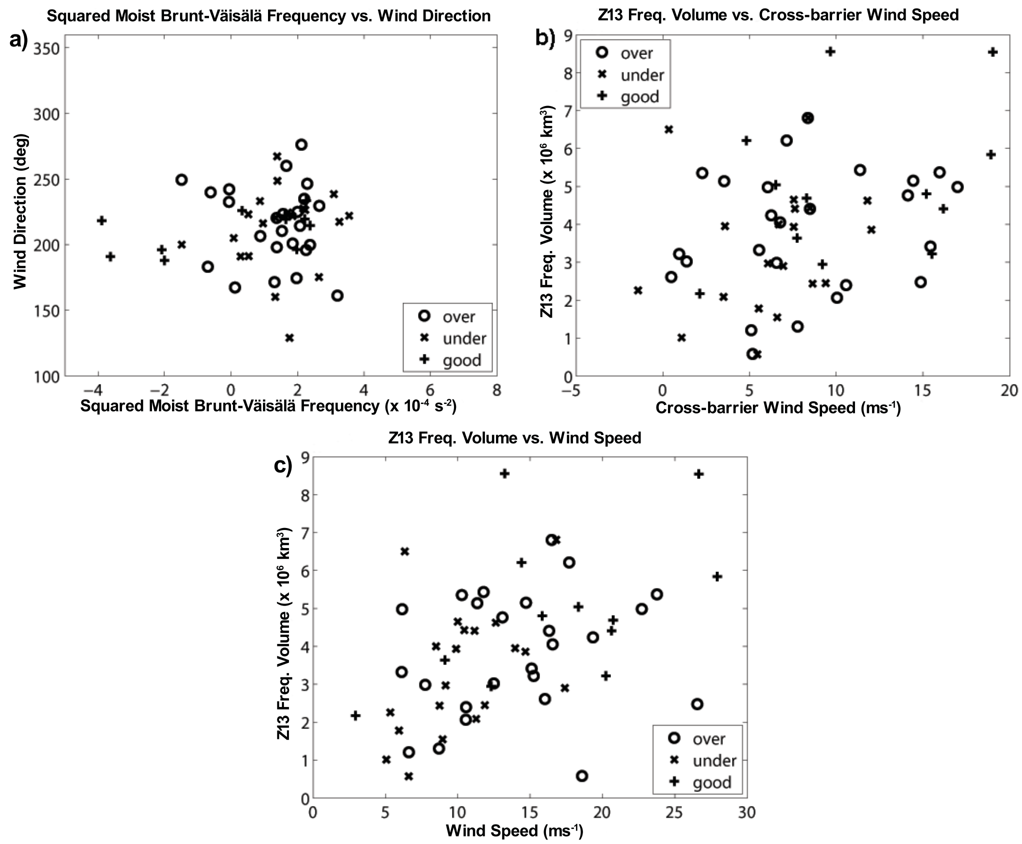

Fig. 25. (a) Moist Squared Brunt-Väisälä Frequency (s^{-2}) versus layer-averaged wind direction for all SNOTEL storms (57) during the 2005-2006 winter season. (b) Scatter plot of storm total precipitation volume ($Z \geq 13$ dBZ) versus vertically averaged cross-barrier wind speed (ms^{-1}). (c) Scatter plot of storm total precipitation volume ($Z \geq 13$ dBZ) versus vertically averaged wind speed (ms^{-1}). Analysis of good, under, and over prediction cases by Yanluan Lin of Stony Brook University based on SNOTEL snow gauge stations in the Western U.S.

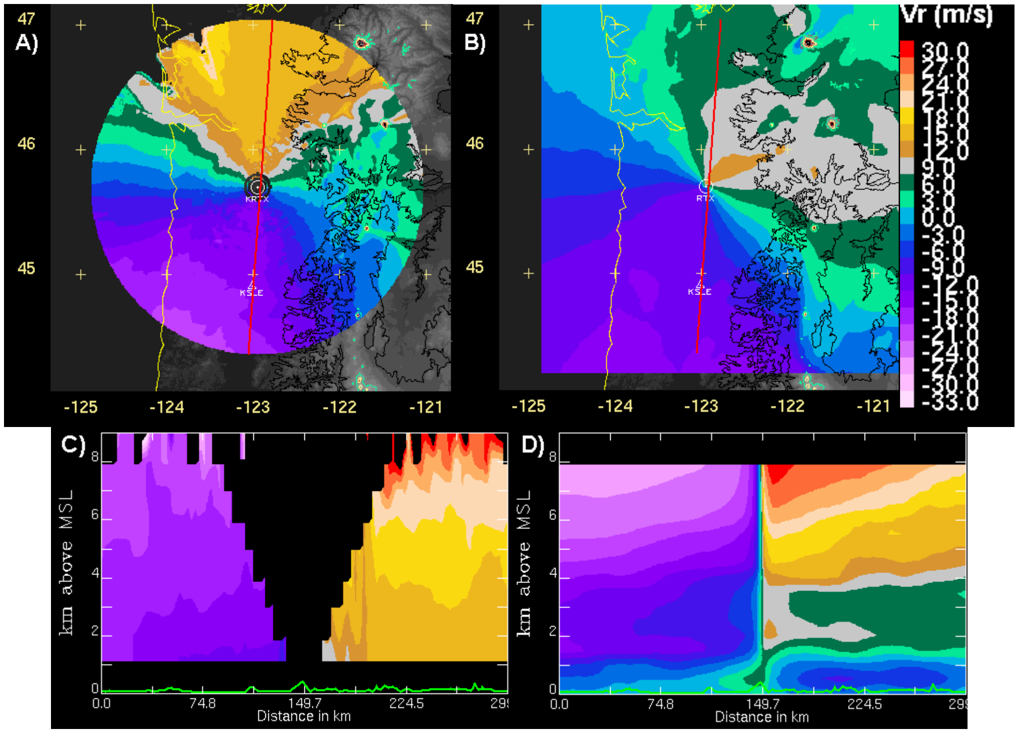

Fig. 26. Comparison of radial velocity structures (ms^{-1}) for southeasterly (SE) storms for the 2005-2006 winter storm season. Observed standard deviation plots use the precipitation frequency threshold > 20 %. (a) Horizontal mean radial velocity pattern for observed SE storms. (b) Same as (a) except for model SE storms. (c) Vertical cross section along red line in (a). (d) Vertical cross section along red line in (b).

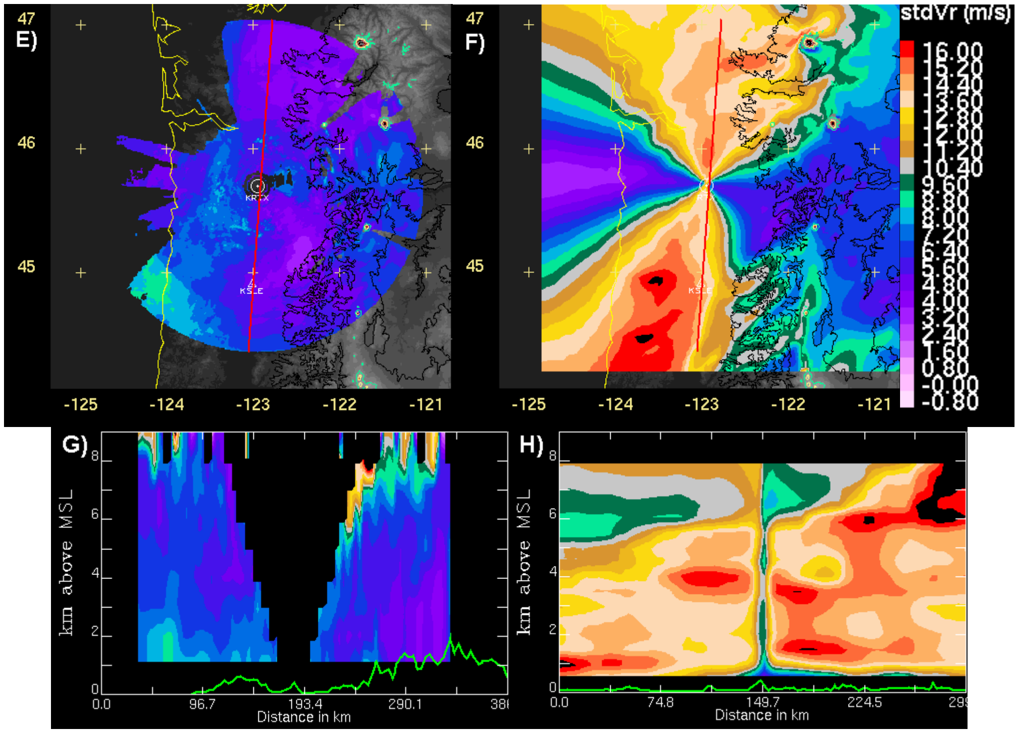

Fig. 26 cont. (e) Standard deviation values of (a). (f) Standard deviation values of (b). (g) Vertical cross section along red line in (e). (h) Vertical cross section along red line in (f).

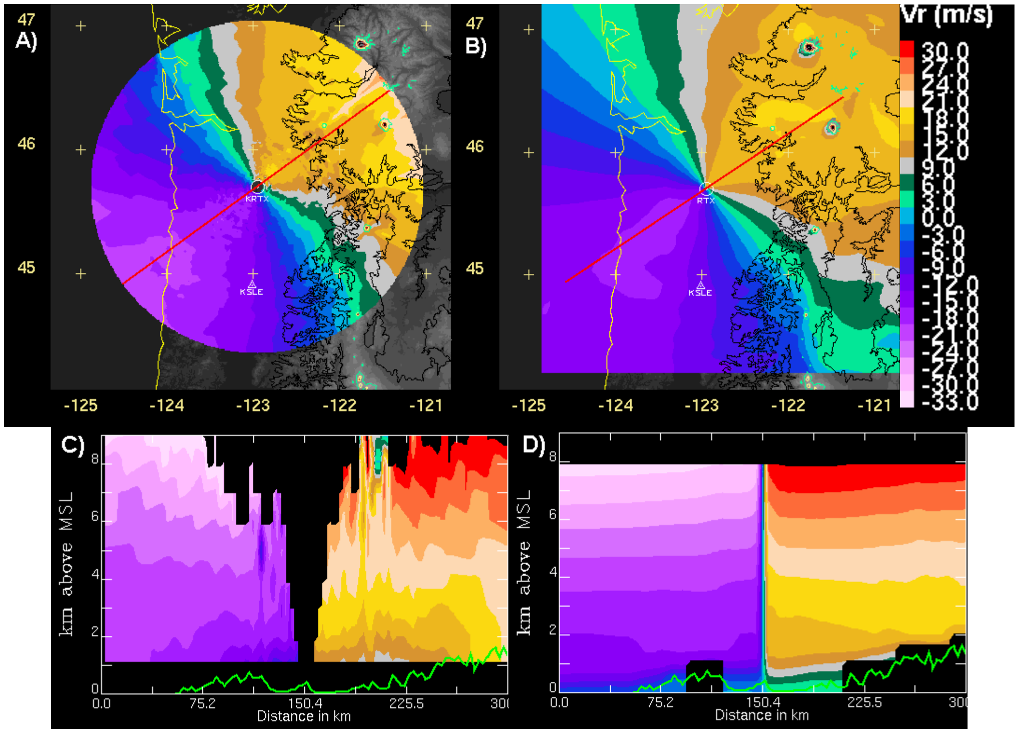

Fig. 27. Comparison of radial velocity structures (ms^{-1}) for south/southwest (S-SW) storms for the 2005-2006 winter storm season. Observed standard deviation plots use the precipitation frequency threshold > 20 %. (a) Horizontal mean radial velocity pattern for observed S-SW storms. (b) Same as (a) except for model S-SW storms. (c) Vertical cross section along red line in (a). (d) Vertical cross section along red line in (b).

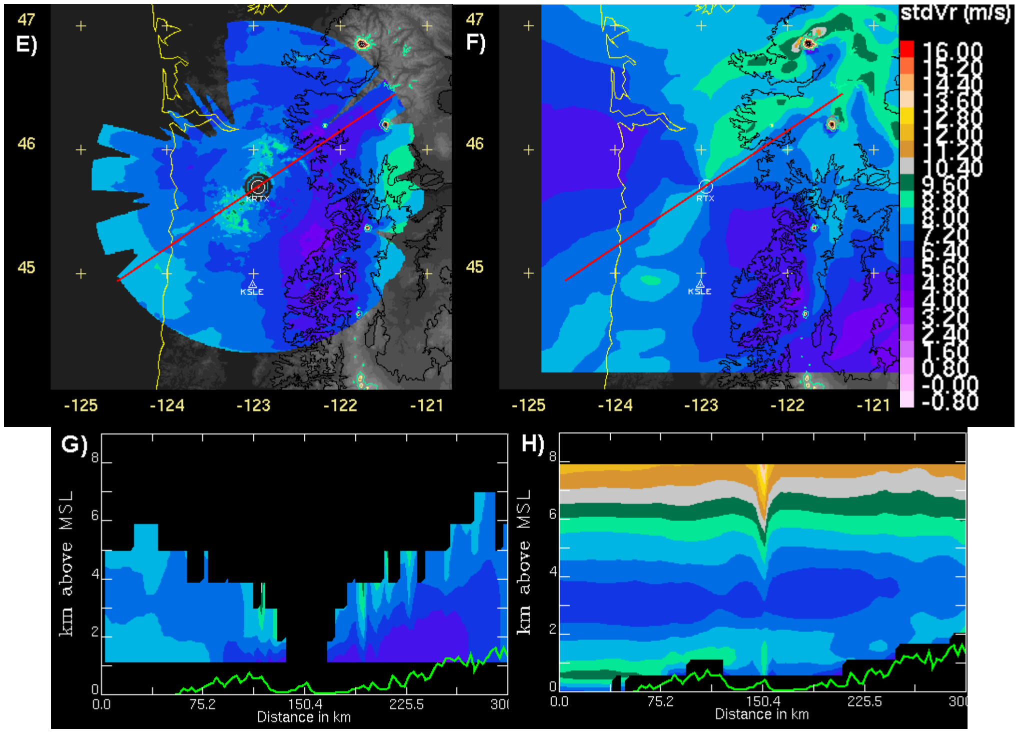

Fig. 27 cont. (e) Standard deviation values of (a). (f) Standard deviation values of (b). (g) Vertical cross section along red line in (e). (h) Vertical cross section along red line in (f).

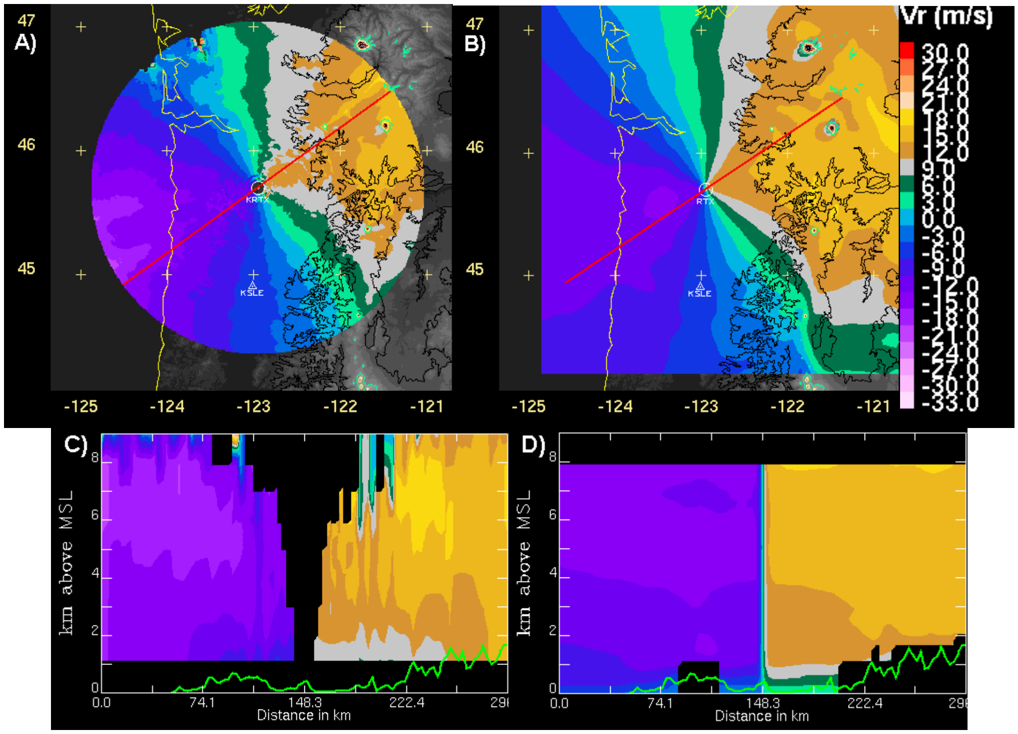

Fig. 28. Comparison of radial velocity structures (ms^{-1}) for west/northwest (W-NW) storms for the 2005-2006 winter storm season. Observed standard deviation plots use the precipitation frequency threshold > 20 %. (a) Horizontal mean radial velocity pattern for observed W-NW storms. (b) Same as (a) except for model W-NW storms. (c) Vertical cross section along red line in (a). (d) Vertical cross section along red line in (b).

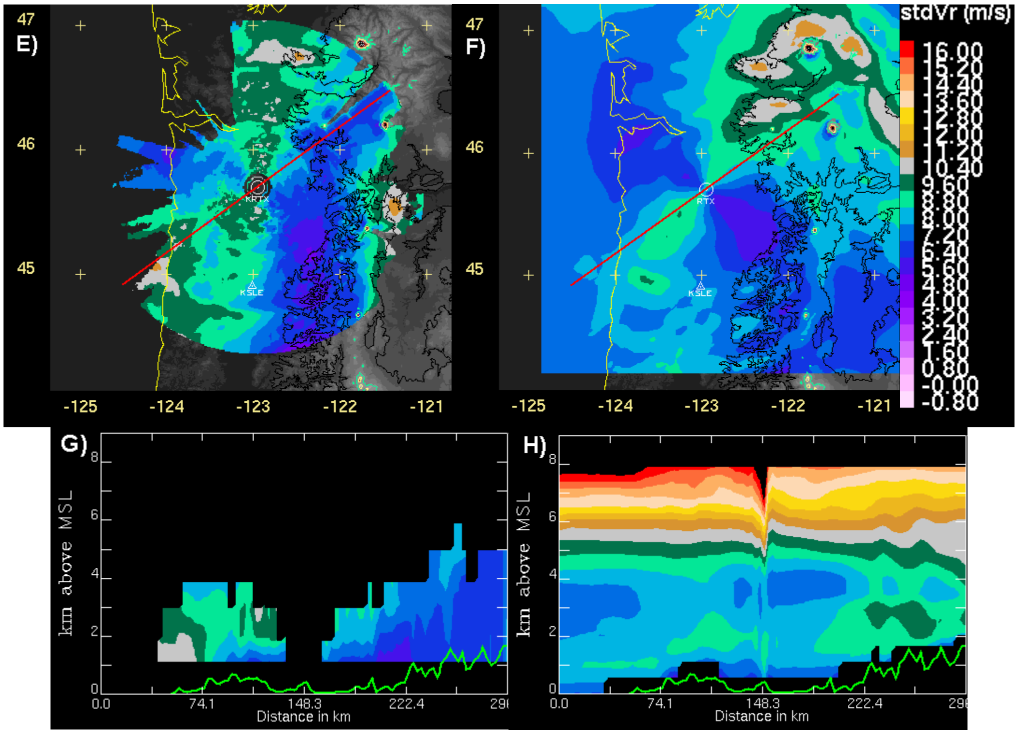

Fig. 28 cont. (e) Standard deviation values of (a). (f) Standard deviation values of (b). (g) Vertical cross section along red line in (e). (h) Vertical cross section along red line in (f).

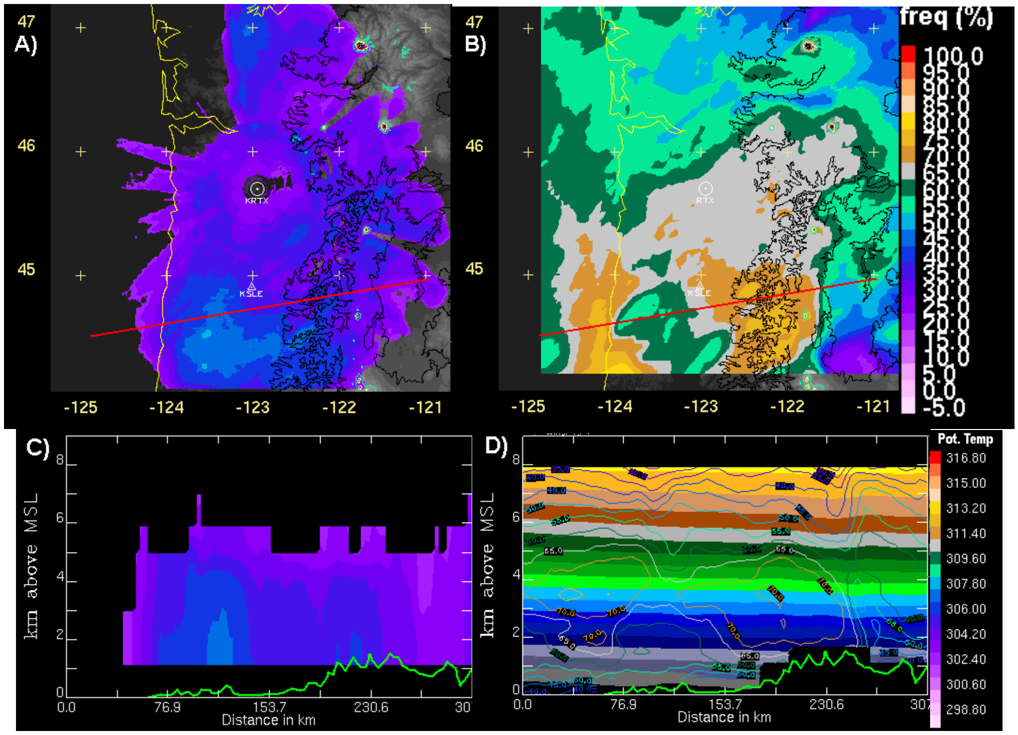

Fig. 29. Comparison of precipitation structures for southeast (SE) storms for the 2005-2006 winter storm season. Radar observations are on the left, while model output is to the right. Observed precipitation frequency figures show only values > 20 %. (a) Horizontal precipitation frequency (%) pattern for observed SE storms. (b) Same as (a) except for model SE storms. (c) Vertical cross section along red line from (a). (d) Vertical cross section along red line in (b) with QT frequency as contours and potential temperature as filled contours.

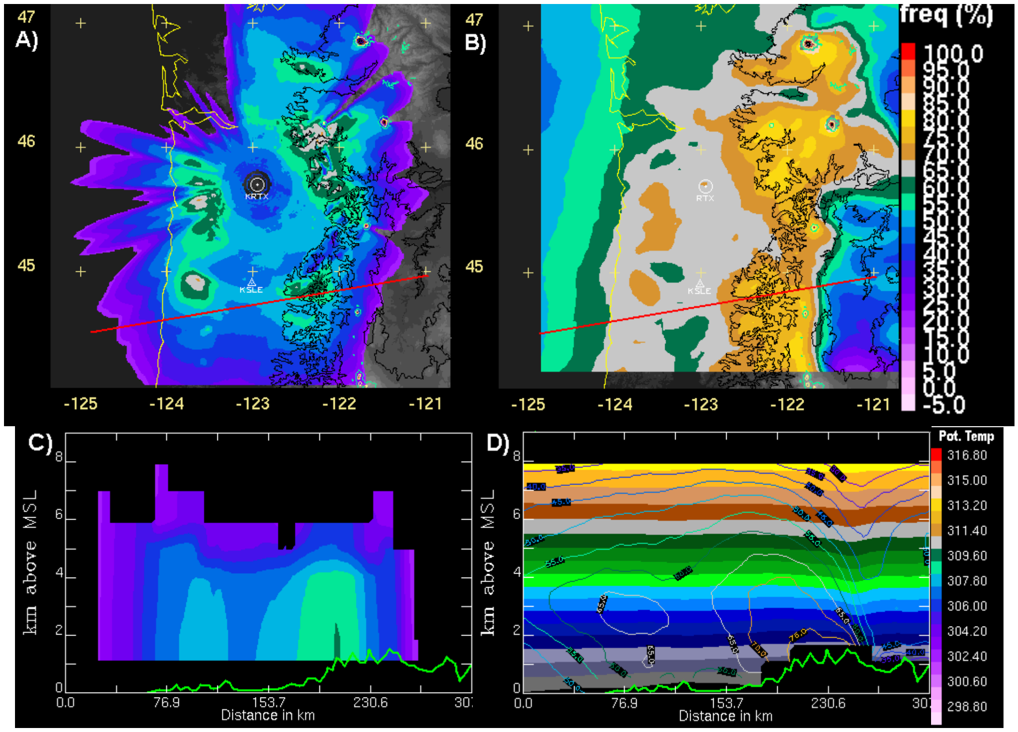

Fig. 30. Comparison of precipitation structures for south/southwest (S-SW) storms for the 2005-2006 winter storm season. Radar observations are on the left, while model output is to the right. Observed precipitation frequency figures show only values > 20 %. (a) Horizontal precipitation frequency (%) pattern for observed S-SW storms. (b) Same as (a) except for model S-SW storms. (c) Vertical cross section along red line from (a). (d) Vertical cross section along red line in (b) with QT frequency as contours and potential temperature as filled contours.

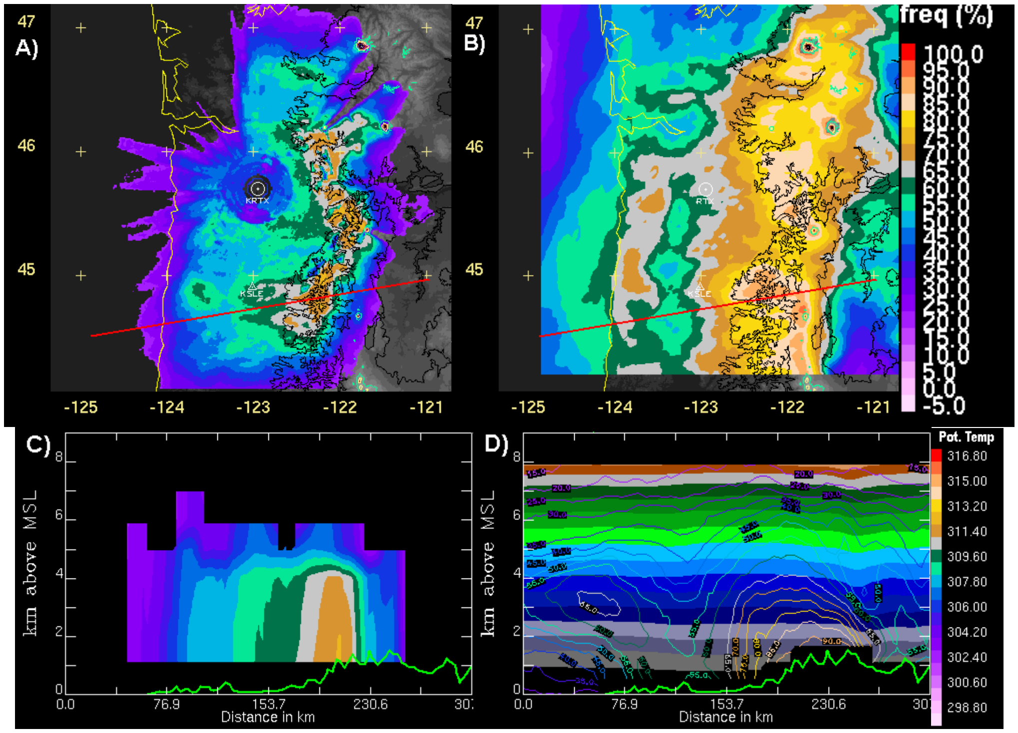

Fig. 31. Comparison of precipitation structures for west/northwest (W-NW) storms for the 2005-2006 winter storm season. Radar observations are on the left, while model output is to the right. Observed precipitation frequency figures show only values > 20 %. (a) Horizontal precipitation frequency (%) pattern for observed W-NW storms. (b) Same as (a) except for model W-NW storms. (c) Vertical cross section along red line from (a). (d) Vertical cross section along red line in (b) with QT frequency as contours and potential temperature as filled contours.

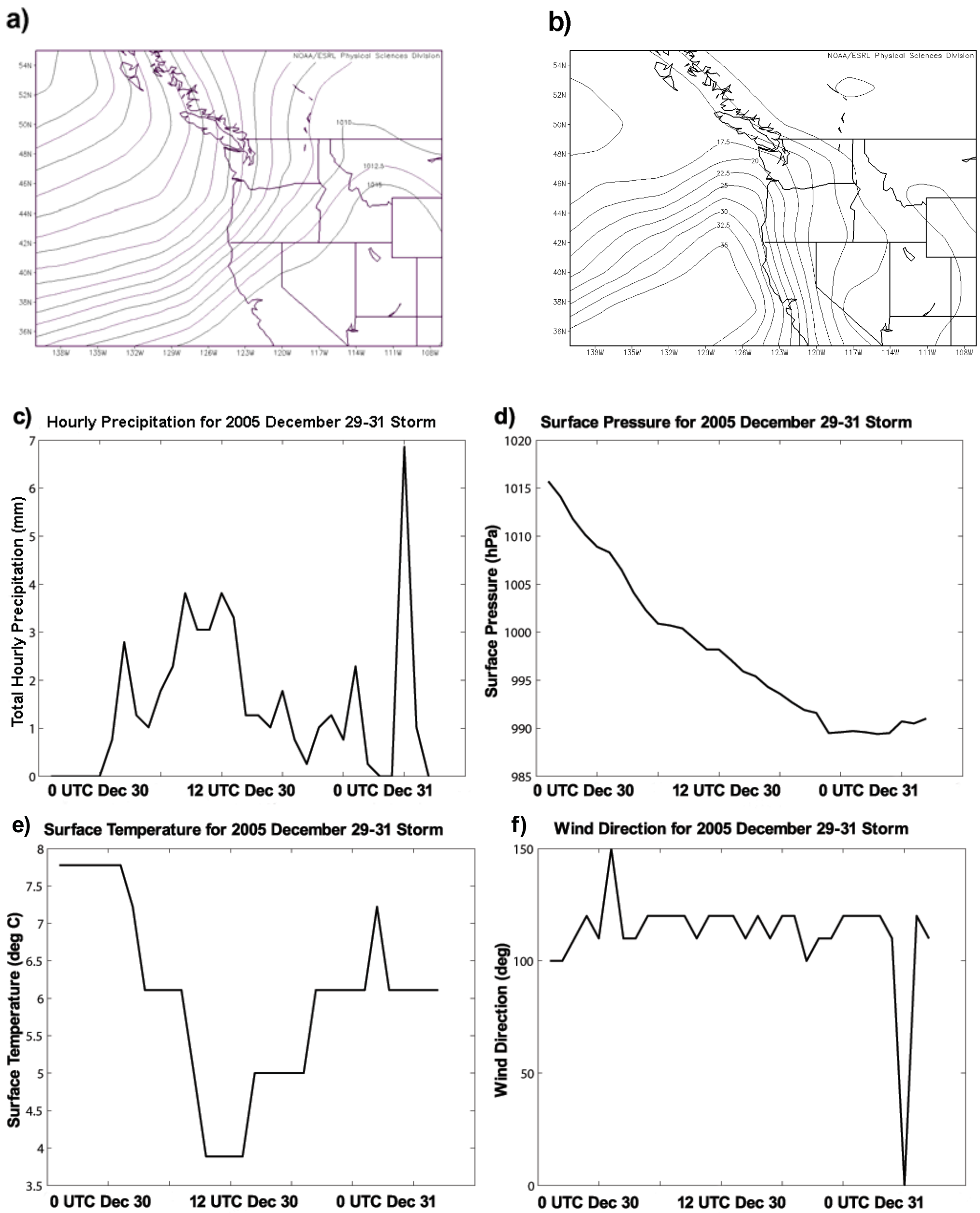

Fig. 32. Characteristics of the 2005 December 29 – 31 storm. (a) Reanalysis plot of surface pressure (hPa) for 24-h period on 2005 Dec 30 (ESRL Reanalysis). (b) Reanalysis plot of precipitable water (mm) for 24-h period on 2005 Dec 30 (ESRL Reanalysis). (c) Total hourly precipitation (mm) from PDX for 2100 UTC 29 Dec 2005 to 0400 UTC 31 Dec 2005. (d) Hourly surface pressure (hPa) for same time period as (c). (e) Hourly surface temperature (° C) for same time period as (c). (f) Hourly wind direction (deg azimuth) for same time period as (c).

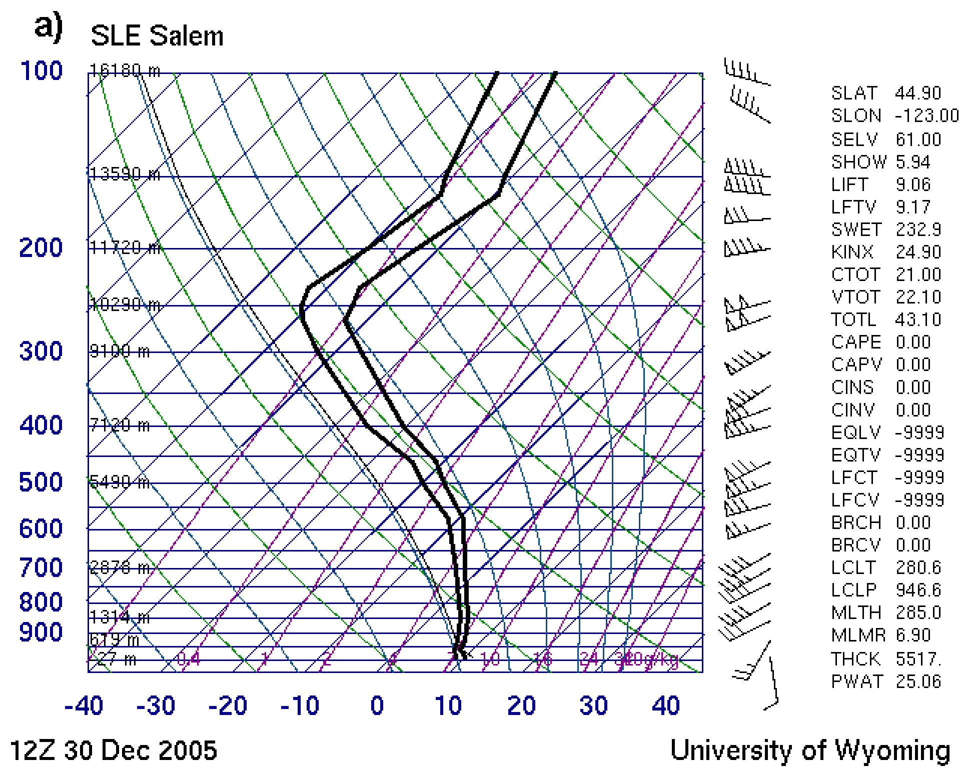

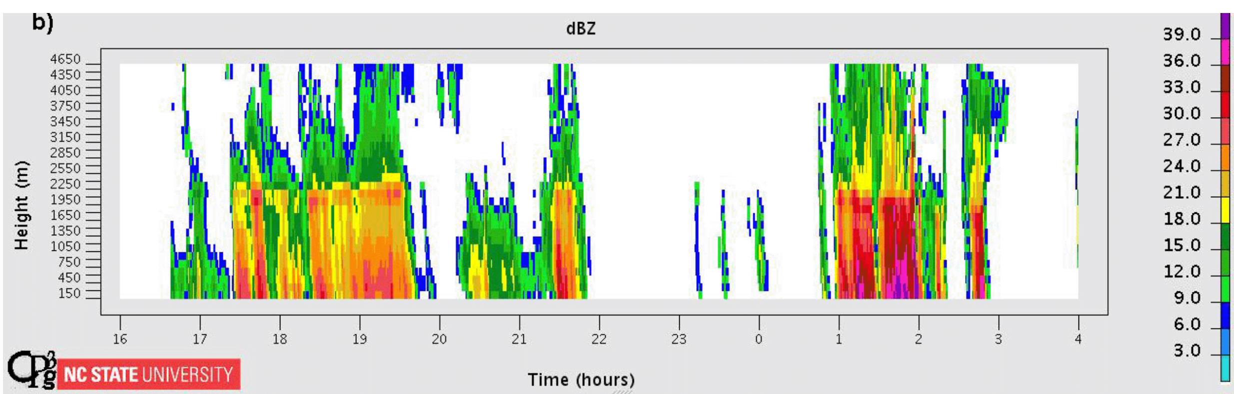

Fig. 33. (a) Vertical profile of SLE sounding for 1200 UTC 30 Dec 2005 representative of flow during the 2005 Dec 29-31 storm. (b) Time height plot of Micro Rain Radar (MRR) vertically pointing radar data for Portland, OR during the 2005 Dec 29-31 storm. Period begins after 1600 UTC 30 Dec 2005 due to missing data.

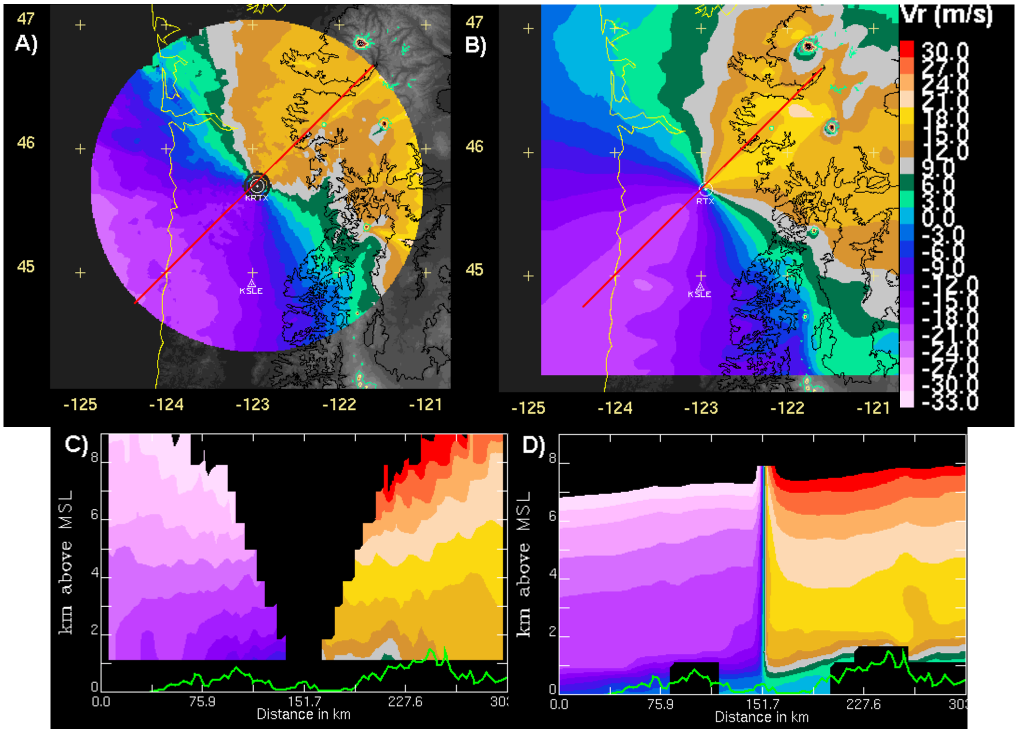

Fig. 34. Comparison of radial velocity structures (ms^{-1}) for the 2005 December 29-31 storm case. Radar observations are on the left, while model output is to the right. Observed precipitation frequency figures show only values > 20 %. (a) Horizontal mean radial velocity pattern for observed SE storms. (b) Same as (a) except for model SE storms. (c) Vertical cross section along red line from (a). (d) Vertical cross section along red line in (b).

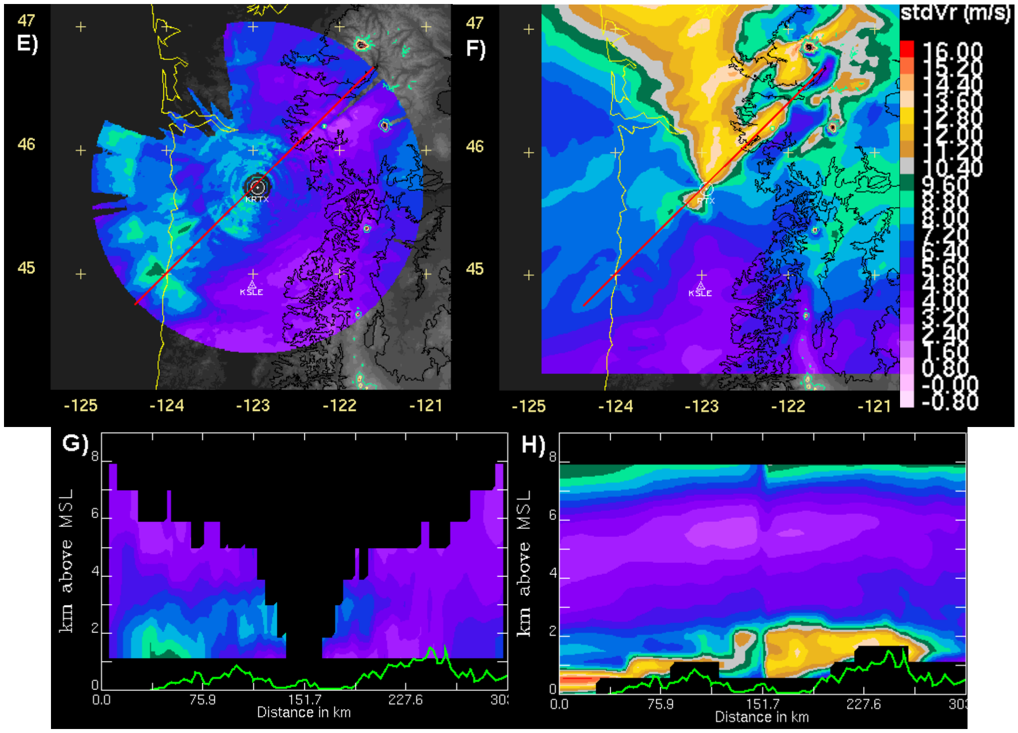

Fig. 34 cont. (e) Standard deviation values of (a). (f) Standard deviation values of (b). (g) Vertical cross section along red line in (e). (h) Vertical cross section along red line in (f).

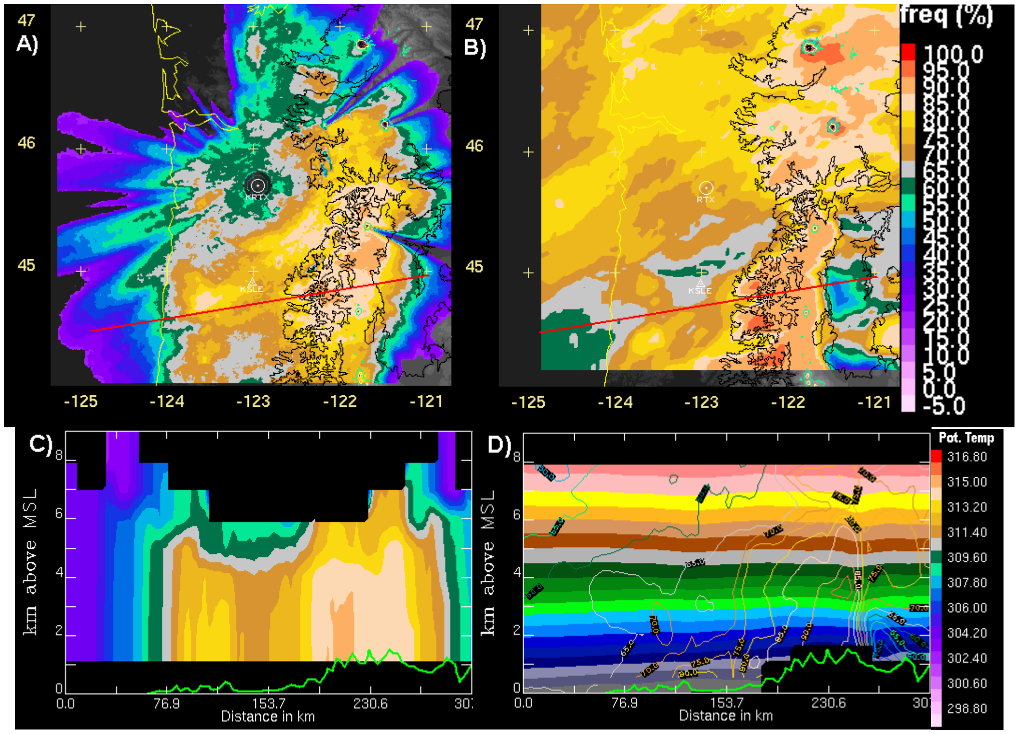

Fig. 35. Comparison of precipitation frequency (%) for the 29 – 31 December 2005 storm case. Radar observations are on the left, while model output is to the right. Observed precipitation frequency figures show only values > 20 %. (a) Horizontal mean radial velocity pattern for observed SE storms. (b) Same as (a) except for model SE storms. (c) Vertical cross section along red line from (a). (d) Vertical cross section along red line in (b) with QT frequency as contours and potential temperature as filled contours.

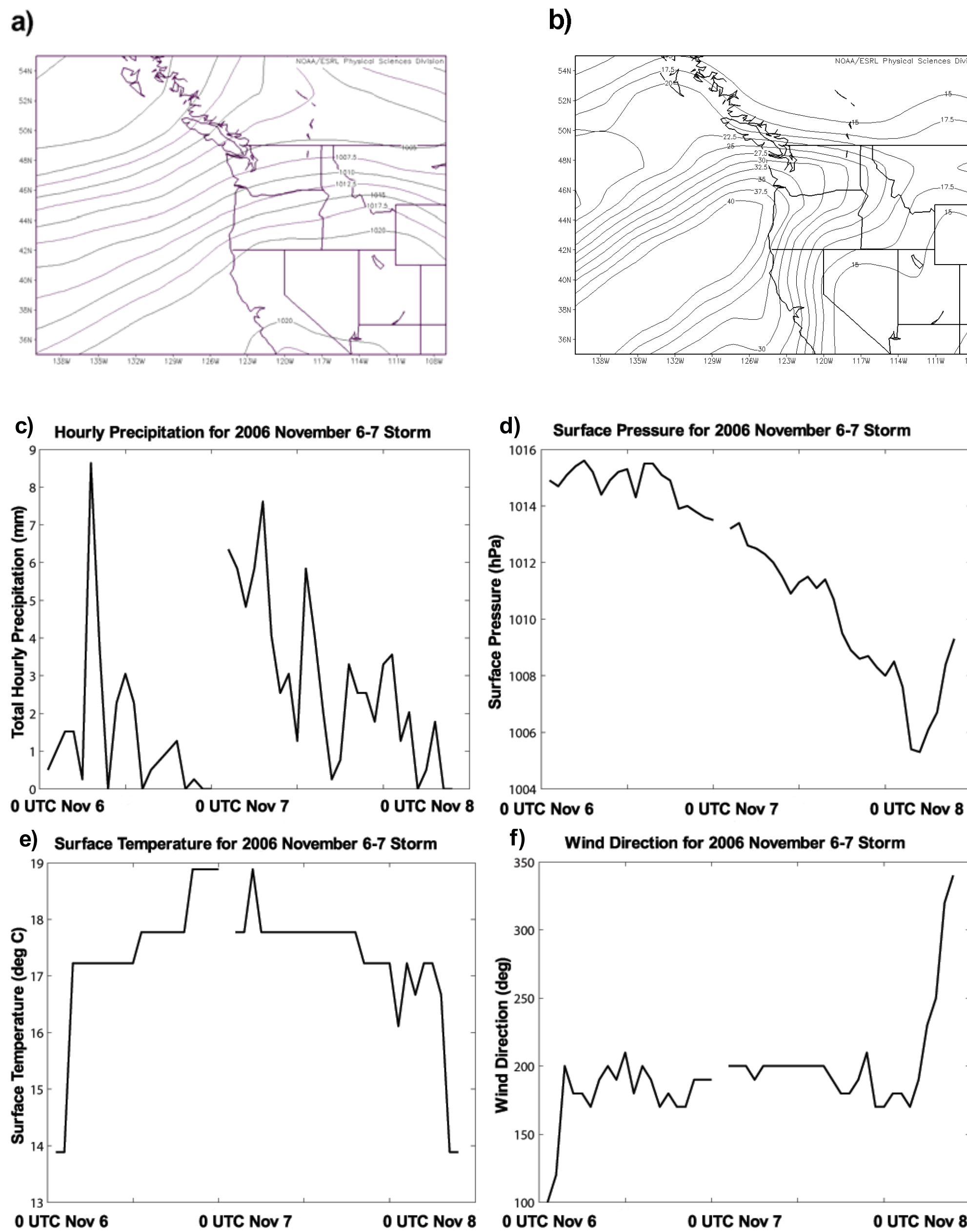

Fig. 36. Characteristics of the 2006 November 6 – 7 storm. (a) Reanalysis plot of surface pressure (hPa) for 48-h period on 2006 Nov 6 – 7 (ESRL Reanalysis). (b) Reanalysis plot of precipitable water (mm) for 48-h period on 2006 Nov 6 – 7 (ESRL Reanalysis). (c) Total hourly precipitation (mm) from PDX for 0000 UTC 6 Nov 2006 to 0000 UTC 8 Nov 2006. (d) Hourly surface pressure (hPa) for same time period as (c). (e) Hourly surface temperature (° C) for same time period as (c). (f) Hourly wind direction (deg azimuth) for same time period as (c).

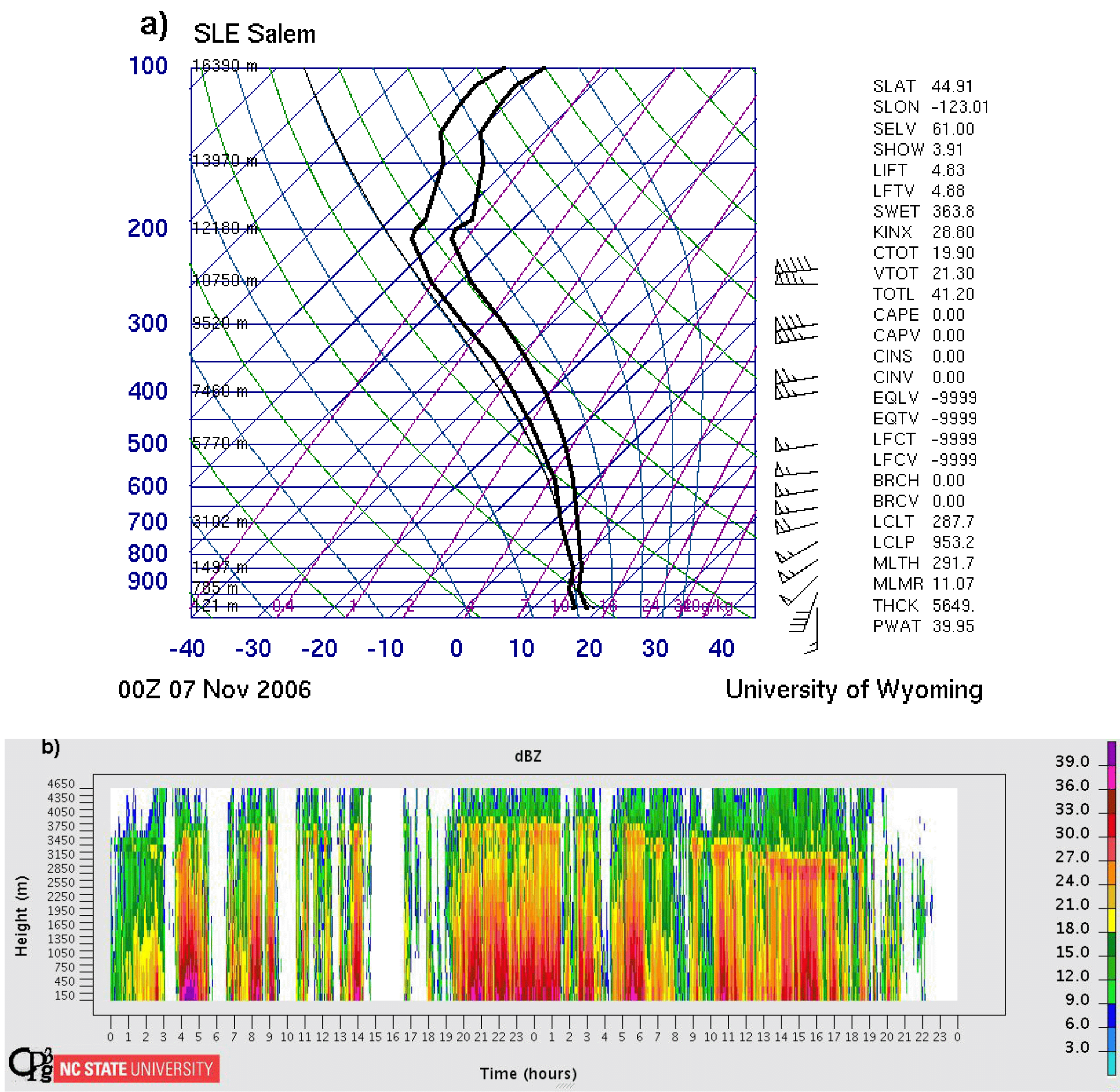

Fig. 37. (a) Vertical profile of SLE sounding for 0000 UTC 7 Nov 2006 representative of flow during the 2006 Nov 6 – 7 storm. (b) Time height plot of Micro Rain Radar (MRR) vertically pointing radar data for Portland, OR during the 2006 Nov 6 – 7 storm.

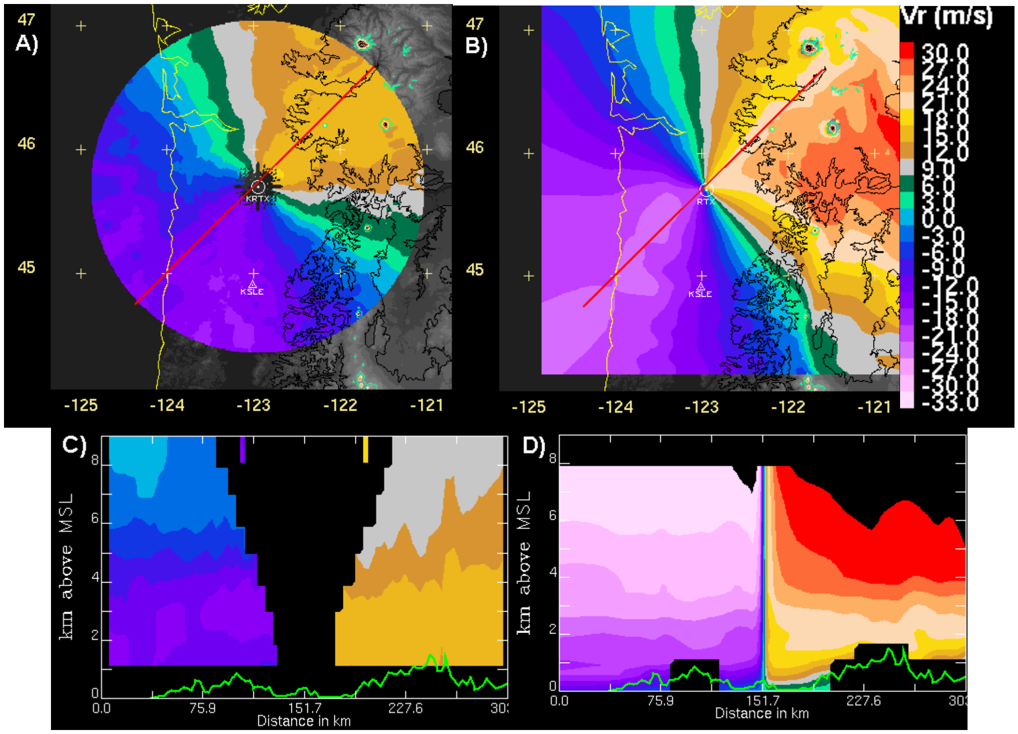

Fig. 38. Comparison of radial velocity structures (ms^{-1}) for the 2006 November 6 – 7 storm case. Radar observations are on the left, while model output is to the right. Observed precipitation frequency figures show only values > 20 %. (a) Horizontal mean radial velocity pattern for observed SE storms. (b) Same as (a) except for model SE storms. (c) Vertical cross section along red line from (a). (d) Vertical cross section along red line in (b).

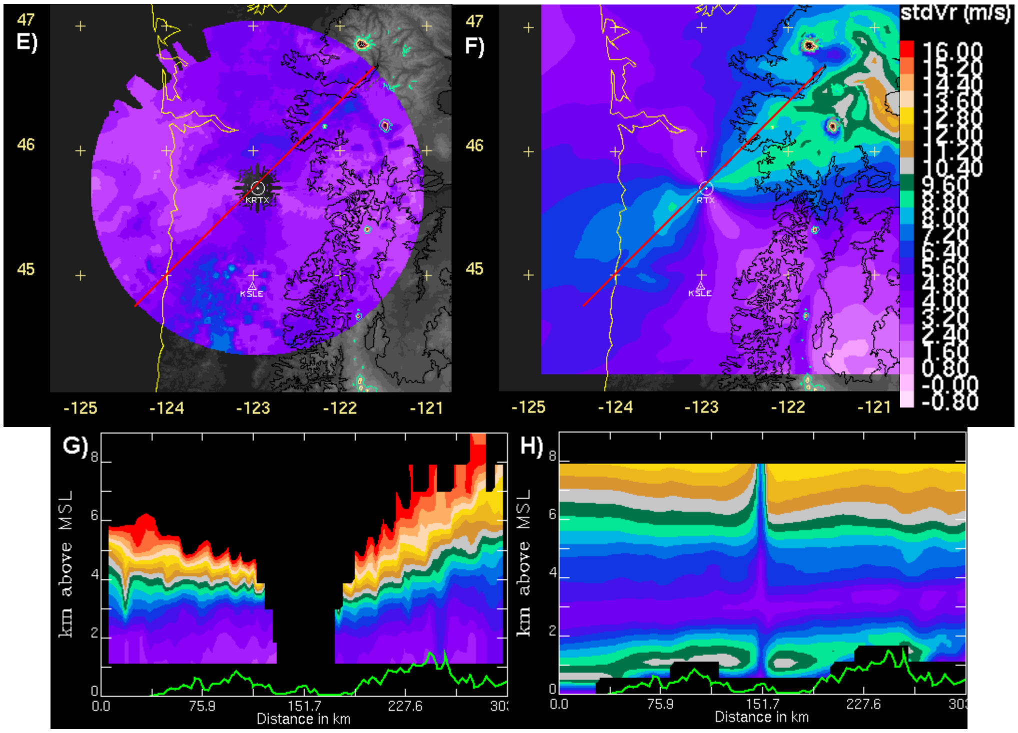

Fig. 38 cont. (e) Standard deviation values of (a). (f) Standard deviation values of (b). (g) Vertical cross section along red line in (e). (h) Vertical cross section along red line in (f).

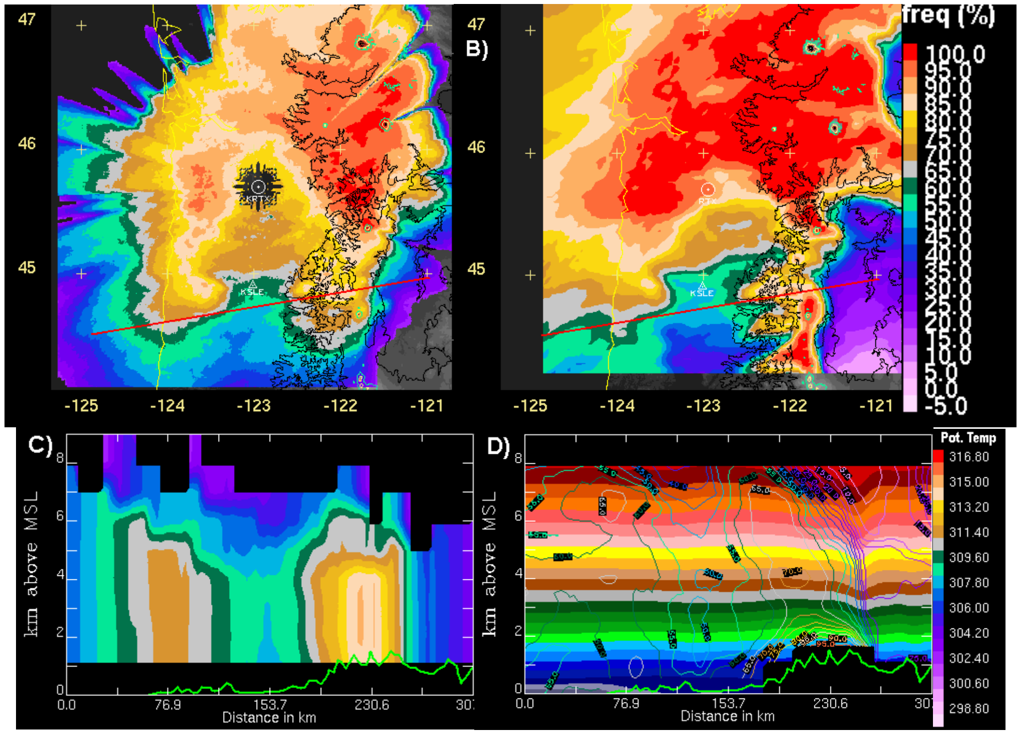

Fig. 39. Comparison of precipitation structures (ms^{-1}) for the 2006 November 6 – 7 storm case. Radar observations are on the left, while model output is to the right. Observed precipitation frequency figures show only values > 20 %. (a) Horizontal precipitation frequency pattern for observed SE storms. (b) Same as (a) except for model SE storms. (c) Vertical cross section along red line from (a). (d) Vertical cross section along red line in (b) with QT frequency as contours and potential temperature as filled contours.

References

Barnes S. L., 1980: Report on a meeting to establish a common Doppler radar data exchange format. *Bull. Amer. Meteor. Soc*, **61**, 1401–1404.

Bougeault, P., P. Binder, A. Buzzi, R. Dirks, R. Houze, J. Kuettner, R. B. Smith, R. Steinacker, and H. Volkert, 2001: The MAP Special Observing Period. *Bull. Amer. Meteor. Soc.*, **82**, 433–462.

Colle, B. A. and C. F. Mass, 2000: The 5–9 February 1996 flooding event over the Pacific Northwest: Sensitivity studies and evaluation of the MM5 precipitation forecasts. *Mon. Wea. Rev.*, **128**, 593–617.

Colle, B. A., 2004: Sensitivity of orographic precipitation to changing ambient conditions and terrain geometries: An idealized modeling perspective. *J. Atmos. Sci.*, **61**, 588–606.

Colle, B. A., M. F. Garvert, J. B. Wolfe, C. F. Mass, and C. P. Woods, 2005: The 13–14 December 2001 IMPROVE-2 Event. Part III: Simulated microphysical budgets and sensitivity studies. *J. Atmos. Sci.*, **62**, 3535–3558.

Colle, B. A., J. B. Wolfe, W. J. Steenburgh, D. E. Kingsmill, J. A. W. Cox, and J. C. Shafer, 2005: High-resolution simulations and microphysical validation of an orographic precipitation event over the Wasatch Mountains during IPEX IOP3. *Mon. Wea. Rev.*, **133**, 2947–2971.

Cox, J. A. W., W. J. Steenburgh, D. E. Kingsmill, J. C. Shafer, B. A. Colle, O. Bousquet, B. F. Smull, and H. Cai, 2005: The kinematic structure of a Wasatch Mountain winter storm during IPEX IOP3. *Mon. Wea. Rev.*, **133**, 521–542.

Daly, C., R. P. Neilson, and D. L. Phillips, 1994: A statistical-topographic model for mapping climatological precipitation over mountainous terrain. *J. Appl. Meteor.*, **33**, 140–158.

Dettinger, M., K. Redmond, and D. Cayan, 2004: Winter orographic precipitation ratios in the Sierra Nevada – Large-scale atmospheric circulations and hydrologic consequences. *J. Hydrometeor.*, **5**, 1102–1116.

Durran D. R., and J. B. Klemp, 1982: On the effects of moisture on the Brunt–Väisälä frequency. *J. Atmos. Sci.*, **39**, 2152–2158.

Emanuel, K. A., 1994: *Atmospheric Convection*. Oxford University Press, 580 pp.

Garvert, M. F., B. A. Colle, and C. F. Mass, 2005: The 13–14 December 2001 IMPROVE-2 Event. Part I: Synoptic and mesoscale evolution and comparison with a mesoscale model simulation. *J. Atmos. Sci.*, **62**, 3474–3492.

Garvert, M. F., C. P. Woods, B. A. Colle, C. F. Mass, P. V. Hobbs, M. T. Stoelinga, and J. B. Wolfe, 2005: The 13–14 December 2001 IMPROVE-2 Event. Part II: Comparisons of MM5 model simulations of clouds and precipitation with observations. *J. Atmos. Sci.*, **62**, 3520–3534.

Garvert, M. F., B. Smull, and C. Mass, 2007: Multiscale mountain waves influencing a major orographic precipitation event. *J. Atmos. Sci.*, **64**, 711–737.

Grossman, R. L. and D. R. Durran, 1984: Interaction of low-level flow with the Western Ghat Mountains and offshore convection in the summer monsoon. *Mon. Wea. Rev.*, **112**, 652–672.

Hagen, M. and S. E. Yuter, 2003: Relations between radar reflectivity, liquid-water content, and rainfall rate during MAP SOP. *Quart. J. Roy. Meteor. Soc.*, **129**, 477–493.

James, C. N., S. R. Brodzik, H. Edmon, R. A. Houze Jr., and S. E. Yuter, 2000: Radar data processing and visualization over complex terrain. *Wea. Forecasting*, **15**, 327–338.

James, C. N. and R. A. Houze Jr., 2001: A real-time four-dimensional Doppler dealiasing scheme. *J. Atmos. Ocean. Tech.*, **18**, 1674–1683.

James, C. N. and R. A. Houze Jr., 2005: Modification of precipitation by coastal orography in storms crossing Northern California. *Mon. Wea. Rev.*, **133**, 3110–3131.

JISAO, cited 2007: The Pacific Decadal Oscillation (PDO). [Available online at http://jisao.washington.edu/pdo].

Lackmann, G. M. and J. R. Gyakum, 1999: Heavy cold-season precipitation in the Northwestern United States: Synoptic climatology and an analysis of the flood of 17–18 January 1986. *Wea. Forecasting*, **14**, 687–700.

Medina S., and R. A. Houze Jr., 2003: Air motions and precipitation growth in Alpine storms. *Quart. J. Roy. Meteor. Soc.*, **129**, 345–371.

Medina S., B. F. Smull, R. A. Houze Jr., and M. Steiner, 2005: Cross-barrier flow during orographic precipitation events: Results from MAP and IMPROVE. *J. Atmos. Sci.*, **62**, 3580–3598.

Medina, S., E. Sukovich, R. A. Houze Jr., 2007: Vertical structures of precipitation in cyclones crossing the Oregon Cascades. *Mon. Wea. Rev.*, submitted.

Neiman, P. J., P. O. G. Persson, F. M. Ralph, D. P. Jorgensen, A. B. White, and D. E. Kingsmill, 2004: Modification of fronts and precipitation by coastal blocking during an intense landfalling winter storm in Southern California: Observations during CALJET. *Mon. Wea. Rev.*, **132**, 242–273.

Neiman, P. J., F. M. Ralph, G. A. Wick, J. D. Lundquist, M. D. Dettinger, 2007: Meteorological characteristics and overland precipitation impacts of atmospheric rivers affecting the West Coast of North America based on eight years of SSM/I satellite observations. *J. Hydrometeor.,* submitted.

Ralph, F. M., P. J. Neiman, and G. A. Wick, 2004: Satellite and CALJET aircraft observations of atmospheric rivers over the Eastern North Pacific Ocean during the winter of 1997/98. *Mon. Wea. Rev.*, **132**, 1721–1745.

Ralph F. M., P. J. Neiman, and R. Rotunno, 2005: Dropsonde observations in low-level jets over the northeastern Pacific Ocean from CALJET-1998 and PACJET-2001: Mean vertical-profile and atmospheric-river characteristics. *Mon. Wea. Rev.*, **133**, 889–910.

Rotunno, R. and R. Ferretti, 2003: Orographic effects on rainfall in MAP cases IOP2b and IOP8. *Quart. J. Roy. Meteor. Soc.*, **129**, 373-390.

Rotunno, R. and R. A. Houze Jr., 2007. Lessons on orographic precipitation from the Mesoscale Alpine Programme. *Quart. J. Roy. Meteor. Soc.*, **133**, 811–830.

Schultz, D. M., W. J. Steenburgh, R. J. Trapp, J. Horel, D. E. Kingsmill, L. B. Dunn, W. D. Rust, L. Cheng, A. Bansemer, J. Cox, J. Daugherty, D. P. Jorgensen, J. Meitín, L. Showell, B. F. Smull, K. Tarp, and M. Trainor, 2002: Understanding Utah winter storms: The Intermountain Precipitation Experiment. *Bull. Amer. Meteor. Soc.*, **83**, 189–210.

Sinclair, M. R., D. S. Wratt, R. D. Henderson, and W. R. Gray, 1997: Factors affecting the distribution and spillover of precipitation in the Southern Alps of New Zealand—A case study. *J. Appl. Meteor.*, **36**, 428–442.

Smith R. B., 1979: The influence of mountains on the atmosphere. *Advances in Geophysics,* Vol. 21, 87–230.

Smith, R. B., Q. Jiang, M. G. Fearon, P. Tabary, M. Dorninger, J. D. Doyle, R. Benoit, 2003: Orographic precipitation and air mass transformation: An Alpine example. *Quart. J. Roy. Meteor. Soc.*, **129**, 433–454.

Smith, R. B. and I. Barstad, 2004: A linear theory of orographic precipitation. *J. Atmos. Sci.*, **61**, 1377–1391.

Stoelinga, M. T., P. V. Hobbs, C. F. Mass, J. D. Locatelli, B. A. Colle, R. A. Houze Jr., A. L. Rangno, N. A. Bond, B. F. Smull, R. M. Rasmussen, G. Thompson, and B. R. Colman, 2003: Improvement of Microphysical Parameterization through Observational Verification Experiment. *Bull. of Amer. Meteor. Soc.*, **84**, 1807–1826.

Taylor, G. H., cited 2007: Impacts of the El Niño/Southern Oscillation on the Pacific Northwest. [Available online at http://www.ocs.orst.edu/reports/enso_pnw.html].

Wallace, J. M. and P. V. Hobbs, 1977: *Atmospheric Science: An Introductory Survey*. Academic Press, 467 pp.

White, A. B., P. J. Neiman, F. M. Ralph, D. E. Kingsmill, and P. O. G. Persson, 2003: Coastal orographic rainfall processes observed by radar during the California Land-Falling Jets Experiment. *J. Hydrometeor.*, **4**, 264–282.

Zhu, Y. and R. E. Newell, 1998: A proposed algorithm for moisture fluxes from atmospheric rivers. *Mon. Wea. Rev.*, **126**, 725–735.